Timber Creep of Historic Urban Quay Walls

The influence of creep of foundation piles on the assessment of inner-city quay walls

T.M. Spannenburg

Technische Universiteit Delft

TU Delft

Timber Creep of Historic Urban Quay Walls

The influence of creep of foundation piles on the assessment of inner-city quay walls

T.M. Spannenburg

Project duration:	September, 2019 – August, 2020	
Supervisors:	Dr. ir. M. Korff (Chair of Committee)	TU Delft
	Dr. ir. D.J. Peters	TU Delft
	Drs. W.F. Gard	TU Delft
	Prof. dr. ir. J.W.G. van de Kuilen	TU Delft
	Ir. M. op de Kelder	IB Amsterdam

Preface

Years ago I started my journey at Civil Engineering at Delft University of Technology. Still to this day, it can be difficult to fathom the amount of knowledge and experience one gains during these years. This Master Thesis marks the end of my journey, which I hereby proudly present.

First I would like to thank IB Amsterdam for the possibility to perform this study in cooperation with them. In addition, I would like to thank my colleagues there for both the support as well as the opportunity to gain insights on other aspects within the engineering department of a municipality. A special thanks goes to C.C. Cordova for being a harsh, but much appreciated, sparring partner.

Next, I would like to thank all committee members for their support, reflection and recommendations. An additional thanks goes to M. op de Kelder, who functioned as daily supervisor.

And concluding, I would like to thank all friends and family members that have helped me throughout this project. From discussions on the topic to just being there, I appreciate all of your words and actions.

Trevor Spannenburg
Zeewolde, August 2020

Abstract

Amsterdam and many other cities consist of a network of old quay walls, which sometimes have been constructed over a century ago. A large uncertainty exists concerning the current safety of these quay walls and their remaining service lifetime. In the current framework for the assessment of old urban quay walls, the influence of timber creep in the structure is being omitted. Since the structures sometimes display excessive deformation, it needs to be investigated whether this deformation is due to creep, or might be a sign of overloading. This research studied the influence of wood creep on the structural behaviour of old urban quay walls, using a case study based on a real historic one at the Herengracht. For this location, information on the geometry is available, such as the number of piles. Furthermore, geotechnical data is present, obtained from both lab and field tests.
For the modelling of the quay walls, use has been made of the Embedded Beam Row (EBR) elements in Plaxis 2D. The EBR feature places beam elements parallel to the soil mesh and connects them via interface elements. Creep has been modelled by using pseudo-elasticity. For each time step, the elasticity of the EBR elements is reduced with an increasing creep factor. At the time of writing, the EBR feature had not been verified for Amsterdam-like soil conditions. The original verification had only been done for uniform sand layers. The EBR has been verified based on a full-scale lateral load test performed at Salt Lake City. In this case, a 3x5 pile group driven in multi-layered cohesive and non-cohesive soils, similar to Amsterdam. The results included deformations, total horizontal load and bending moment distributions over depth. It has been found that the EBR provides reasonable results when modelling laterally loaded pile groups. The force-displacement curve obtained using Plaxis was close to as had been measured. Maximum bending moments obtained using the EBR had been found to be 20 to 30% lower compared to the experimental data. The group efficiency of the pile group was initially lower for small displacements, which was likely caused by the lack of installation effects of driven piles in the Plaxis model. It has been observed that the Interface Stiffness Factors (ISF) that are used to calibrate the EBR behaviour have a limited range. Increasing the ISF values beyond a certain limit will no longer affect results, as the interface connecting the EBR to the soil will have become practically rigid at this point. Nevertheless, it has been concluded the EBR can be used in this case to model laterally loaded pile groups.

The influence of the timber creep on the structural behaviour of quay walls has been studied using a model based on the Herengracht in Amsterdam. A maximum creep factor has been applied of φ=1.6. Two methods have been used to apply the final creep factor. With the "Direct" method, the maximum creep factor was applied in the same phase as the load. With the "Indirect" method, the creep factor has been applied incrementally in steps of 0.1. It has been observed that the results from these methods deviate significantly. With the Indirect method, larger creep displacements have been calculated, as well as lower maximum compressive stresses in the piles. The creep behaviour has been studied in more depth using the Indirect method. In this case study, creep displacements of 2.22 times the initial displacement have been calculated. When plotted against the increasing creep factors, it has been observed a power function could be fitted to the data. In addition, a stress reduction of 0.590 times the initial maximum compressive stress has been observed in the front two pile rows. This stress reduction was achieved at φ=0.4. In the most landin pile row, stresses continued to decrease, with a reduced rate beyond φ=0.4. A sensitivity analysis has been performed to study which parameters have significant influence on the creep behaviour. Conclusions were drawn based on the relative change in horizontal displacement and maximum compressive stress in the front pile row. It has been concluded that the shear strength parameters of the top layer, the elastic modulus of the timber, surface load and the geometry have the largest influence on the creep behaviour. Furthermore, it has been discovered that the size of the creep factor steps influences the final stress and displacement. With decreasing stepsize, convergence occurred in the results.

From the results it has been concluded that the structural behaviour of old urban quay walls is significantly influenced by timber creep. The inclusion of timber creep in the analysis resulted in large displacement increases, but also in a stress reduction. The results suggest that excessive deformations of quay walls do not necessarily mean that an ultimate limit state has been reached. It is recommended to include the timber creep in the modelling and assessment of existing quay walls.

Contents

List of Figures

List of Tables

List of Symbols

Latin characters

A	=	Cross-sectional area	$[m^2]$
	=	Scale factor power creep law	$[m]$
b	=	Width	$[m]$
c'	=	Effective cohesion	$[N/m^2]$
CDF	=	Cumulative distribution function	[-]
D	=	Pile diameter	$[m]$
D_{eq}	=	Equivalent pile diameter	$[m]$
d	=	Water depth	$[m]$
E	=	Elastic modulus, Young's modulus	$[N/m^2]$
E_0	=	Soils: small strain stiffness	$[N/m^2]$
	=	Initial elastic modulus	$[N/m^2]$
E_{50}	=	Elastic modulus for primary loading	$[N/m^2]$
E_{50}^{ref}	=	Elastic modulus for primary loading at reference pressure	$[N/m^2]$
E_B	=	Elastic bending modulus	$[N/m^2]$
$E_{Ménard}$	=	Ménard stiffness, radial elasticity modulus piles	$[N/m^2]$
E_{oed}	=	Oedometer modulus	$[N/m^2]$
E_{pot}	=	Potential energy	$[Nm]$
E_{oed}^{ref}	=	Oedometer modulus at reference pressure	$[N/m^2]$
E_{ur}	=	Elastic modulus for un-/reloading	$[N/m^2]$
E_{ur}^{ref}	=	Elastic modulus for un-/reloading at reference pressure	$[N/m^2]$
e_0	=	Initial void ratio	[-]
F	=	Force	$[N]$
f	=	Empirical factor correlating $E_{Ménard}$ to K_H	[-]
$f_{m,k}$	=	Characteristic bending strength	$[N/m^2]$
$f_{t,0,k}$	=	Characteristic tensile strength parallel to the grain	$[N/m^2]$
$f_{c,0,k}$	=	Characteristic compressive strength parallel to the grain	$[N/m^2]$
G	=	Shear modulus	$[N/m^2]$
G_0	=	Initial shear modulus	$[N/m^2]$
g	=	Gravitational constant	$[m/s^2]$
h	=	Height	$[m]$
I	=	Moment of inertia	$[m^4]$
ISF_{RN}	=	Interface Stiffness Factor lateral spring Embedded Beam Row interface	[-]
ISF_{RS}	=	Interface Stiffness Factor axial spring Embedded Beam Row interface	[-]
ISF_{KF}	=	Interface Stiffness Factor foot spring Embedded Beam Row interface	[-]
K_H	=	Horizontal modulus of subgrade reaction for piles	$[N/m]$
K_n	=	Elastic lateral stiffness Embedded Beam Row interface	$[N/m^2/m']$
K_s	=	Elastic axial stiffness Embedded Beam Row interface	$[N/m^2/m']$
L	=	Length	$[m]$
$L_{spacing}$	=	Centre-to-centre pile spacing	$[m]$
M	=	Bending moment	$[Nm]$
MOR	=	Modulus of Rupture, flexural strength	$[Nm]$
m	=	Factor stress dependency stiffness	[-]
	=	Slope factor power creep law	[-]
N	=	Axial normal force	$[N]$
n	=	Amount, number	[-]
p'_{max}	=	Bearing capacity	$[N/m^2]$
p^{ref}	=	Reference pressure	$[N/m^2]$

p_{water}	=	Water pressure	$[N/m^2]$
q_c	=	Cone resistance	$[N/m^2]$
R_{eq}	=	Equivalent radius	$[m]$
t	=	Time	$[s]$
t_n	=	Lateral traction Embedded Beam Row interface element	$[N/m/m']$
t_s	=	Axial traction Embedded Beam Row interface element	$[N/m/m']$
u	=	Displacement	$[m]$
V	=	Shear force	$[N]$
	=	Volume	$[m^3]$

Greek characters

α	=	Empirical factor correlating $E_{Ménard}$ to K_H	[-]
ϵ	=	Error	[-]
ε	=	Strain	[-]
ε_e	=	Elastic strain	[-]
ε_c	=	Creep strain	[-]
γ	=	Shear strain	[-]
	=	Specific weight	$[kN/m^3]$
$\gamma_{0.7}$	=	Threshold shear strain Hardening Soil small strain model	[-]
γ_n	=	Natural specific weight	$[N/m^3]$
γ_{sat}	=	Saturated specific weight	$[N/m^3]$
γ'_{soil}	=	Effective specific weight of soil	$[N/m^3]$
γ_{unsat}	=	Unsaturated specific weight	$[N/m^3]$
γ_w	=	Specific weight water	$[N/m^3]$
Δ	=	Relative density	[-]
κ	=	Curvature	$[m^{-1}]$
μ	=	Mean value	[/]
ν_{ur}	=	Poisson's ratio for un-/reloading	[-]
φ	=	Creep factor	[-]
	=	Friction angle	[°]
φ'	=	Effective friction angle	[°]
ψ	=	Dilatency angle	[°]
ρ	=	Density	$[kg/m^3]$
σ	=	Stress	$[N/m^2]$
	=	Standard deviation of normal distribution	[/]

1 Introduction

1.1. Background and motivation

The centre of Amsterdam is, alike many Dutch historic cities, dominated by quay walls. With the growth of the cities in previous centuries, new quay walls had been constructed. From time to time, these have been replaced. At the time of writing, Amsterdam is facing a large maintenance task. In the past couple of years, multiple cases had been reported in which quay walls had become unsafe and required emergency operations (Amsterdam, 2020). During a recent assessment of the quay walls, the municipality of Amsterdam had deemed 200 km, out of they 600 km that is their responsibility, as unsafe. Large sections of these quay walls are over 100 years old. Given the time-dependent behaviour of wood, it is unknown in what state the material is. Over time, the wood used in the construction has undergone decades of loading and unloading, degradation, bacterial attacks and more. These aspects all form part of a vast collection of uncertainties in the current framework used for the assessment of quay walls.

One of the aspects that has been neglected is the creep of timber. Under continuous loading, the strain of wood increases over time. As a result, large displacements are generated over time, which can eventually lead to failure. Given the age of some of these structures, the timber creep is likely to play a role in the large deflections occurring in the Amsterdam quay walls. It is uncertain though what this role is and especially how it influences the remaining safety. It is plausible that the horizontal displacements are caused by the timber creep, although it is unknown to which extent.

As a result, this study has been performed to gain rudimental insight on the behaviour of quay walls under influence of timber creep. In order to do so, a case study has been modelled based on the Herengracht in the centre of Amsterdam. For calculations, use has been made of the Embedded Beam Row (EBR) feature in Plaxis 2D. In Chapter 2, a literature study has been performed on the topic of timber creep. Furthermore, the Embedded Beam Row and its implementation has been researched as well. In Chapter 3, a verification of the EBR has been executed based on a full-scale pile group testing, performed in soil conditions alike those in Amsterdam. Chapter 4 will introduce the Plaxis 2D model that has been used for the Herengracht case. The timber creep has been implemented in Chapter 5, in which the results of the quay wall behaviour influenced by creep will be presented. A sensitivity analysis has been performed concerning which parameters affect the creep behaviour of the quay walls, which will be discussed in Chapter 6. Chapter 7 will provide a short discussion on how varying creep rates might influence the results obtained in the previous chapters. In Chapter 8 the influence of soil creep on the quay wall behaviour has been theorised. Finally, conclusions will be drawn regarding the wood creep behaviour on timber walls and recommendations regarding both research and design will be made.

1.2. Research objectives and questions

The primary research question has been formulated as follows:

How does the inclusion of timber creep influence the modelling and assessment of urban quay walls

For this study, the structural behaviour concerns force distribution within the foundation piles as well as the horizontal displacement of the quay wall. The new insights obtained from this study are to help better assess the remaining safety of quay walls. For the modelling of quay walls, the Embedded Beam Row of Plaxis 2D has been used, as it has been suspected this feature allows for numerically cheap computations. To achieve the main question, of what is the influence of timber creep on quay walls, the following secondary research questions have been formulated:

1. *To what extent is the Plaxis 2D Embedded Beam Row adequate for modelling the structural behaviour, that is force distribution and displacements, of laterally loaded foundation piles in multi-layered cohesive and non-cohesive soils?*
2. *What is the influence of timber creep on the structural behaviour of quay walls?*
3. *How is the creep behaviour affected by the the time step discretisation?*

2

Literature Study

2.1. Quay walls

Quay walls are a result of maritime trade (Gijt, 2010). Quay walls allowed for a faster transfer of goods from and to ships. The oldest version of a brick quay wall that has been found dates back to 2400 BC, found in India. However, wooden sheet piles date back even further. Civilisations with maritime trade networks would construct quay walls to maximize profit. For the Netherlands, construction of quay walls increased significantly in the 14th and 15th century, as a result of urbanisation and the increased trade in the Baltic sea (Verkuil et al., 2011). In the 16th century, especially during the Dutch Golden Age, international trade flourished, which in turn resulted in a larger amount of quay walls. These would be repaired or replaced throughout the ages, but most Dutch cities still have an infrastructure which partially consists of quay walls.

The function of a quay wall is, as already said in the previous section, to allow for a quick transfer of goods from and to ships. The main structural function of a quay wall however is to provide horizontal earth retainment. A large part old inner-city quay walls consists of a brick wall on a wooden relieving floor, supported by multiple pile rows. These piles are to provide lateral resistance, as horizontal earth pressure tries to push away the top section of the quay wall. Therefore, the modelling of these types of quay walls includes the problem of laterally loaded piles.

2.2. Single laterally loaded pile

In multiple cases, foundation piles have to withstand horizontal loads acting on the superstructure above. Causes of these horizontal loads can originate from for example wind, water or, in the case of quay walls, lateral earth pressures. Designers often take this into account by applying a rake to the piles. By doing so, the axial force in the pile is capable of providing a lateral resistance. When this is not the case, the piles bend in order to carry the load. The piles transfer the load into the soil, creating shear zones on the passive side of the pile. The volume enclosed by these shear zones are referred to as passive soil wedges, of which an illustration is provided in Figure 2.1.

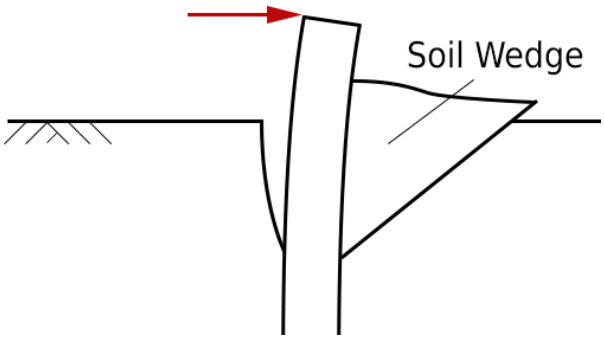

Figure 2.1: Soil wedge providing resistance to laterally loading of pile

Several design methods have been developed for laterally loaded piles. One of the more common methods is the one developed by Brinch-Hansen (1961). Based on the principle of the soil wedge and the corresponding force equilibrium, he formulated an ultimate limit state model. As input parameters, the model requires the effective friction angle, cohesion and specific weight of the soil, as well as the pile diameter and possible overburden pressure. The ultimate soil pressure varies over depth and can make jumps around transitions of soil layers. By dividing the pile in small elements and calculating the force equilibrium of each corresponding soil wedge, the ultimate load of the pile-system can be determined. The force equilibrium of the soil wedge as proposed by Brinch-Hansen (1961) is presented in Figure 2.2

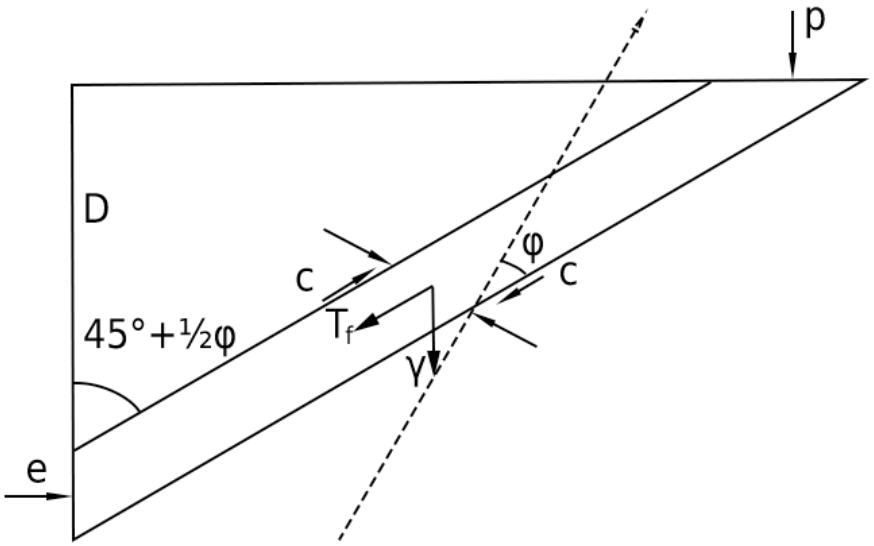

Figure 2.2: Force equilibrium soil wedge (Brinch-Hansen, 1961)

The Brinch-Hansen method is often used in combination with a Winkler beam, or beam on elastic foundation. The FEM software D-Sheet Piling by Deltares provides a Single Pile Module, in which this combination has been applied. The foundation, in this case the soil, is modelled as linear-elastic perfectly plastic. The stiffness in the elastic branch is based on the Ménard stiffness. The plastic limit is equal to the ultimate soil resistance as determined by Brinch-Hansen. A drawback of this method is that the soil stiffness has been schematised as linear elastic, whereas in reality a nonlinear stiffness is observed. Furthermore, the Brinch-Hansen model is an ultimate limit state model. This means that less information can be obtained regarding for example the serviceability limit state.

Another method that has been developed for the design of laterally loaded piles is the P-y curve method. The P-y curve method employs a Winkler beam with nonlinear springs, with varying stiffnesses over depth. The values for these springs have been determined based on full-scale pile testing. Hence, different P-y curves have been developed for different soils. An example of a P-y curve can be found in Figure 2.3. The software packages LPile and PyPile, which will both be mentioned in this report, use the P-y method for calculations. One difference between the software is that LPile uses finite difference, whereas PyPile is based on finite elements.

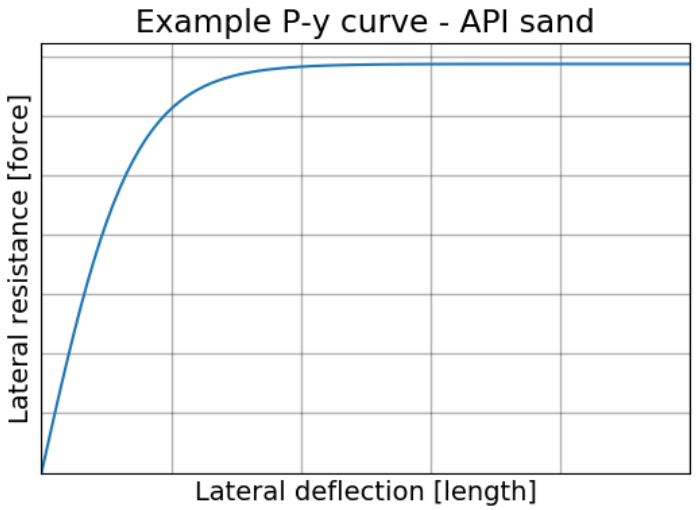

Figure 2.3: Example API sand P-y curve

2.3. Laterally loaded pile groups

The problem of the laterally loaded pile becomes more complex when looking at groups. For laterally loaded pile groups, high levels of interaction can occur. A proposed method to take into account group interaction is to create a coupled Winkler system, which has been illustrated in Figure 2.4.

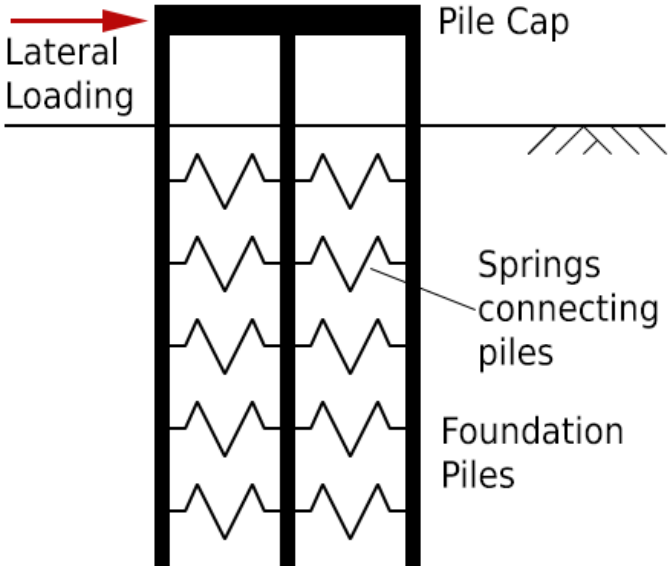

Figure 2.4: Example coupled Winkler beams in order to model laterally loaded pile groups

Two major aspects of the group interaction, or group effects, are the shadow and edge effects. The resistance of laterally loaded piles consists of the weight of passive soil wedges. However, for closely-grouped piles, it is possible these soil wedges to start overlapping one another. In this case, a reduction of the resisting soil weight has to be taken into account, as the same soil cannot contribute to the resistance of a pile twice. If the overlap occurs between piles in a row parallel to the plane of loading, this is called shadow effect. In the case that the overlap occurs between piles in a row perpendicular to the plane of loading, this is called an edge effect. Both principles have been illustrated in Figure 2.5. The severity of the group interaction is dependent on the relative centre-to-centre distance between piles, or relative pile spacing, expressed in equivalent pile diameter.

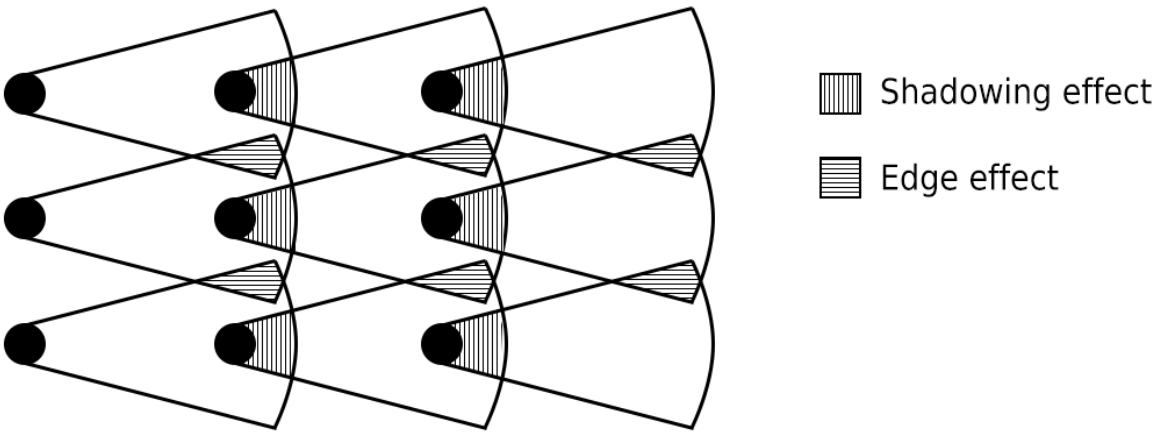

Figure 2.5: Group effects laterally loaded pile group

One method of studying the influence of the group effects is by calculating efficiencies. The efficiency of a group is defined as follows:

$$Efficiency = \frac{F_{total}}{n_{piles} F_{single\,pile}} \tag{2.1}$$

With:

- F_{total}: total load applied to the pile group at certain displacement [force]
- $F_{single\,pile}$: load applied to a single pile at certain displacement [force]
- n_{piles}: number of piles within the group

The group efficiency can be described as the ratio of the load the group carries, divided by what an equivalent single pile would carry at the same displacement and multiplied with the total number of piles. An alternative definition would be the average pile load within the group divided by the pile load of a single pile, given the same displacement.

For most cases, the group efficiency is less than 1. The lower efficiency is often caused by the earlier mentioned shadow and edge effects. The efficiencies tend to decrease for increasing displacements, as the mobilised soil wedges grow and start overlapping more. Several formulae have been created to predict efficiency of a group. Not only can these be used on the group as a whole, but also to estimate the efficiency of each individual pile, depending on among other things the centre-to-centre distance and location of the pile within the group. The applied efficiencies are in that case called P-multipliers, as it reduces the load P that can act on a pile. The relations for the P-multipliers are often obtained from tests carried out on pile group, similar to how P-y curves are determined based on pile testing. Several software packages use P-multipliers to model laterally loaded pile group. One example is the software GROUP, which will be discussed later.

2.4. Plaxis 2D

For the modelling of the soil, use will be made of Plaxis. Plaxis is a Finite Element Method software specialised in the modelling of soil behaviour, as well as soil-structure interaction. It allows for more advanced soil models compared to other FEM packages. Two options for Plaxis are available, the 2D and 3D version. For this research, it has been decided to use the 2D version of Plaxis. It is likely that a 3D model would provide more realistic results. Group interaction such as the edge effect mentioned earlier would for example be likely modelled more accurate using 3D modelling as compared to 2D. However, using 3D volume elements would increase computation time significantly. By switching from 2D plane elements to 3D volume elements, the amount of nodes increases. Moreover, the amount of degrees of freedom increase per node. Both aspects contribute to a relative large increase in the system of equations that has to be solved by the program, depending on which type of elements are used. Hence, it has been opted to use the 2D version of Plaxis. This version provides 2 types of model, the plane-strain model and the axisymmetric model. A quay wall can be

schematised as a structure with repetition in one direction, in the direction parallel to the water. Therefore, one method of modelling the quay walls is using plane-strain elements. One aspect of the quay wall that is not truly 2D is the foundation piles it is standing on. Multiple solutions have been proposed to model foundation piles. For this research, the Embedded Beam Row has been used, which will be treated in the next section.

2.5. Embedded Beam Row

The Embedded Beam Row (abbreviated: EBR) is a structural element implemented in Plaxis 2D, which aims to model an equally-spaced pile row going into the out-of-plane model. It functions by generating Mindlin beam elements not in the plane of the 2D mesh, but rather on top of it, making it sometimes called a "2.5D" model. The beam elements have individual nodes, but they do align with those of the underlying soil mesh. The stiffness properties of the beam elements take into account the pile spacing, as the software determines a stiffness per unit length. The beam nodes are connected via springs in both horizontal and vertical direction, modelling the shaft resistance. An additional spring is placed at the tip of the pile. The EBR can be compared to modelling reinforced concrete in plain strain; the rebar can be modelled in an identical way as the EBR by putting beam elements over the mesh and connecting it via springs. A visualisation of the EBR concept can be found in Figure 2.6.

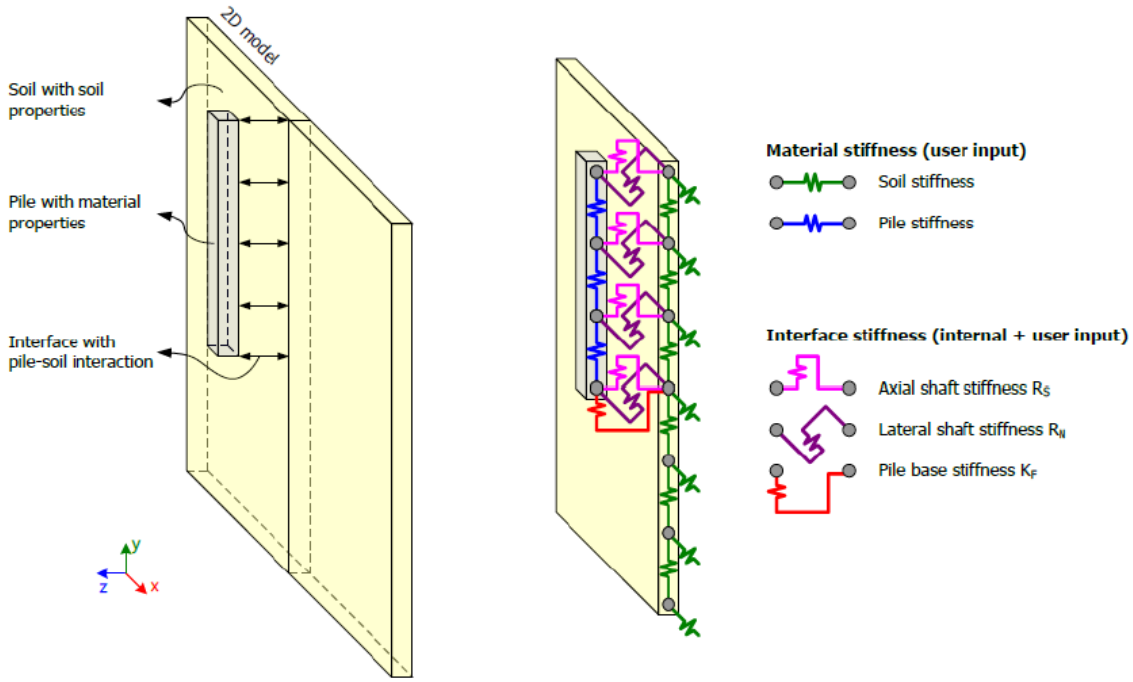

Figure 2.6: Schematisation Embedded Beam Row model (Sluis, 2012)

The traction in between the soil and pile is calculated via the following constitutive equation:

$$\begin{bmatrix} t_s \\ t_n \end{bmatrix} = \begin{bmatrix} K_s & 0 \\ 0 & K_n \end{bmatrix} \begin{bmatrix} u_s^p - u_s^s \\ u_n^p - u_n^s \end{bmatrix} \tag{2.2}$$

With:

- t_s: traction in axial direction $[kN/m/m']$
- t_n: traction in lateral direction $[kN/m/m']$
- K_s: elastic shear/axial stiffness $[kN/m^2/m']$
- K_n: elastic normal/lateral stiffness $[kN/m^2/m']$
- u^p: displacement pile node $[m]$
- u^s: displacement soil node $[m]$

The spring stiffnesses are calculated as follows:

$$
\begin{aligned}
K_s &= ISF_{RS}\frac{G_{soil}}{L_{spacing}} \\
K_n &= ISF_{RN}\frac{G_{soil}}{L_{spacing}} \\
K_{foot} &= ISF_{KF}\frac{G_{soil}R_{eq}}{L_{spacing}} \\
ISF_{RS} &= 2.5\left(\frac{L_{spacing}}{D_{eq}}\right)^{-0.75} \\
ISF_{RN} &= 2.5\left(\frac{L_{spacing}}{D_{eq}}\right)^{-0.75} \\
ISF_{KF} &= 25\left(\frac{L_{spacing}}{D_{eq}}\right)^{-0.75}
\end{aligned}
\tag{2.3}
$$

With:

- ISF_{RS}: Interface Stiffness Factor axial spring [-]
- ISF_{RN}: Interface Stiffness Factor lateral spring [-]
- ISF_{KF}: Interface Stiffness Factor foot spring [-]
- G_{soil}: shear stiffness surrounding soil [kPa]
- $L_{spacing}$: out-of-plane centre-to-centre pile spacing [m]
- R_{eq}: equivalent pile radius [m]
- D_{eq}: equivalent pile diameter [m]

The Interface Stiffness Factors can be overridden by the user, in order to fit the numerical results to for example field tests. The default values have been based on the validation performed by Sluis (2012), which consisted of uniform non-cohesive soils. Hence, the default values have not been validated for other cases such as cohesive multi-layered soils, as are present in Amsterdam.

The EBR had originally been designed in order to model vertically loaded piles, but users have tried using it for laterally loaded piles as well. The initial validation of the model was done by Sluis (2012), who compared the numerical results of the EBR to a 3D model. Furthermore, they modelled the same situation using 2D plate elements, which was the then most commonly used method for plane-strain modelling. The EBR results were in line with the 3D results and performed better than the other 2D options. The initial model did not include a plastic slider for the beam row, giving it unlimited lateral resistance. However, this would be implemented in a later iteration of the EBR.

Prior to the Embedded Beam Row, two common methods to model laterally loaded piles in Plaxis 2D were using anchors or plate/volume elements. Anchors can only be used to introduce the lateral resisting force that would occur at the pile head. However, there is no further interaction with the soil, as there is no volume within the model. Moreover, no structural forces such as bending moments can be derived directly from an anchor model. When using plate elements, structural forces can be derived directly. In contrast to the anchor, the plate elements take into account interaction with the soil. As a result though, the mesh becomes discontinuous, as the soil cannot flow through the plate element. The Embedded Beam Row has tries to incorporate the positive features of both methods. It incorporates the pile-soil interaction while allowing the mesh to remain continuous. Furthermore, the EBR calculates structural forces within the pile.

2.6. Timber creep

The time-dependent behaviour of timber structures had already been reported on in the 18th century, when Buffon (1741) experimented with wooden beams under different loading. He noted how the time to rupture would change depending on loading. Nearly a hundred years later, Vicat (1834) concluded one of the first studies on the creep phenomena, in his case concerning steel cables. At the end of the 19th century, Thurston (1895) would propose the creep curve as presented in Figure 2.7, which is still being utilised today. Since then, multiple studies have been carried out concerning creep in timber. Several aspects have been studied, such as stress level, type of loading, wood species and atmospheric conditions. Most creep tests have been carried out for up to 1 or 2 years, with relatively few test lasting 10 years (Gressel, 1984) (Holzer et al., 1989).

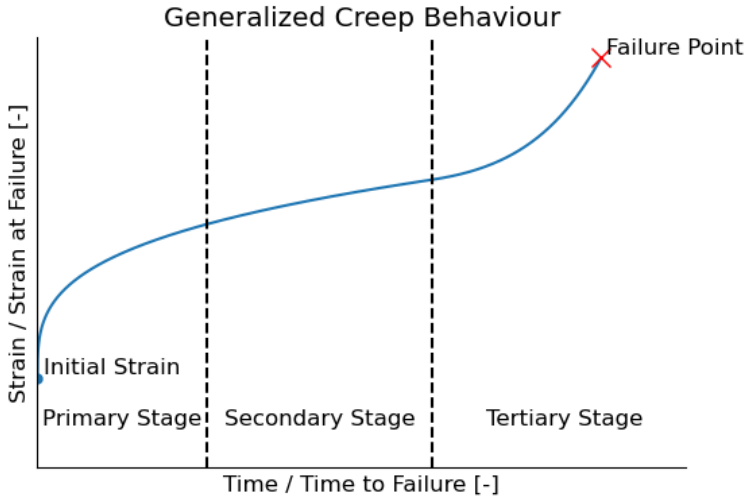

Figure 2.7: Creep curve as proposed by Thurston (1895)

2.7. Modelling creep using pseudo-elasticity

At the time of writing, Plaxis has not incorporated a visco-elastic material for the Embedded Beam Row, or a user-defined material at that. The only available materials are linear elastic, elasto-plastic and a custom moment-curvature diagram. Hence, a different method must be used in order to implement the timber creep. For this, it has been decided to use the method of effective E-modulus. In concrete design, this method is already employed for estimating the creep deformation (Walraven and Braam, 2018). For concrete, the following equations are used to determine the long-term strain (leaving out the shrinkage term):

$$\begin{aligned}
\varepsilon_c(t) &= \varepsilon_{ce} + \varepsilon_{cc}() \\
&= \sum_{i=0}^{n} \frac{1}{E_c}\left(\Delta\sigma_i\left(1+\varphi(t,t_i)\right)\right) \\
If\ t \to \infty: & \\
\varepsilon_c(t\to\infty) &= \varepsilon_{ce} + \varepsilon_{cc}(t\to\infty) \\
&= \sum_{i=0}^{n} \frac{1}{E_c}\left(\Delta\sigma_i\left(1+\varphi(\infty,t_i)\right)\right) \\
\sum_{i=0}^{n} \Delta\sigma_i &= \sigma_\infty \\
&\downarrow \\
\varepsilon_c(\infty) &= \frac{1}{E_c}\sigma_\infty\left(1+\varphi_\infty\right) \\
&\downarrow \\
E_c' &= \frac{E_c}{1+\varphi_\infty}
\end{aligned} \tag{2.4}$$

With:

- ε_c: Total concrete strain[-]
- ε_{ce}: Elastic concrete strain[-]
- ε_{cc}: Concrete creep strain[-]
- $\Delta\sigma_i$: Stress increment $[MPa]$
- n: Number of stress increments [-]
- E_c: Initial elastic modulus concrete $[MPa]$
- φ: Creep coefficient, dependent on cross-section, concrete strength class, cement type, relative humidity and concrete age [-]
- φ_∞: Creep coefficient at t=∞ [-]
- E_c': Effective elastic modulus $[MPa]$

In timber engineering, a similar approach is used (Ravenshorst et al., 2016), with the effective elastic modulus defined as follows:

$$E_{fin} = \frac{E}{1+k_{def}} \tag{2.5}$$

With:

- E_{fin}: Effective elastic modulus timber after a long period of time $[MPa]$
- E: Initial elastic modulus timber $[MPa]$
- k_{def}: Deformation factor to account for creep, to be determined using Eurocode, dependent on surrounding climate and load duration class $[-]$

Both methods however take only two moments in time into account, namely t=0 and t=∞, in which for the latter it is unclear at which moment the time can be considered as ∞. This method, easy in use, provides little insight in the structural behaviour during the service lifetime. The method effective E-modulus can be extended by using varying creep coefficients in the formulae above.

2.8. Implementation pseudo-elasticity in Plaxis 2D

The structural behaviour as function of time can be modelled by performing calculations in Plaxis, with different creep factors for different time steps. However, simply reducing the E-modulus will not cause a change in results (Bentley Systems, 2013). In this case, the calculations in Plaxis use two errors to compare to the tolerance provided by the user, namely the global error ϵ_{global} and Additional Error Check. These are defined as (Plaxis, 2019a):

$$\begin{aligned} \epsilon_{global} &= \frac{\sum ||Out\ of\ balance\ nodal\ forces||}{\sum ||Active\ loads|| + CSP \cdot ||Inactive\ loads||} \\ CSP &= \int \frac{\Delta\varepsilon \cdot \Delta\sigma}{\Delta\varepsilon D^e \Delta\varepsilon} \end{aligned} \tag{2.6}$$

$$AEC = \frac{max\ ||Out\ of\ balance\ structure\ nodal\ moments||}{max\ ||Structure\ nodal\ moments||} \tag{2.7}$$

With:

- Out of balance nodal forces: the difference between the external loads and the forces that are in equilibrium with the current stresses
- Active loads: load difference between current and previous calculation phase
- Inactive loads: active loads from the previous phase
- CSP: current stiffness parameter
- Out of balance structure nodal moments: out if balance moment of the structure nodes
- Structural nodal moments: bending moment obtained from stress integration

Both errors use force as a measurement. When changing the E-modulus of a material, neither the nodal forces or structure nodal moments are being updated. With no forces or moments being updated, and an equilibrium having been found in the previous phase, no calculation will be initiated. Plaxis only initiates calculation when there are too much out of balance nodal forces or moments. Bentley Systems (2013) mentions that reducing the strength of a material can lead to increased displacements. This can be done by looking at the equations defining the Embedded Beam Row elements, which are modelled as Timoshenko beam elements. The kinematic, constitutive and equilibrium equations for Timoshenko beam elements are as follows, with sign convention as shown in Figure 2.8:

$$\begin{aligned} w &= w \\ \frac{dw}{dx} &= \gamma - \varphi \\ \kappa &= \frac{d\varphi}{dx} \end{aligned} \tag{2.8}$$

$$\begin{aligned} M &= EI_{zz}\kappa \\ V &= GA_{eff}\gamma \\ &= \frac{EA_{eff}}{2(1-\nu)}\gamma \end{aligned} \tag{2.9}$$

$$\begin{aligned} V &= \frac{dM}{dx} \\ q &= -\frac{dV}{dx} \end{aligned} \tag{2.10}$$

With:

- γ: rotation due to shear [−]
- φ: rotation due to bending [−]
- E : Elastic Young's modulus [MPa]
- I_{zz}: relevant second moment of area [m^4]
- G : shear modulus [MPa]
- A_{eff}: effective shear cross-section [m^2]
- ν: Poisson's ratio [-]

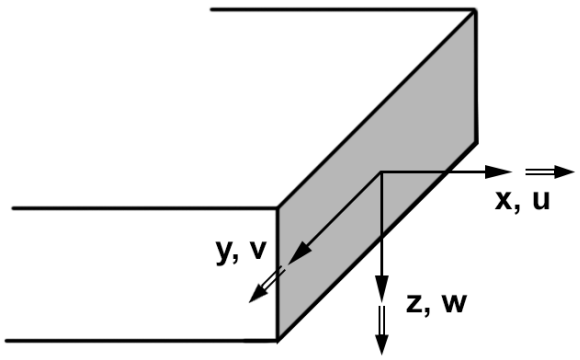

Figure 2.8: Sign convention beam, with location, displacement as indicated

A strength reduction is to be introduced in the constitutive equations shown in Equation 2.9. For the Embedded Beam Row, as well as plate materials, this can be accomplished by introducing a custom moment-curvature diagram, effectively reducing the bending stiffness of the beam. Substitution of the effective E-modulus into Equation 2.9 results in:

$$\begin{aligned} E' &= \frac{E_0}{1+\varphi} \\ M &= E' I_{zz} \kappa \\ &= \frac{E_0}{1+\varphi} I_{zz} \kappa \\ V &= \frac{E' A_{eff}}{2(1-\nu)} \gamma \\ &= \frac{E_0 A_{eff}}{2(1-\nu)(1+\varphi)} \gamma \end{aligned} \tag{2.11}$$

With:

- E': effective E-modulus [MPa]
- E_0: initial E-modulus [MPa]
- φ; creep factor, dependent on creep law [-]

The creep factor use for the effective modulus is dependent on which creep law is being used. Several creep laws have been formulated and tested for wood. In general, the power law, based on empiric relations, provides a good approximation of the creep behaviour of timber structures, using the following form (Gressel, 1984):

$$\epsilon(t) = \epsilon_0 + A * t^m \tag{2.12}$$

With:

- ε: total deformation [m]
- ε_0: intercept of a line parallel to the secondary stage in the creep, as seen in Figure 2.7, Page 9. This value is close, but not equal to, the initial deformation [m]
- m: slope constant [-]
- A: scale factor [m]

However, in the case of the laterally loaded piles, with complex pile-soil interaction, no proper creep law had been found that can be implemented. Hence, as of now, this method will provide moments, or snapshots, in time. The chronological order of these snapshots is known. Nevertheless, without a proper creep law, their position in real-time as well as the time relative to each other, is unknown.

Concerning the implementation in Plaxis 2D, a stiffness reduction is to be applied by using the custom moment-curvature diagram feature. By reducing the stiffness, Plaxis will register a violation of the strength criterion in the Embedded Beam Row, increasing the error. If the error is large enough, it will trigger Plaxis to perform calculations. The material behaviour can be considered as Linear Elastic Perfect Plastic, which could be described using three points. However, the linear elastic part has to be discretised. First of, the first part of the M-kappa diagram is considered to be elastic, hence it is not taken into account when calculating internal forces for the force equilibrium. Secondly, it seems the new moment must be outside the of the discretised segment of the old moment-curvature diagram, as depicted in Figure 2.9. If the steps in the discretised moment-curvature diagram are too large, there is a possibility Plaxis will not recalculate displacements due to the stiffness reduction.

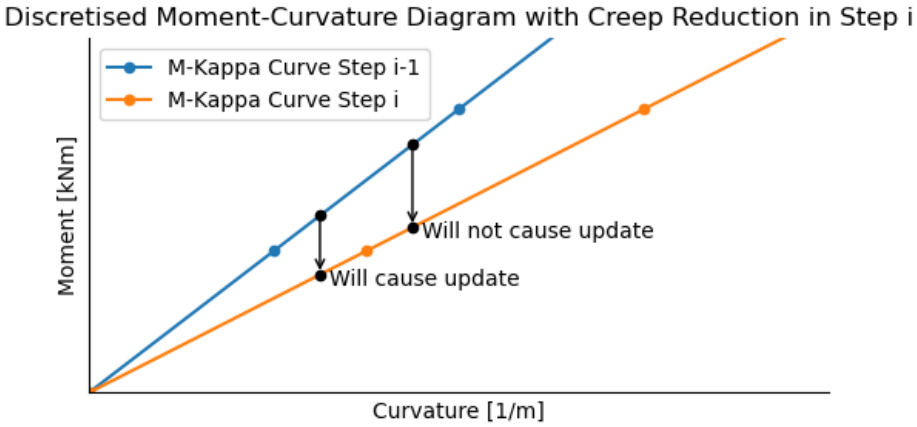

Figure 2.9: Influence of the discretisation of the moment-curvature on whether Plaxis updates displacements

2.9. Influence of bending stiffness on pile behaviour

In the previous sections, it has been discussed to model creep behaviour of the wood by changing the bending stiffness. However, several studies have shown the influence of the bending stiffness on the behaviour of laterally loaded piles (Poulos and Davis, 1980) (Banerjee and Davies, 1978). In order to normalise the pile stiffness, use has often been made of the relative pile flexibility ratio defined as follows:

$$K_{rc} = \frac{E_p I_p}{E_s L^4} \tag{2.13}$$

With:

- E_p: elasticity modulus of the pile $[kPa]$
- I_p: moment of inertia of the pile $[m^4]$
- E_s: average soil elasticity modulus $[kPa]$
- L: embedded pile depth $[m]$

The pile is defined as rigid when $K_{rc} > 10^{-2}$ and flexible otherwise. Banerjee and Davies (1978) reported how the pile stiffness has an influence on the normal pressure and moment distribution along laterally loaded piles, as presented in Figures 2.10 and 2.11. In these figures, it can be seen how a reduced stiffness can lead to higher soil pressures and lower bending moments. This might suggest that using pseudo-elasticity might not model creep, but general laterally loaded pile behaviour as presented in these figures. Yet, it must be noted the difference in stiffness in Figures 2.10 and 2.11 are of a factor 1000, as K_r goes from 10^{-1} to 10^{-4}. In this study, a maximum creep factor of 1.6 has been used, which would result in a factor 2.6. Hence, it has been deemed unlikely that using pseudo-elasticity will give false results concerning creep behaviour.

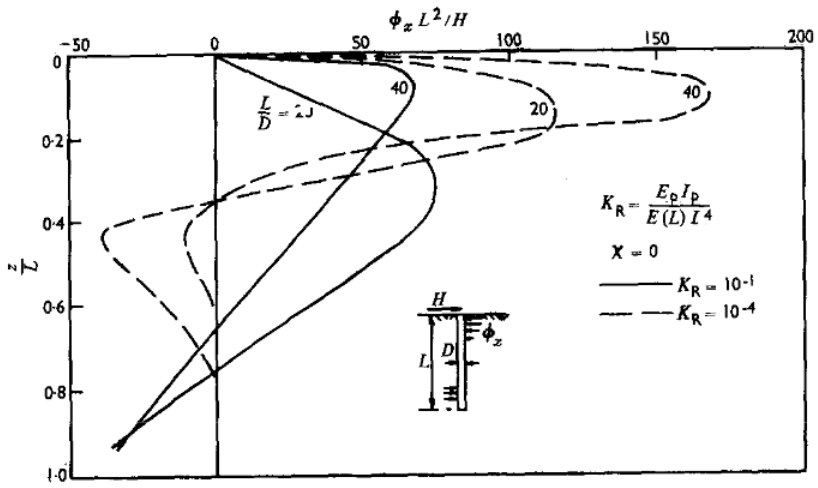

Figure 2.10: Normal pressure distributions along laterally loaded piles for different relative pile flexibility ratios and different soil homogeneities χ ($\chi = 0$: non-homogeneous soil, $\chi = 1.0$: homogeneous soil) (Banerjee and Davies, 1978)

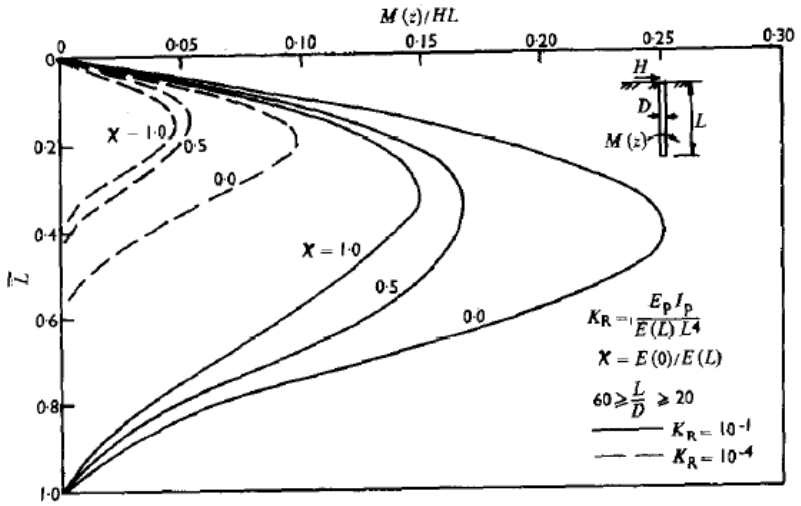

Figure 2.11: Moment distribution along laterally loaded piles for different relative pile flexibility ratios and different soil homogeneities χ ($\chi = 0$: non-homogeneous soil, $\chi = 1.0$: homogeneous soil) (Banerjee and Davies, 1978)

3

Embedded Beam Row Verification

The Embedded Beam Row has only developed a couple of years back in 2012 by Plaxis. Little to no case studies have been found that use the EBR to design or check a quay wall. Still, it has been opted to choose this method of modelling as opposed to the conventional ways of 2D modelling, which consists of either using plates or anchors. However, both of these methods have their own drawbacks, as described in Section 2.5, Page 7. These could be overcome by modelling in Plaxis 3D. This would seem to be the best solution, also considering the fact that the laterally loaded pile is a 3D problem. The resistance of the pile is often taken to consist of a soil wedge in 3-dimensional space, as stated by Brinch-Hansen (1961). However, it has been decided use Plaxis 2D, as the computation cost is lower.

No full-scale testing has been done on the Herengracht quay wall. Hence, it is not possible to perform a validation of the Embedded Beam Row model using data from this case. Therefore, it has been decided to model a field test of a laterally loaded pile group in cohesive soil to assess the quality of the EBR. The conclusions drawn from these results have been used to determine the applicability of the EBR.

For the reference case, the load test at Salt Lake City as reported on by Snyder (2004) has been used. The testing consists of the loading of both a single pile as well as a 3x5 pile group. The subsoil consists mainly of soft cohesive soils with sand layers embedded, similar to the Herengracht case. The remained of this chapter will provide a brief summary of the reference case study, the way of modelling and the corresponding results. Furthermore, the results will be analysed, upon which a conclusion will be drawn whether the Embedded Beam Row is accurate enough for the given application. For a full description of the case study, the input data, the modelling, calculations and results, see Appendix A, Page 72.

3.1. Field test data verification case

3.1.1. Description verification case

For the verification case, it has been decided to model a load test performed on a pile group in Salt Lake City, as reported by Snyder (2004). This test consisted of the loading of both a single pile as well as a 3x5 pile group. The soil composition consists of soft cohesive layers with embedded sand layers. Geotechnical data was available from both earlier tests as well as lab and fields tests during the project itself. Displacements, forces and rotations were measured and reported. Using the rotations, corresponding bending moments had been calculated. The single pile load test had been modelled afterwards with LPile, a software that uses P-y curves. The measurements of the group test had been validated using GROUP, a software that utilises P-y curves and P-multipliers, with the latter being calculated based on the measurements. A more elaborate description of the load test can be found in Appendix A, Page 72, or in the original report of Snyder (2004). An impression of the test setup is presented in Figures 3.1 through 3.3.

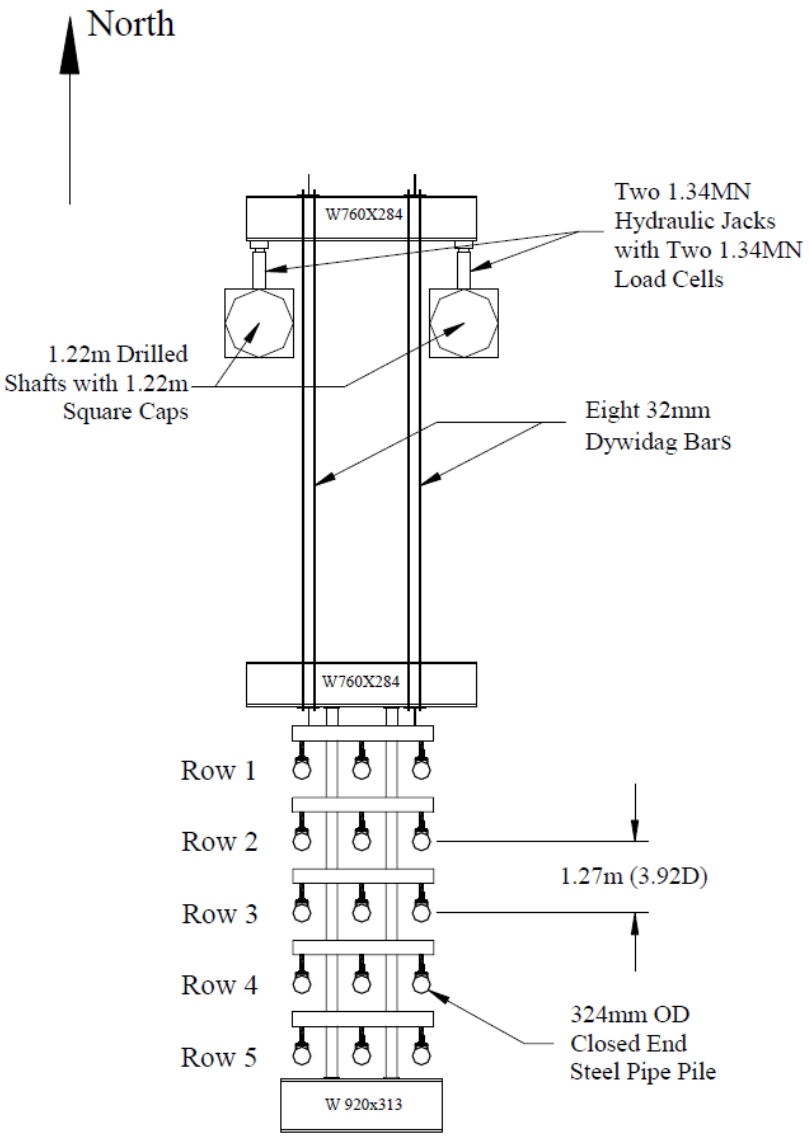

Figure 3.1: Topview pile group loading test Salt Lake City case (Snyder, 2004), with North row being row 1

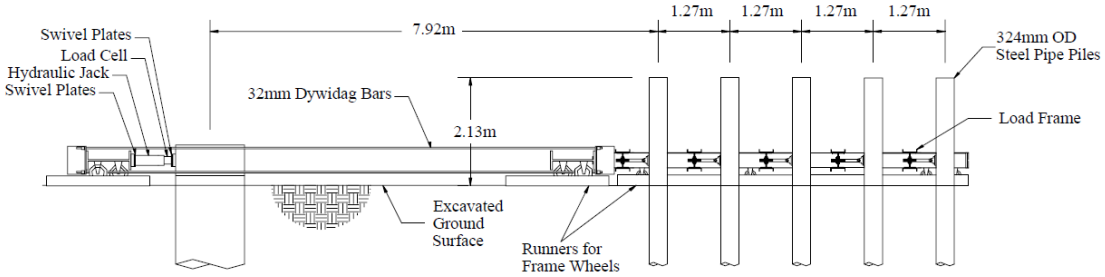

Figure 3.2: Side view pile group loading test Salt Lake City case (Snyder, 2004), with left row being row 1

(a)

(b)

Figure 3.3: Pile group loading tests Salt Lake City case (Snyder, 2004)

The soil profile of the site has been schematised as presented in Figure 3.4.

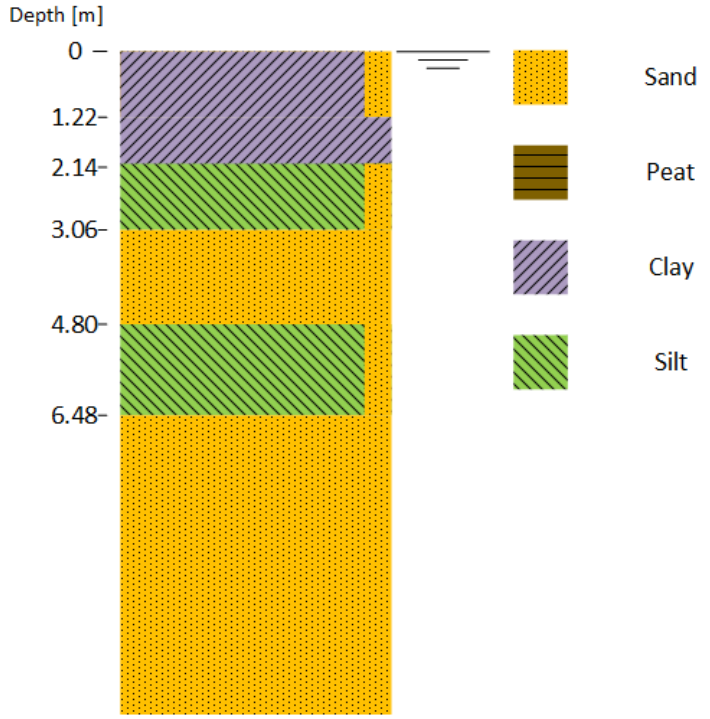

Figure 3.4: Idealised soil profile Salt Lake City case

Layer	**Depth bottom of layer** $[m]$
Sandy Lean Clay	1.22
Lean Clay	2.14
Sandy Silt	3.06
Silty Sand	4.80
Sandy Silt	5.33
Sandy Silt	5.87
Sandy Silt	6.48
Poorly Graded Sand	N.A.

Table 3.1: Schematised soil profile Salt Lake City case according to Snyder (2004).

3.2. Single pile modelling verification case

Part of the input of the Embedded Beam Row is the ultimate lateral resistance, which can vary over the length of the pile. This ultimate resistance had been implemented by Plaxis to limit the load piles can carry. The ultimate lateral resistance of the pile can be defined using results from field tests or pile modelling. For the Salt Lake City case, the resistance has been determined by modelling a single pile with the P-y curve method. The P-y curves had been calculated using the same input parameters as by Snyder (2004). The only difference in modelling was the software used; for the original report LPile had been used, whereas for this thesis the software PyPile has been used. As mentioned in Section 2.2, Page 3, the first one uses Finite Difference Method and the latter Finite Element Method.

3.2.1. Results single pile modelling verification case

The force-displacement curve obtained from PyPile has been plotted along with the measurements and well as the LPile results in Figure 3.5. In this figure it can be observed that the PyPile model provides a good fit with the measured data. The curve from PyPile appears to have a similar shape to the curve created by both the measurements as well as LPile, with only a slightly stiffer response.

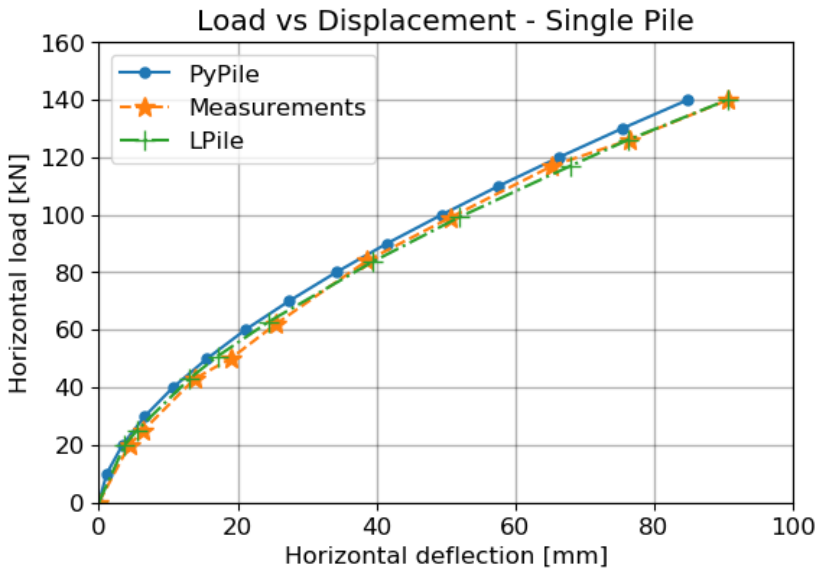

Figure 3.5: Force-displacement curve PyPile, compared to field measurement and LPile calculations, Salt Lake City case

Figure 3.6 shows the maximum bending moment as function of the applied load for PyPile, LPile and what had been measured. The figure shows that the data from both software packages coincide. However, for loads larger than 60 kN, both curves deviate from the measured data. In the original report, it had been stated that the strain gauges were malfunctioning or had been damaged. Still, both software packages overestimate the maximum bending moment with a maximum of 10% of what had been measured.

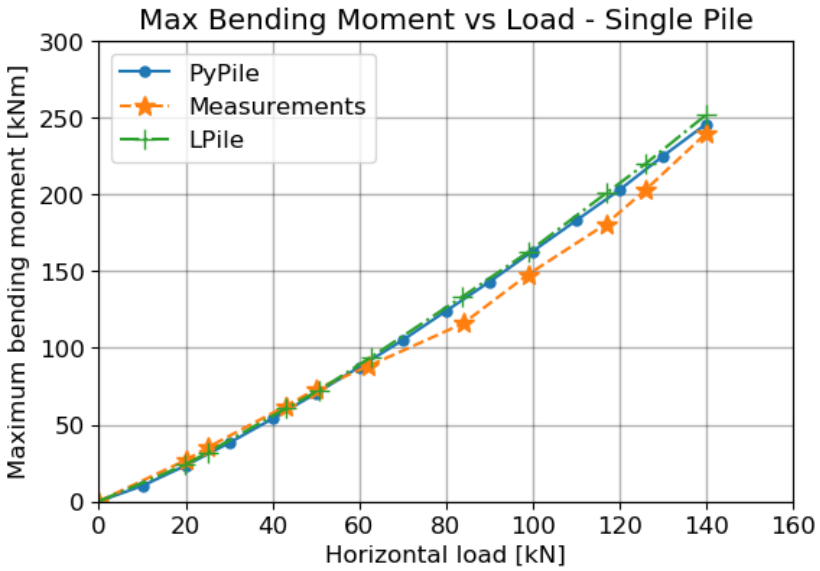

Figure 3.6: Moment-force curve PyPile, compared to field measurement and LPile calculations, Salt Lake City case

From both graphs it can be concluded that the PyPile model is capable of realistically modelling the single pile as had been tested at Salt Lake City. The force-displacement curve coincided with the results of the measurements, as well as the validation that had been performed using LPile. For the maximum bending moment, small discrepancies were found between software results and measurement data. However, difficulties had been reported during original testing, and the differences in values are within 10%. Hence, the current PyPile model will be used to model the input for the lateral resistance used by the Plaxis 2D model.

3.2.2. Ultimate lateral resistance

With the PyPile model validated, it can be used to determine the ultimate lateral resistance of the pile as function of depth. Multiple P-y curves show asymptotic behaviour, as for example the on presented in Figure 3.7a. As such, PyPile does not provide an ultimate lateral resistance. Instead, a large displacement has been applied on the soil, to obtain a load close to the ultimate limit state. At a certain point, a large increase in soil displacement provides a negligible increase in force. This has been illustrated in 3.7a as well. For the Salt Lake City case, a value for y of 100 mm has been chosen. The corresponding force over depth has been plotted in Figure 3.7b. As a validation that the values obtained for 100 mm displacement are near ultimate limit state, the force as function over depth for 200 mm soil displacement has been plotted alongside. As can be seen in the figure, the forces for 200 and 100 mm are nearly identical.

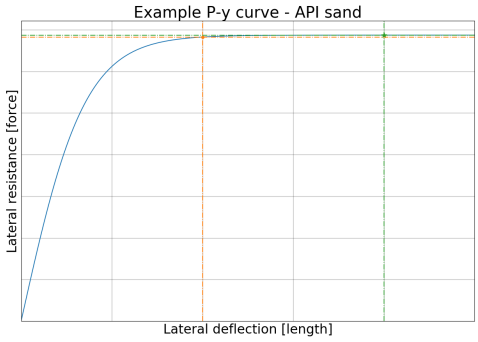

(a) Example API sand P-y curve

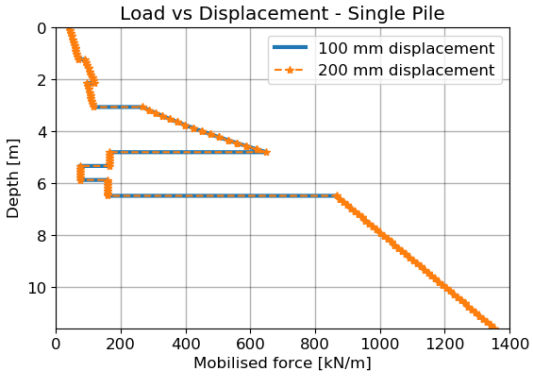

(b) Force acting on the pile over depth, given a displacement of 200 and 100 mm. The force acting at 100 mm functions as input for lateral resistance of the Embedded Beam Row in Plaxis 2D

3.3. Results Plaxis 2D modelling verification case

This section will discuss the results obtained from the Plaxis 2D modelling. For a full description on the input of the modelling, see Appendix A, 72.

Figure 3.8 shows the force-displacement curve of the whole group as calculated with Plaxis 2D, compared to the measurements, as well as the GROUP calculations performed by the original author. The figure showcases that the Plaxis model is less stiff compared to the measurements. For the first load step, the Plaxis model predicts a displacement 40% larger than had been reported. For increasing loads, the overestimate seems to stabilise to around 20%. The initial larger difference is likely due to installation effects. During driving of the piles, the surrounding soil is compressed. Later, during lateral loading, this compression helps increase the lateral resistance of the pile. The effect of the installation effect is most noticeable for small displacements. In Plaxis 2D however, there is no proven method of modelling these installation effects. The exclusion of installation effect can explain the initial larger difference in displacement at small loads.

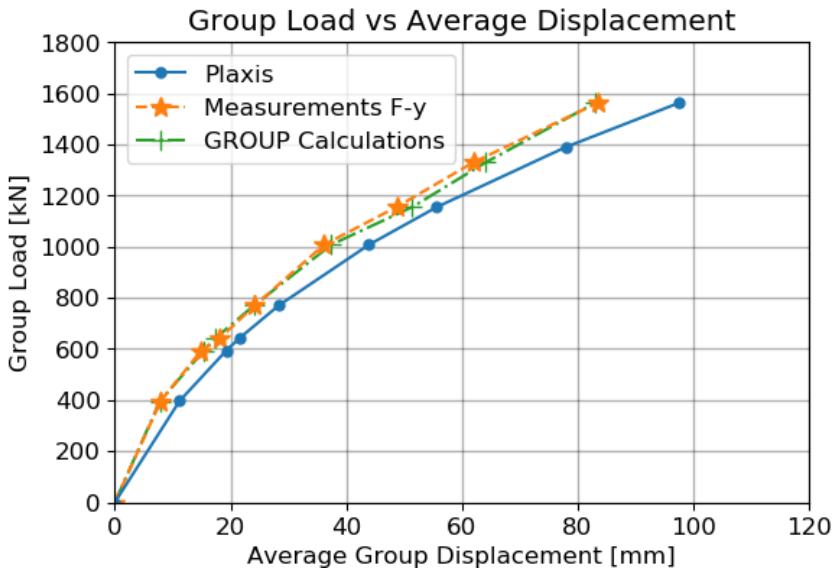

Figure 3.8: Load-displacement curve pile group, from Plaxis modelling and compared to measurements and GROUP calculations Salt Lake City case

Sluis (2012) suggests that the Interface Stiffness Factors, which are used to manipulate the stiffness of the interface connecting the beam to the soil, should be varied in order to fit Plaxis results to the measurements. For curve that can be seen in the figure, a value of 10 has been used for the lateral ISF. Testing has been done to try and obtain a better fit. Initially, a value of 1.194 had been used, which was the default value Plaxis provided as calculated using Equation to 2.3, Page 8. However, using this value resulted in an even less stiff response of the pile group. The default values for these factors had been derived by Sluis (2012) for a uniform sand layer. In the Salt Lake City case however, the top part of the soil mainly consists of cohesive clays and silts.

A separate test has been run using an Interface Stiffness Factor of 100. However, the results of this test were near identical to the ones obtained using a value of 10. This can be explained using Figures 3.9 and 3.10. In Figure 3.9, the left spring represents a simplified response of the soil body when a force is applied to it, assuming full elasticity. The right part represents the parallel system that connects the Embedded Beam Row to the soil body. In here, the spring at the top represents the interface stiffness, which is influenced by the Interface Stiffness Factor. The plastic slider at the bottom represents the ultimate lateral resistance, which is part of the user input. In this case, the input of the plastic slider has been determined using PyPile, as discussed in Section 3.2.2, Page 21. This spring-slider system is a schematisation of the total response of the Embedded Beam Row when subjected to a load. The total response thus consists of a series coupling of the interface elements as well as the soil body. This has been illustrated in Figure 3.10, where the first graph depicts the response of the soil body, the second one the response of the interface, and the last one the total response when put in a series coupling. At a certain point, the interface stiffness will become so high compared to the soil stiffness, that in Figure 3.9, it will act as if rigid. Hence, the Interface Stiffness Factors can only be varied for a certain range.

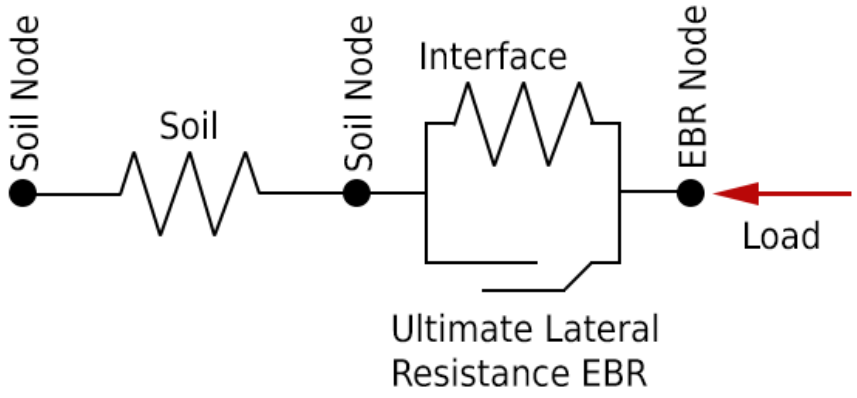

Figure 3.9: Schematisation of elasto-plastic model of the Embedded Beam Row, assuming simplified elastic soil response

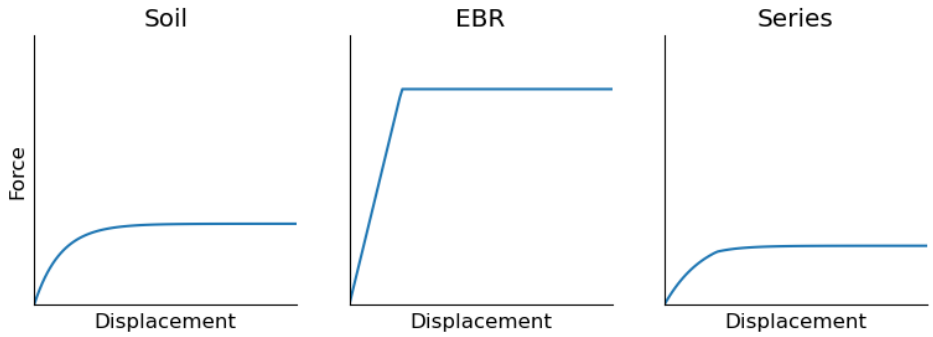

Figure 3.10: Schematisation of elasto-plastic response of the Embedded Beam Row

Figures 3.11a and 3.11b show the force-displacement curves averaged per row. Rows 2 through 4 showed behaviour similar to Row 1, in which the response was less stiff than had been measured. Figure 3.11b however displays that the trailing row carried more load in comparison to the measurements.

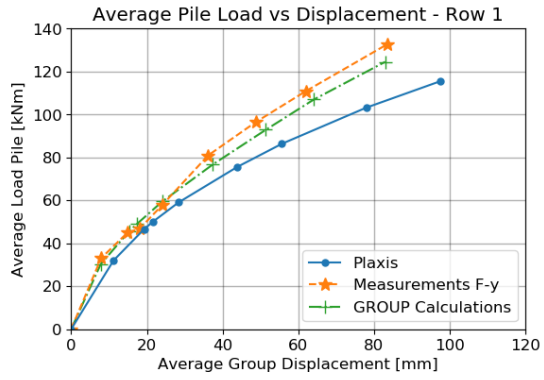

(a) Average pile load versus group displacement, row 1

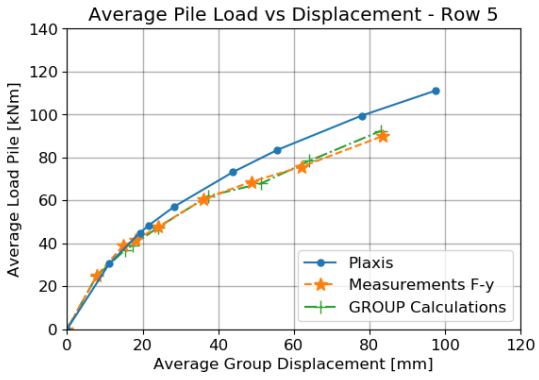

(b) Average pile load versus group displacement, row 5

Figure A.9 shows the efficiency of the group as a function of group average displacement. As has been defined in Section 2.3, Page 5, the efficiency has been defined as the total load carried, divided by the load a single pile would carry multiplied with the total number of piles. The figure shows how the measured efficiency starts just below 1 and decreases for increasing displacement. The decreasing efficiency is a sign of shadow and edge effects taking place. The curve corresponding to the Plaxis results however starts at around 0.7, to then increase until it approaches the measured efficiency. As mentioned earlier during the discussion of the force-displacement curves, the initially softer response is most likely caused by the lack of installation effects.

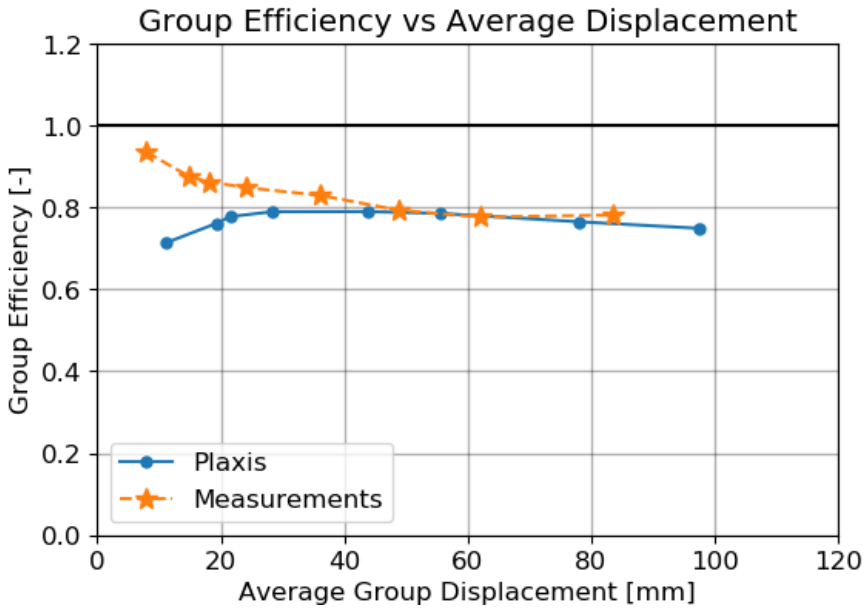

Figure 3.12: Group efficiency as function of displacement, from Plaxis modelling and compared to measurements of Salt Lake City case

Figures 3.13a and 3.13b show the efficiency per row, with the first one displaying the measurements and the second one those obtained from Plaxis. Figure 3.13a shows that the measured efficiency of the first row is larger than 1. First off, the front row experiences less influence of group effects reducing the resistance, as there is no shadowing. Additionally, at small displacements, edge effects have most likely not developed yet, especially for undrained loading. Secondly, the other rows most likely provide some sort of restraint on the front row.

Both the measurements as well as the Plaxis results show that the third row has a lower efficiency than the other centre rows, namely Rows 2 and 4. In the original report, it had been claimed this was unusual behaviour and suggested local soil variation caused this discrepancy. However, in the Plaxis model, the soil profile is considered to be constant in the horizontal plain. Still, the model reported a lower efficiency for Row 3. Hence, it is likely the measured data could have occurred for a constant soil profile.

As had been observed in the force-displacement curve in Figure 3.11b, Page 23, the trailing row carried more load in the Plaxis model relative to the measurements. It is unclear what causes this discrepancy. However, results have been compared to a different full-scale test, performed at the same site at Salt Lake City. This test consisted of a 3x3 driven pile group. as reported on by Rollins et al. (2003). The resulting row efficiencies have been presented in Figure 3.14. Here it can be seen the trailing row has a higher efficiency compared to the centre row, which is contrary to the results as reported by Snyder (2004). It is possible the difference in load carrying had been caused by local soil variation.

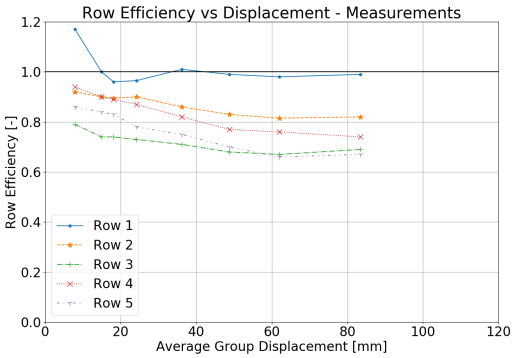

(a) Row efficiency, measurements

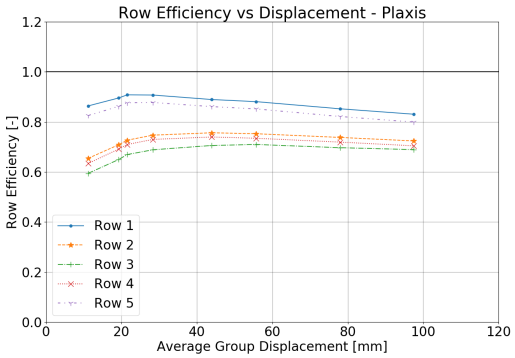

(b) Row efficiency, Plaxis results

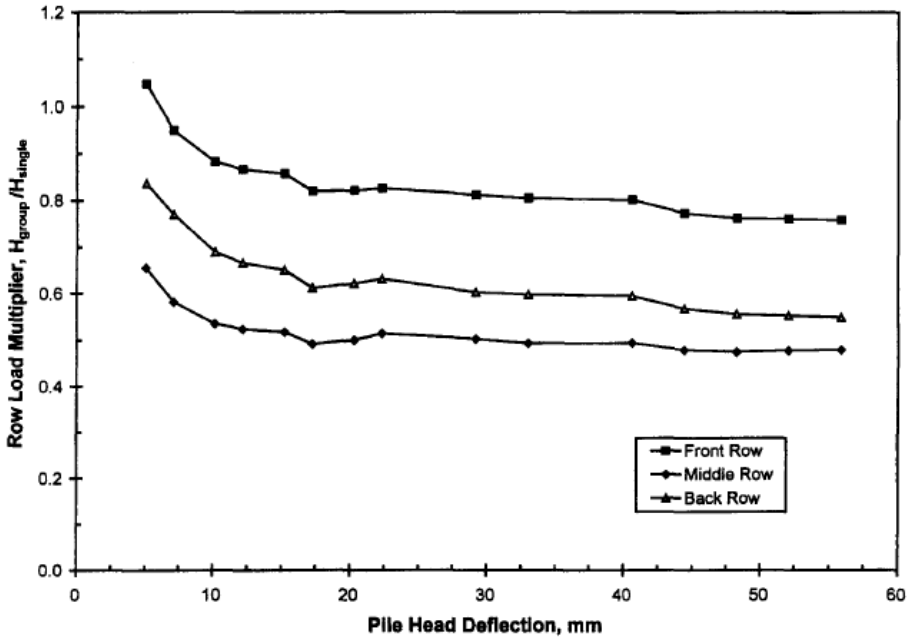

Figure 3.14: Row efficiency as function of displacement, from a 3x3 driven pile group tested at the Salt Lake City site (Rollins et al., 2003)

Figures 3.15a and 3.15b show the maximum bending moment in rows 1 and 5 as a function of the load carried, compared to the measurements and GROUP results. Rows 2 through 4 showed similar behaviour to row 1. In all cases, the maximum bending moment as reported by Plaxis is lower compared to both the measurements as well as the GROUP calculations. Rows 1 through 4 underestimates the maximum up to 30%. The fifth row however, underestimated the bending moment at times by 50%. Again, this shows the difference in efficiency of the last row between Plaxis and the measurements. In the Plaxis model, the trailing row seems to have a higher resistance to bending.

The lower maximum bending moment can also be observed in the original validation report of the Embedded Beam Row. In here, a laterally loaded pile group in soft clay had been modelled using Embedded Beam Rows, which was compared to a 3D embedded beam model as well as a 3D volume model. Figure 3.16 shows the bending moment over depth obtained during the validation. In the figure it can be seen the maximum bending moment obtained using the Embedded Beam Row is approximately 20 % lower.

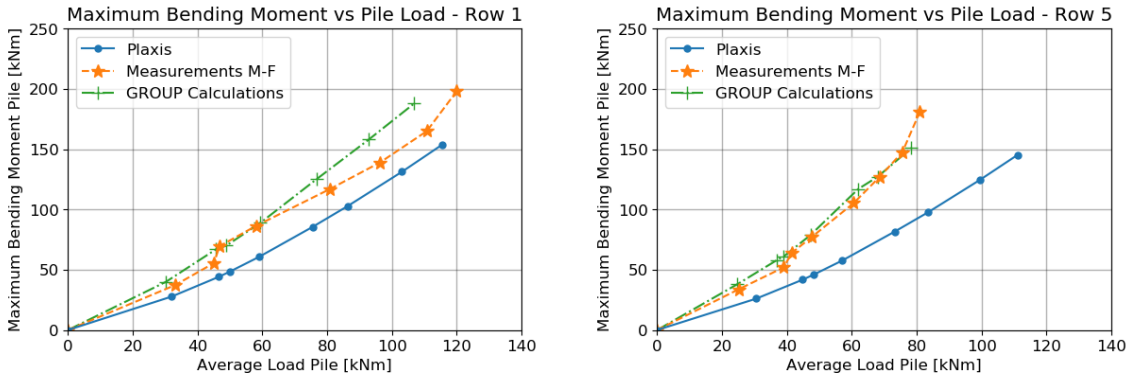

(a) Maximum bending moment versus average pile load, row 1

(b) Maximum bending moment versus average pile load, row 5

Figure 3.15: Moment-load curve averaged per pile row, from Plaxis modelling and compared to field measurements and GROUP calculations Salt Lake City case

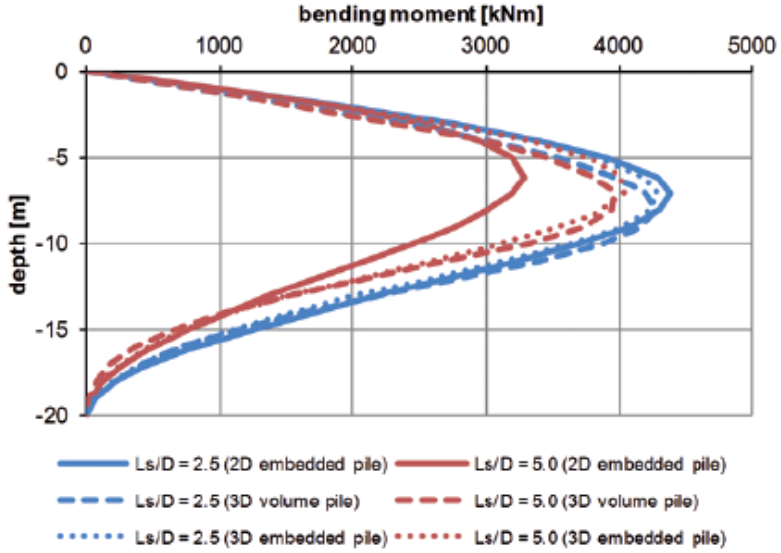

Figure 3.16: Bending moment over depth for a laterally loaded pile in soft clay, $L_{spacing}$/D=5.0, using 2D Embedded Beam Row, 3D Embedded Beam and 3D volume elements, as reported by Sluis et al. (2013)

Figures 3.17a and 3.17b shows the bending moment over depth for the first row, at a group load of 770 kN and at 1330 kN. Small values obtained from the measurements are prone to error, these values have been marked in red. In the figures, it can again be observed how Plaxis predict a lower maximum bending moment compared to the measurements. Furthermore, the location of the maximum bending moment is at a shallower depth. In Figure 3.16 the same phenomena can be observer. This could indicate that the top layers provide larger resistance than they did during the full-scale test. Additionally, the moments obtained from Plaxis do not change sign.

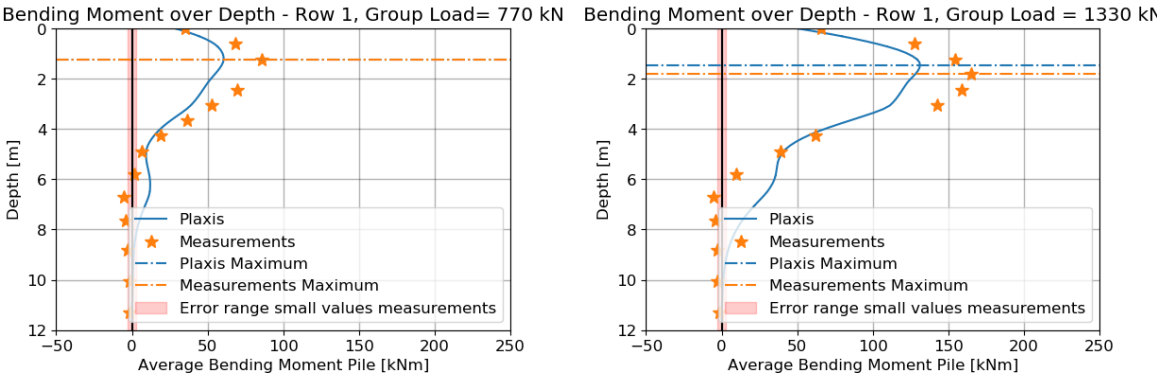

(a) Bending moment over depth, Row 1, Plaxis results compared to measurements, group load = 770 kN

(b) Bending moment over depth, Row 1, Plaxis results compared to measurements, group load = 1330 kN

3.4. Conclusion verification EBR

The Embedded Beam Row provided realistic results for the modelling of the Salt Lake City case. The force-displacement behaviour of the group as a whole approached the measured behaviour reasonably. The comparison of group efficiency showed that the accuracy was lower at smaller displacements. Where the measurements showed a high initial efficiency that decreased for growing displacements, the Plaxis model started at a low efficiency which gradually increased. This difference is likely due to installation effects, which as of time of writing cannot be modelled properly in Plaxis 2D using Embedded Beam Rows.

The Embedded Beam Row will likely underestimate the bending moments that occur in the pile. This has not only been found during this verification, but also in the one performed by Sluis (2012), which had been carried out for the implementation of the EBR. Furthermore, the location of the maximum moment is at a shallower depth than had been measured.

The default Interface Stiffness Factors provided by Plaxis have been deemed invalid in the current case. These default values had been based on tests performed in a uniform sand layer, and did not apply for the Salt Lake City pile test. The default values had been designed as a first estimate, but should be used to fit results to measured data. Nevertheless, during the Salt Lake City verification it had been discovered there is an upper limit to these values. Beyond this upper limit, the interface strings will act as rigid compared to the soil body, and no longer influence behaviour of the pile group.

The last aspect that has to be considered is whether the Salt Lake City case should be modelled using a plane-strain model. In this case, there are only three pile rows in the plane perpendicular of loading. When using the Embedded Beam Row, it is assumed that there are an infinite number of pile rows perpendicular to the plane of loading. From the results presented here it is possible to conclude that the Salt Lake City case was not a true 2D situation. It is plausible some of the discrepancies when comparing the results have been caused by the schematisation of the case using a 2D model.

3.5. Connection Herengracht case

It has been concluded that the Embedded Beam Row can be used to simulate a laterally loaded pile group up to some degree of accuracy. The results obtained using the EBR were realistic in comparison with those measured. The discrepancies found in the comparison of the results could be explained to a large extent. For the Herengracht case, there is no data to validate results with. Hence, it is sufficient for the EBR to provide realistic results. The following points can be taken into account for the modelling of the Herengracht case:

- The default Interface Stiffness Factors provided by Plaxis can be too low for cohesive layers
- For small displacements, the model can be less realistic, as efficiency can be much lower than in reality
- Bending moments obtained can be 20-30% lower than in reality. Furthermore, it is possible the depth of the maximum is deeper

4

Modelling Herengracht Case

In order to study the influence of the to be researched factors, a case study will be performed based on a quay wall at the Herengracht. This case has been chosen due to the relative high availability of soil data, both form field as well as lab tests. Furthermore, it lies in the historic city centre of Amsterdam, making it likely to be representative for a large portion of the quay walls.

4.1. Parameter set Herengracht case

4.1.1. Quay wall dimensions

This section provides properties on the dimensions and age of the quay wall. For the full determination of all parameters, see Appendix B, Page 102. The quay wall has been constructed in 1886. The following schematisation of the quay wall has been created:

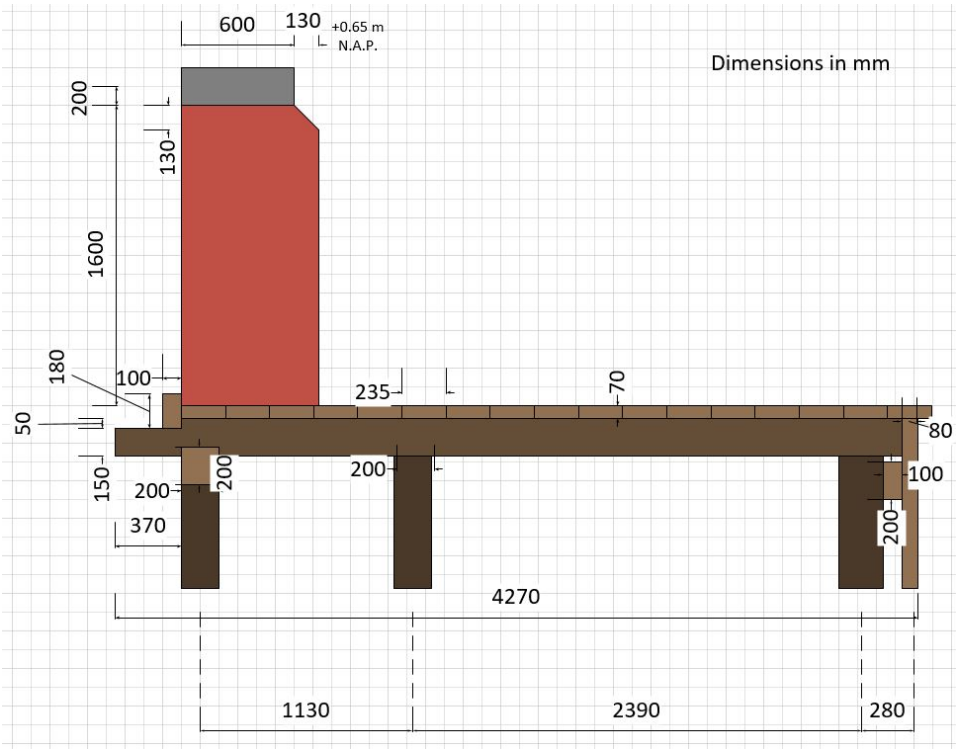

Figure 4.1: Schematisation cross-section quay wall Herengracht, dimensions in mm

Element	**Dimension**	**Value** [mm]
Pile spacing	Row 1-2	1130
	Row 2-3	2370
	Longitudinal	1000
Pile	Diameter	200
	Length	11 500
	Length embedded in first sand layer	500
Cross beam	Length	4180
	Width	250
	Height	200
Longitudinal beam	Width	90
	Height	200
Wall	Width bottom	730
	Height front	2000
Floor planks	Width	235
	Height	70
Retaining screen	Length	4000
	Height	70

Table 4.1: Main dimensions quay wall

4.1.2. Soil profile and parameters

This section provides an overview of all soil parameters used. For the full determination of all parameters, see Appendix C, Page 105. Based on drillings, the soil profile has been schematised as presented in Figure 4.2 and Table 4.2.

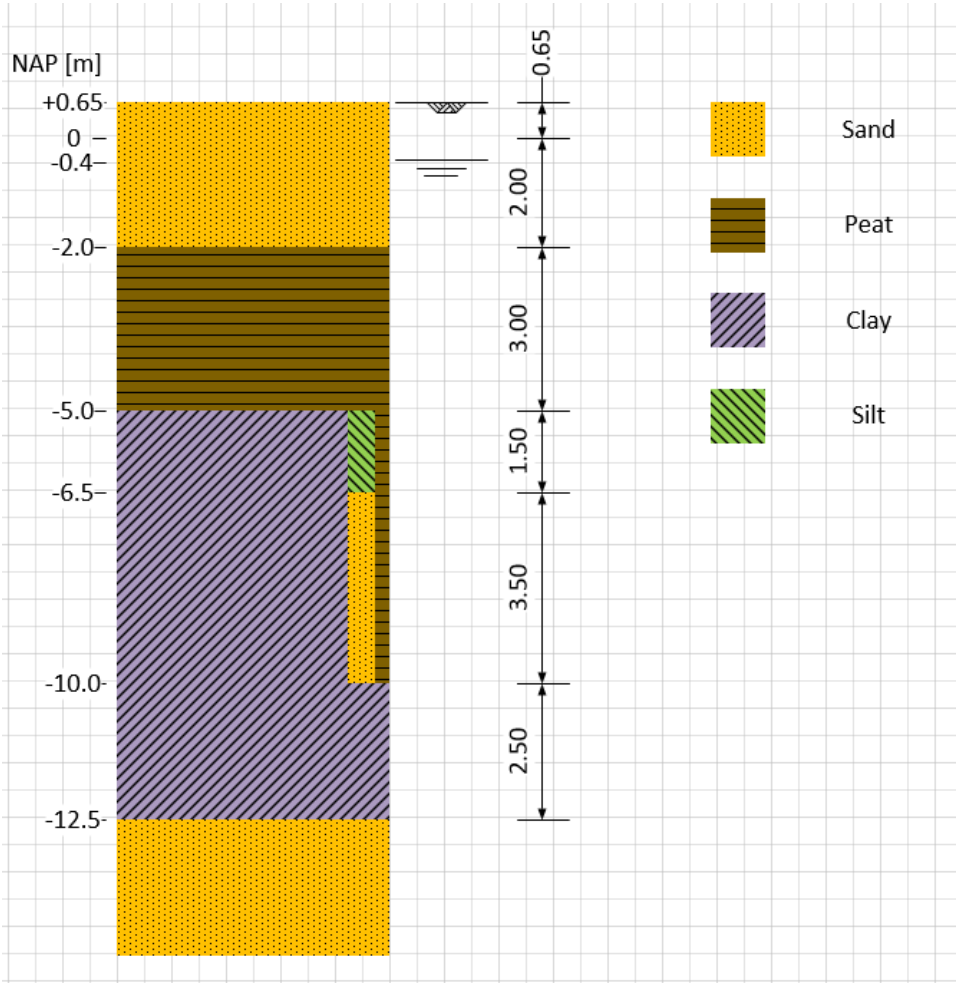

Figure 4.2: Schematisation soil profile Herengracht

Layer	Elevation layer top [m NAP]	Elevation layer bottom [m NAP]
1. Anthropogenic sand	+0.65	-2.00
2. Holland peat	-2.00	-5.00
3. Mudflat deposition - clayey	-5.00	-6.50
4. Mudflat deposition - sandy	-6.50	-10.0
5. Hydrobia clay	-10.0	-12.5
6. First sand layer	-12.5	N.A.

Table 4.2: Soil profile Herengracht, Natural Surface Level at +0.65 m NAP

The following table gives an overview of soil parameters obtained which are to be used for the HSsmall soil models.

Layer	**1**	**2**	**3**	**4**	**5**	**6**	
Parameter							**Unit**
γ_n	19.0	10.5	16.9	17.9	15.5	17.7	kN/m^3
γ_{dry}	15.2	2.69	11.7	13.2	9.30	14.7	kN/m^3
γ_{sat}	19.4	11.0	17.2	18.1	15.5	18.9	kN/m^3
e_0	0.740	6.60	1.27	0.980	1.72	0.774	–
φ'	32.5	14.9	28.8	25.0	23.6	35.0	°
c'	0.00	6.20	3.65	2.17	10.9	0.00	kPa
ψ	2.50	0.00	0.00	0.00	0.00	5.00	°
ν_{ur}	0.15	0.15	0.15	0.20	0.15	0.20	–
m	0.5	0.9	0.8	0.7	0.8	0.5	–
E_{50}^{ref}	20.0	2.32	16.5	12.6	7.40	40.0	MPa
E_{oed}^{ref}	21.1	2.36	17.4	14.0	7.81	44.4	MPa
E_{ur}^{ref}	60.0	6.70	49.5	37.9	22.2	120.	MPa
G_0	26.1	2.91	21.5	15.8	9.65	50.0	MPa
$\gamma_{0.7}$	5.65E-4	4.19E-3	7.20E-4	9.01E-4	1.77E-3	2.98E-4	–

Table 4.3: HSsmall properties per layer, with reference pressure p_{ref} = 100 kPa, with layers defined as:
1: Anthropogenic sand
2: Holland peat
3: Mudflat deposition - clayey
4: Mudflat deposition - sandy
5: Hydrobia clay
6: 1st sand layer

4.1.3. Wood parameters

This section provides an overview of the timber properties determined. For the full derivation, see Appendix D, Page 115. The following properties have been used:

Parameter	**Value**	**Unit**
γ	2.71	kN/m^3
$f_{m,k}$	27	MPa
$f_{t,0,k}$	16	MPa
$f_{c,0,k}$	22	MPa
E_B	11 864	MPa
Wood type	European Spruce (*Picae abies*)	–

Table 4.4: Timber properties

4.1.4. Pile resistance parameters

In the Embedded Beam Row model, the lateral, axial and tip resistance of the pile is part of the user input. These resistances can differ per pile, based on the soil profile. The lateral resistance has been determined as proposed by Brinch-Hansen (1961). The axial and tip resistance have been determined using the method Koppejan. For the determination, see Appendix E, Page 118.

4.2. Plaxis 2D calculations Herengracht case

This section provides a summary of the Plaxis model used. For a full overview, see Appendix F, Page 121.

The quay wall has been modelled as depicted in Figures 4.3 and 4.4.

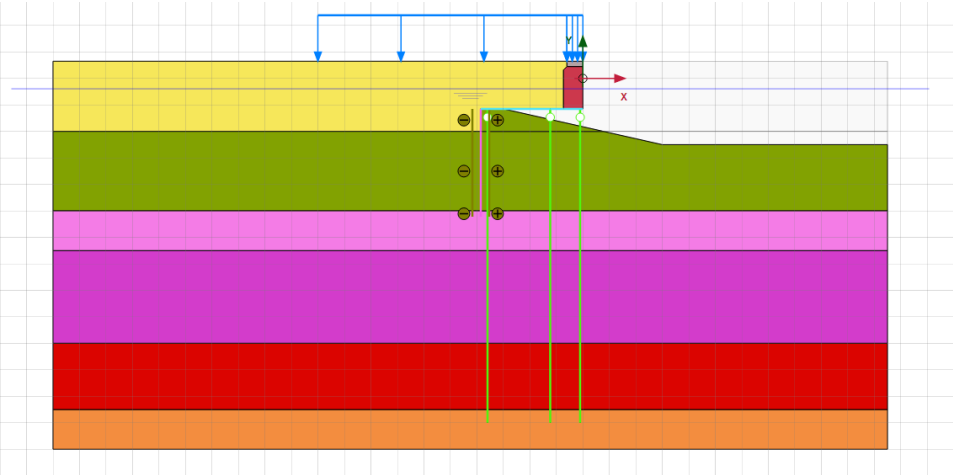

Figure 4.3: Geometry Plaxis model Herengracht case

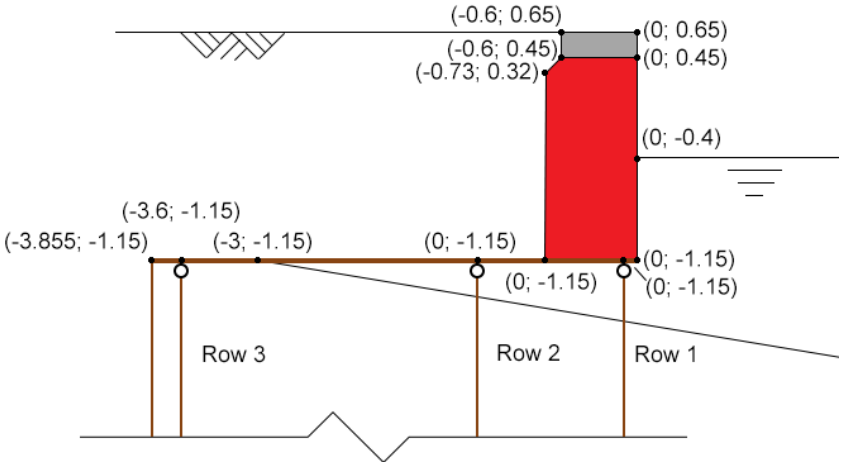

Figure 4.4: Geometry Plaxis model Herengracht case, schematised

The phases used in the model have been listed in Table 4.5. The model starts with a homogeneous soil in which a K0-procedure is executed. In the following phase 1, the quay wall is installed in phase. The exact installation method is not relevant, as the quay wall modelled is not a replica of an existing one. In phase 2, the load is applied on the structure, this phase would represent t = 0. Phase 3 runs parallel to phase 2 and uses the results from phase 1. In phase 3, the load is activated and the maximum creep factor is applied on the structure. These results will serve as a check. Phases 4 and onward use the results from phase 2. In these phases, the stiffness is incrementally reduced to simulate the creep. It has been assumed creep deformations occur slow enough to be modelled using drained loading conditions.

Phase number	Start from phase	Description
0	N.A.	Initial phase, soil profile homogeneous in horizontal plane, stress generation via K0 procedure
1	0	Moment just after finishing construction quay wall, t=0
2	1	Applying load on the quay wall directly after finishing construction, using parameters from t=0
3	1	Applying load on the quay wall directly after finishing construction, using parameters from t=∞
4+	2	Calculating deformation at different points in time, using parameters 0<t=∞

Table 4.5: Plaxis 2D phases Herengracht model

For the first case, a load of 10 kN/m^2 has been applied from the side of the quay wall up to 10 m away. At this point, housing starts, which is supported by pile foundation. Hence, it has been assumed the housing does not exert a load on the greenfield.

4.3. D-Sheet Pile calculations Herengracht quay wall

A validation of the behaviour of the Embedded Beam Row for the Herengracht case has been performed. In here, it can be seen how the front pile row of the quay wall has been modelled as a single laterally loaded pile. The soil profile is constant in the horizontal plane, in order to ensure the pile is solely being loaded by the horizontal force at the top. For comparison, a single pile has been modelled using the Single Pile module in D-Sheet Piling. An image of the model is seen in Figure 4.5. Note, elevations in D-Sheet Piling are in reference to pile head, whereas in the Plaxis model it is to NAP. In D-Sheet, the ultimate resistance is calculated in the centre of each layer, and then used over the whole depth of that layer. This can lead to inaccurate results. Hence, a mesh refinement has been carried out. The layers have been reduced in thickness until there was a negligible change in displacement of the head of the pile.

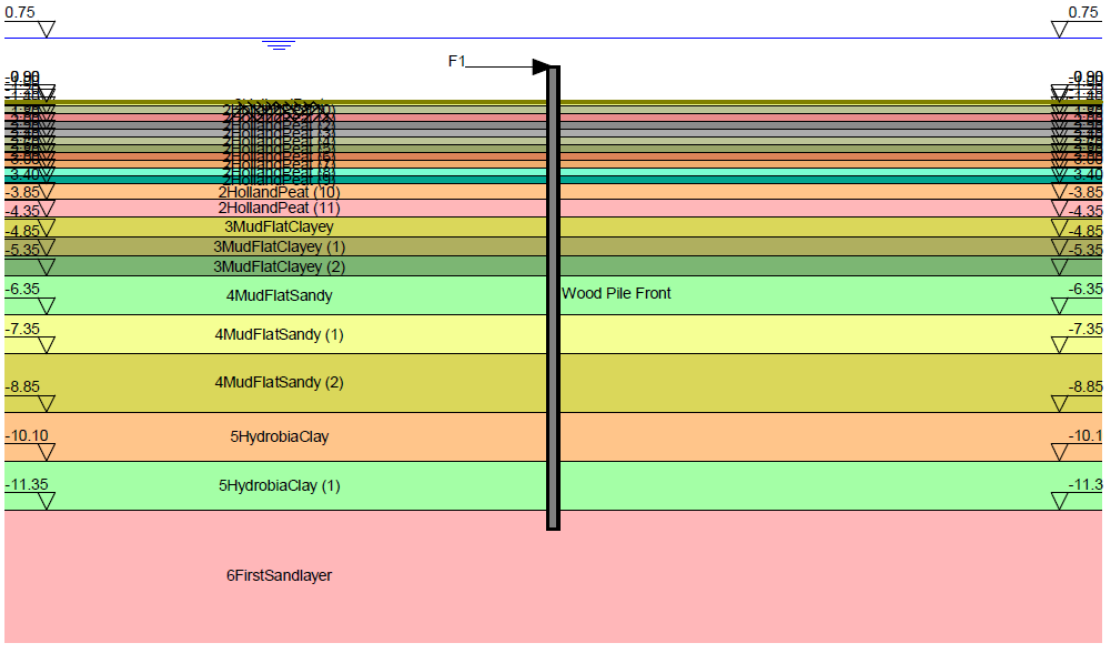

Figure 4.5: D-Sheet Piling model single pile Herengracht case

The horizontal subgrade modulus of the soil has been determined using the Ménard method:

$$\frac{1}{K_H} = \frac{D}{E_{Ménard}} \frac{4.0(2.65)^{\alpha} + 3\alpha}{18} \; (D < 0.60\ m)$$
$$E_{Ménard} = f * q_c \tag{4.1}$$

With:

- K_H: horizontal modulus of subgrade reaction for piles [kN/m]
- D: pile diameter [m]
- $E_{Ménard}$: radial elasticity modulus, or Ménard stiffness [kPa]
- α: empirical factor as defined in Table 4.6 [-]
- q_c: cone resistance [kPa]
- f: empirical factor as defined in Table 4.6 [-]

Soil type	**f**	α
Gravel	N.A.	1/4
Sand	0.8 to 1.0	1/3
Silt	2.0 to 3.0	1/2
Clay	3.0	2/3
Peat	3.0 to 4.0	1.0

Table 4.6: Empirical factors horizontal subgrade modulus

The parameters in Table 4.7 have been used in the D-Sheet Piling model. Furthermore, a second run has been done where the $E_{Ménard}$ values had been halved, in order to check the sensitivity of the results relating to the stiffness.

Layer	**2**	**3**	**4**	**5**	**6**	
Parameter						**Unit**
γ_{unsat}	10.5	16.9	17.9	15.5	17.7	kN/m^3
γ_{sat}	11.0	17.2	18.1	15.5	18.9	kN/m^3
φ'	14.9	28.8	25.0	23.6	35.0	°
c'	6.20	3.65	2.17	10.9	0.00	kPa
q_c	400	1000	1400	600	7000	kPa
f	3.5	3	3	3	0.8	–
α	1	2/3	2/3	2/3	1/3	–

Table 4.7: D-Sheet Piling input per layer, with layers defined as:
2: Holland peat
3: Mudflat deposition - clayey
4: Mudflat deposition - sandy
5: Hydrobia clay
6: 1st sand layer

The results are presented in Figures 4.6 through 4.8. In Plaxis, no stability had been found beyond the final load.

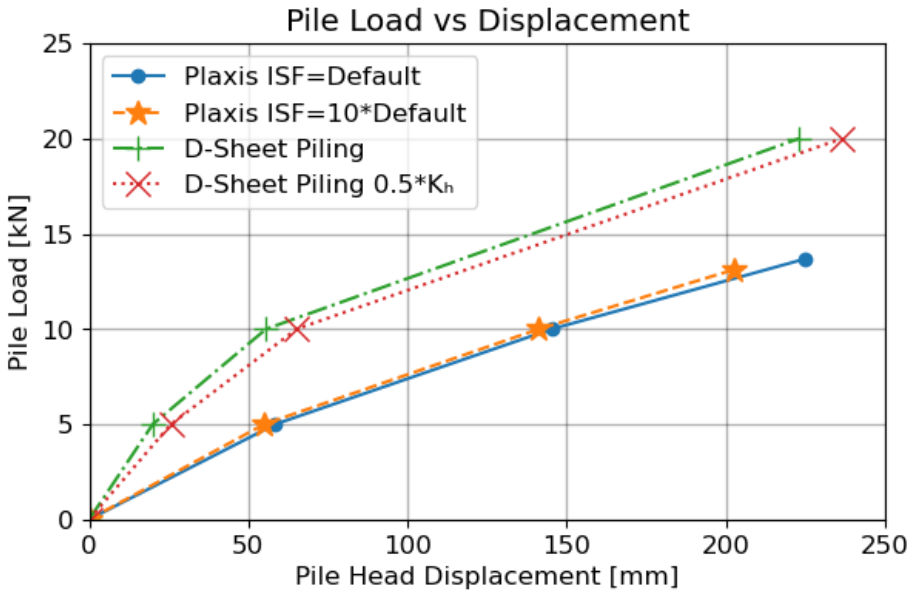

Figure 4.6: Load-displacement curve single pile (D-Sheet Piling) and single pile row (Plaxis) Herengracht case

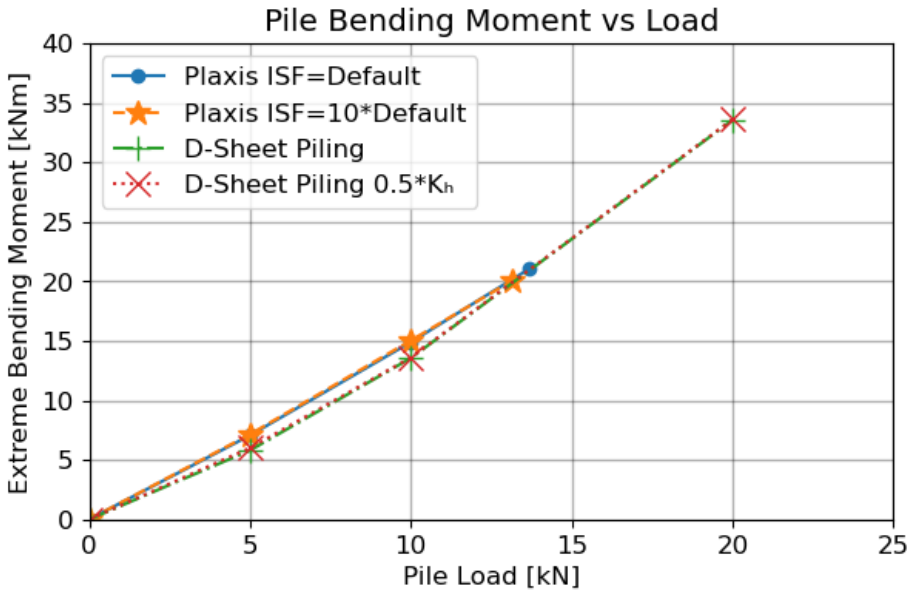

Figure 4.7: Moment-load curve single pile (D-Sheet Piling) and single pile row (Plaxis) Herengracht case

In Figure 4.6 it can be observed the response of the Plaxis model is less stiff compared to D-Sheet Piling. This is as had been expected, as D-Sheet Piling does not incorporate group effects, which would results in less stiff behaviour. Decreasing the $E_{Ménard}$ by halve only increased displacements with approximately 6%. Figure 4.7 shows that for a given loading, the maximum occurring bending moment in the Plaxis model is near identical to those obtained using D-Sheet Piling. The graph for D-Sheet Piling extends beyond the one from Plaxis, as failure occurred in the latter. Halving the soil stiffness in the D-Sheet model caused a negligible increase in maximum bending moment.

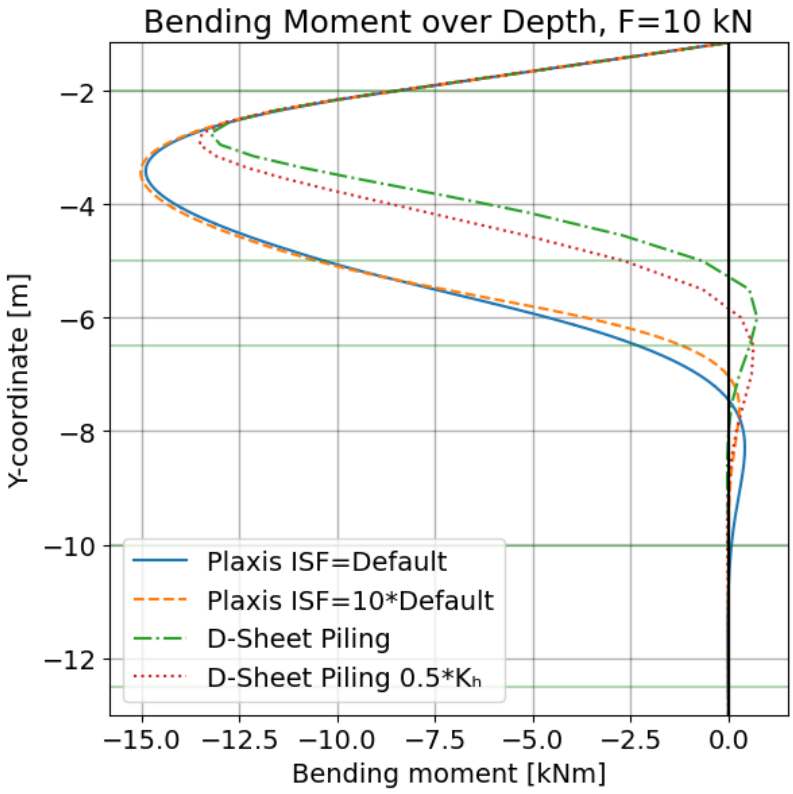

Figure 4.8: Bending moment over depth single pile Herengracht, F = 10 kN

Figure 4.8 shows that the extreme bending moments occur at larger depths in the Plaxis model compared to the D-Sheet Piling one. This suggests that the top layers in D-Sheet Piling provide a stiffer response. A possible explanation for this is the difference in soil model. Where D-Sheet Piling uses a linear-elastic perfect-plastic model, Plaxis uses the non-linear Hardening Soil model. When halving the soil stiffness in D-Sheet, the moment distribution slightly approaches the one calculated using Plaxis 2D.

From the comparison to D-Sheet Piling, it has been concluded the Plaxis model provides realistic results. The force-displacement behaviour of the Plaxis model is less stiff, which is to be expected since group effects take place. Some difference was found between the bending moment distribution over depth. Nevertheless, it seems that the Plaxis results are realistic. However, comparison between the two software packages remains difficult, as different soil models are being used.

5

Results Timber Creep Herengracht case Plaxis

For the reference case, the quay wall has been simulated for the cases φ = 0.0 and φ = 1.6. The results are presented below. The pile rows have been labelled 1 through 3, with row 1 nearest to the water and row 3 the furthest away. First, the results at the beginning and end of creep curve will be analysed, in Sections 5.1. From Section 5.2, Page 42, the behaviour over time will be discussed.

5.1. Results creep behaviour using one (Direct) or multiple (Indirect) steps Herengracht case

This section will discuss the behaviour of the quay wall prior and after the creep process. The results obtained from the different modelling methods will be compared. These included the Direct method, in which the final creep factor of 1.6 had been applied in the same step the surface load has been applied, and the Indirect one. in which the creep reduction is applied in steps of 0.1.

5.1.1. Horizontal displacements quay wall before and after creep Plaxis 2D Herengracht case

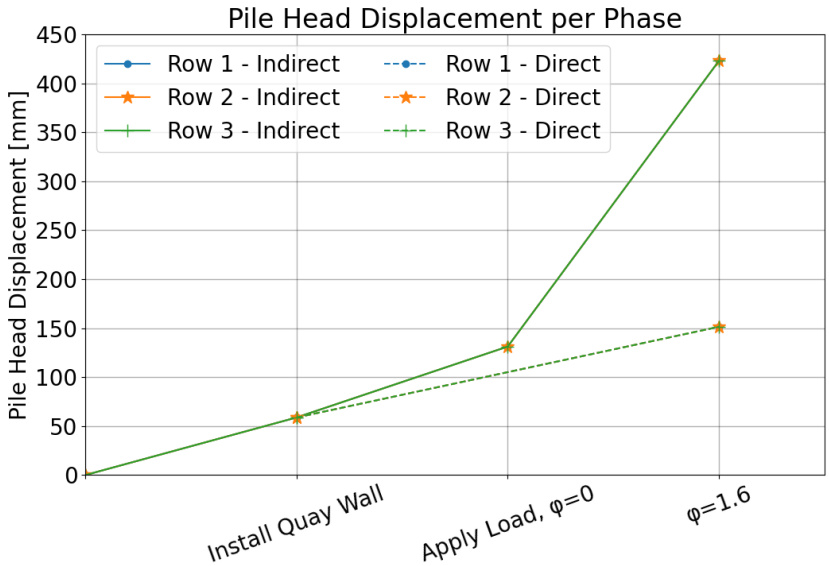

Figure 5.1: Displacement individual pile rows in the phases prior and after creep, per pile row, from Plaxis 2D Herengracht model

In Figure 5.1, on the previous page, the "Indirect" graphs show the behaviour of a pile when the load application and stiffness-reduction are performed in different phases. The "Direct" graphs show the behaviour obtained when using one phase for modelling creep. Figure 5.1 shows that with the M-κ reduction based on φ = 1.6, the displacements increase. Furthermore, it can be observed that by first applying the load in one phase and reducing the stiffness in the following, yields different results than applying everything at once. For all piles, the displacements calculated using one direct step are lower than when using multiple stages. For both Direct and Indirect phasing, there is a negligible difference in head displacement between the rows. Compared to the phase in which the quay wall is installed, the Indirect phasing resulted in a relative horizontal displacement of 364 mm. The Direct phasing predicted a relative horizontal displacement of 93 mm, 75% less compared to the Indirect phasing. This suggests different stress paths occur, depending on how the creep is modelled.

5.1.2. Maximum compressive stresses and forces before and after creep Herengracht case

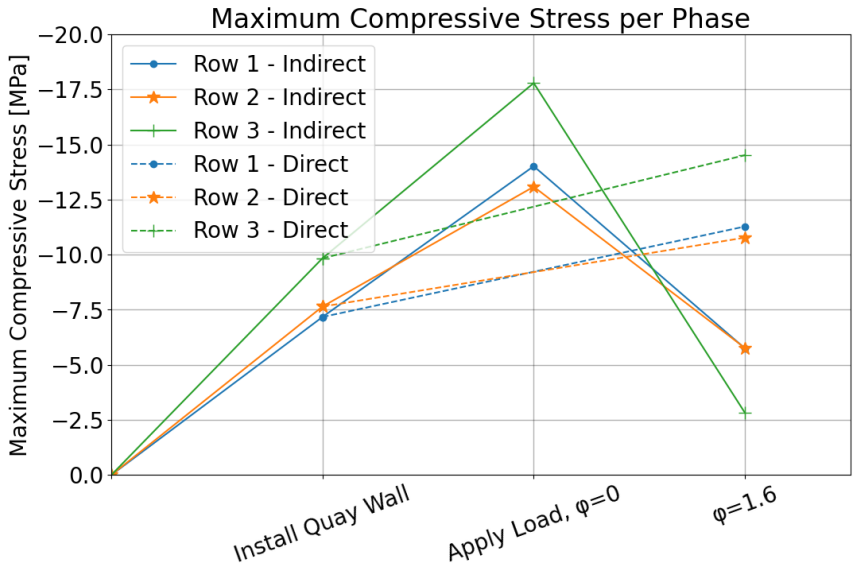

Figure 5.2: Maximum compressive stress in the phases prior and after creep, per pile row, from Plaxis 2D Herengracht model

In Figure 5.2, the "Indirect" graphs show the behaviour of a pile when the load application and stiffness-reduction are performed in different phases. The "Direct" graphs show the behaviour of the piles when the load application and reduction are applied in the same phase. When using multiple phases, the Indirect graphs, the compressive stress decreases when applying the stiffness reduction. Prior to the reduction, the highest stress occurred in row 3. However, after the stiffness-reduction, the stress in row 3 has decreased the most of all rows, ending up with the lowest stress. In the Direct phasing, the stresses in row 1 and 2 decrease slightly, wheres in row 2 they increase with a certain significance. For all pile rows, the Direct method resulted in larger final stresses than the Indirect method. The Indirect method predicted 49% lower stresses in pile row 1 and up to 81% for pile row 3, compared to the Direct method. The stresses in the final step of the Direct method, after all creep deformation, are lower than the initial stresses in the Indirect method in the phase the load had been applied.

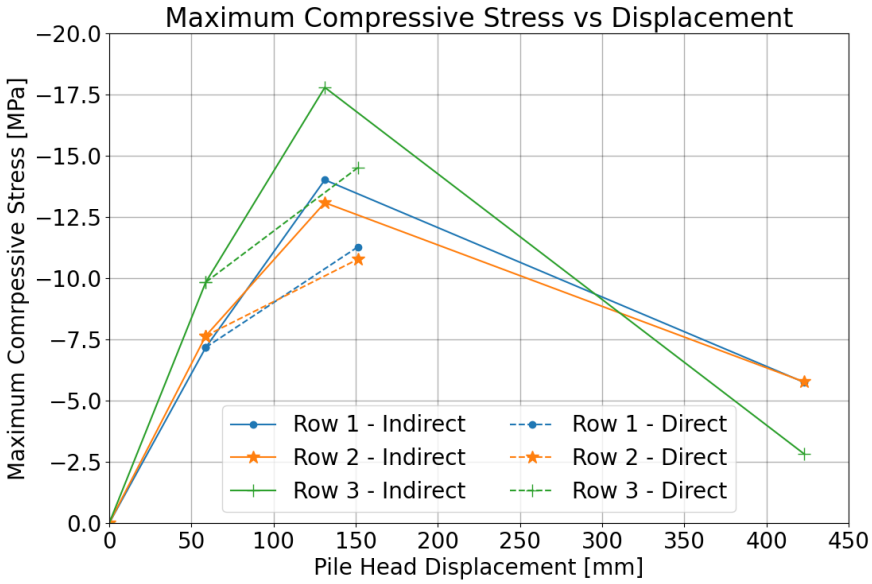

Figure 5.3: Maximum compressive stress vs displacement individual, per pile row, from Plaxis 2D Herengracht model

Figure 5.3 shows a combination of Figures 5.1 and 5.2. The figure shows the results are dependent on how the creep is introduced. In the Direct phasing, more stress remains present within the piles. Furthermore, the displacements are smaller. For the Indirect phasing, the stress has dropped significantly after the creep has been applied, accompanied by large displacements.

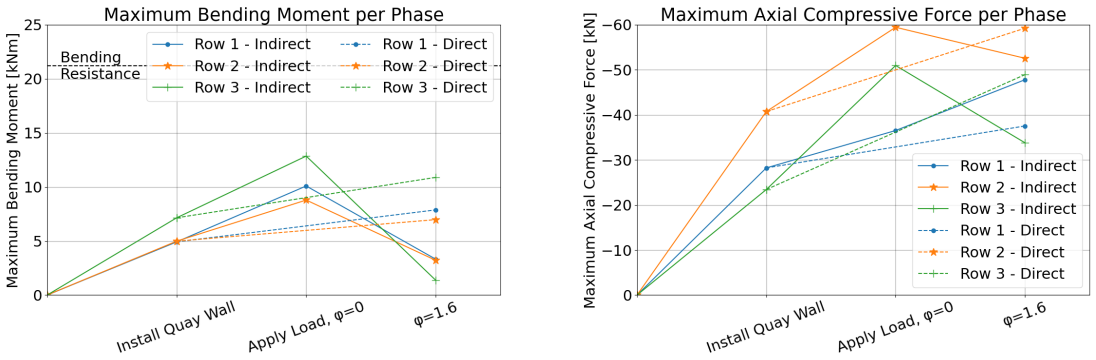

(a) Maximum bending moments in the phases prior and after creep, per pile row, from Plaxis 2D Herengracht model

(b) Maximum axial compressive force in the phases prior and after creep, per pile row, from Plaxis 2D Herengracht model

Figure 5.4a shows the maximum bending moments before and after the creep process. It can be observed that for all pile rows in the Indirect phasing, the maximum bending moment has decreased after the creep has taken place. Furthermore, all maximum bending moments in the final step of the Direct phasing are lower than those in the step "Apply Load, φ=0" of the Indirect phasing. As had been expected from Figure 5.2, the maximum bending moments have decreased during the creep process. Figure 5.4b shows the maximum axial compressive force before and after the creep process. For the Direct phasing, all axial forces increased due to the creep. For the Indirect phasing, all pile rows show different behaviour. The front row, row 1, shows an increase in axial force after the creep phase. The centre row, row 2, shows a little change in the axial force. The last row, row 3, shows a decrease in axial force. The increase in axial force on the front-side and decrease at the back suggests the quay-wall was overturning during the creep process. In the results of the final creep step, it had been found that the vertical displacement of pile row 3 was 20 mm less compared to pile rows 1 and 2, seemingly confirming the statement concerning overturning.

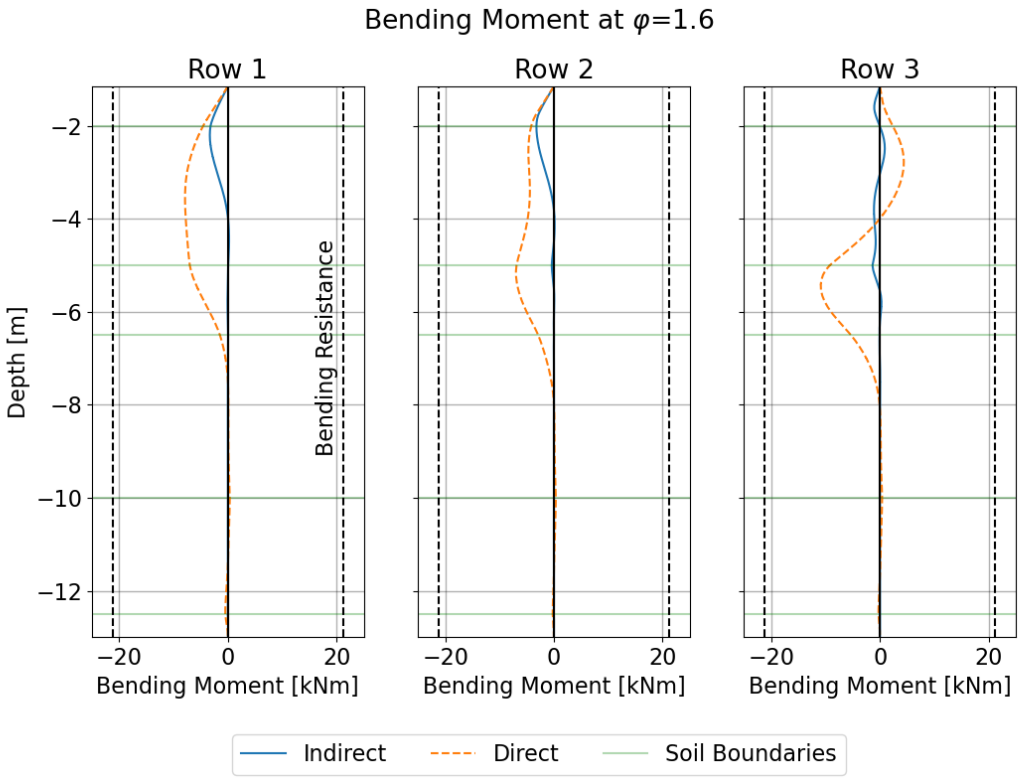

Figure 5.5: Bending moment per pile over depth Plaxis 2D Herengracht model, φ = 1.6

Figure 5.5 shows that Direct and Indirect phasing result in different moment distributions after creep. The maximum bending moment in the Direct phasing is in all rows larger than in the Indirect one. For each pile row, the shape of the graph differs. Furthermore, the depth of the extreme bending moments vary. The bending moments in the Direct phasing reach zero at a larger depth; for row 1, the bending moments in the Indirect phasing go to zero at a depth of -5 m, whereas for the Direct phasing this takes place from -8 m and deeper. Subsequently, the surface area enclosed by the graphs shows that in the Indirect phasing, the pile rows carry less load. The larger the area under the graph, the more potential energy has been stored in the beam in the form of bending energy, as stated in Equation 5.1. The surface of the Indirect phasing is significantly smaller in contrast to the Direct phasing, meaning it has less potential energy stored.

$$\begin{aligned} E_{pot,bending} &= \int_0^L \frac{1}{2}\kappa^2 EI dx \\ &= \int_0^L \frac{1}{2}\left(\frac{M(x)}{EI}\right)^2 EI dx \\ &= \int_0^L \frac{1}{2}\frac{(M(x))^2}{EI} dx \end{aligned} \tag{5.1}$$

5.1.3. Lateral traction after creep Herengracht case

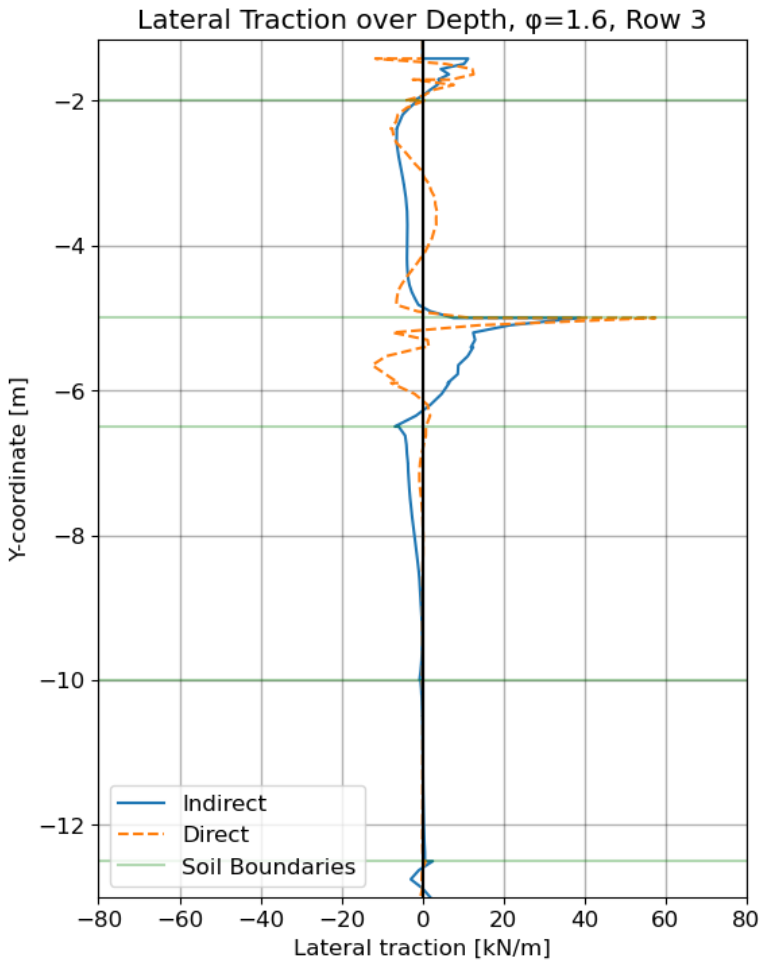

Figure 5.6: Embedded Beam Row Interface lateral traction over depth per pile from Plaxis 2D Herengracht model, row 3, $\varphi = 1.6$

Figure 5.6 shows the lateral traction over depth in the final step for pile row 3. It can be observed that the graphs for Indirect and Direct are again dissimilar. The shape of the graphs deviate as well as the area enclosed. One thing the graphs do have in common is the peak at the soil boundary at -5 m. Besides that, it can be observed that the Direct and Indirect phasing result in a different response of the quay wall.

5.2. Results creep behaviour over time Herengracht case

As stated earlier, the previous sections concerned the quay wall behaviour before and after creep. This section will discuss the behaviour of the quay wall for varying creep factors, which represents the behaviour of the quay wall at different moments in time. However, it is unknown which amount of real time each moment represents. Furthermore, it is possible the time between these moments differ; for example, the time between φ=0.2 and φ=0.3 might be double of the time between the moments of φ=0.1 and φ=0.2. It is possible to use a creep law to relate the creep factors to moments in time. However, no creep law has been deemed applicable to model this case.

5.2.1. Horizontal displacement quay wall over time Herengracht case

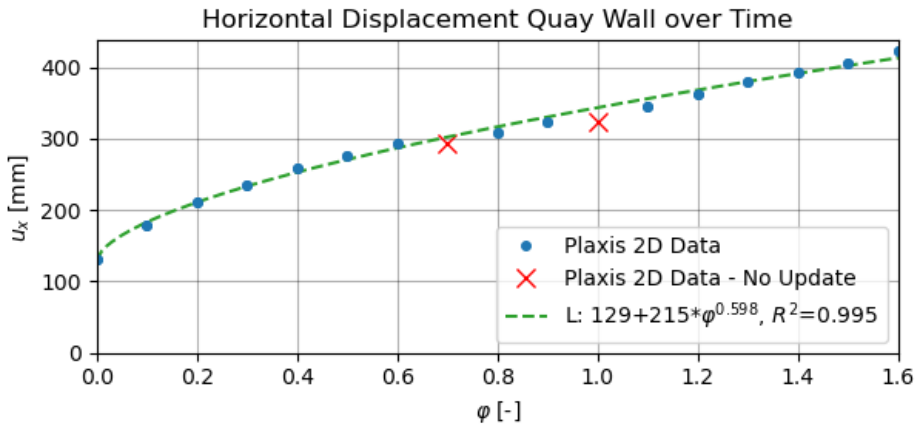

Figure 5.7: Horizontal displacement of the quay wall over time, Herengracht case

Figure 5.7 shows the horizontal displacement of the quay wall over time. The largest increment for displacement occurs in the first creep step. After this first step, the displacement rate decreases with each creep factor increment. As discussed during the literature study, a power law has often been applied to describe timber creep. A power law as presented in Equation 2.12, Page 13 has been used to perform a curve-fit, shown by the green dashed line. As can be seen in the figure itself, the curve and the data align well. Furthermore, the R-squared value of 0.995 suggests the power law provides a decent fit. The data, as well as the power law curve-fit, take on the shape of the primary and secondary creep stages as presented in the general creep curve in Figure 2.7, Page 9.

Figure 5.7 also shows two red crosses at φ=0.7 and 1.0. These points show an identical horizontal displacement compared to the steps prior to them. In these phases, no new displacements had been calculated by Plaxis. In these phases, the reduction in strength in the Embedded Beam Rows did not cause a sufficiently large error to trigger calculations. For this reason, these two points have not been included in the curve-fit. It is possible this error could have been prevented by decreasing the stepsize used to create the moment-curvature diagram, as has been explained in Section 2.8, Page 11. However, smaller steps could not be achieved. This is due to Plaxis checking if the slope of the moment-curvature increases, which it does not allow. By decreasing step sizes, floating point arithmetic error occurred, in which the slope is rounded upward due to the bitsize used for storing the values. With the slope being rounded up, Plaxis did not allow for the moment-curvature to be entered.

5.2.2. Maximum compressive stresses and forces over time Herengracht case

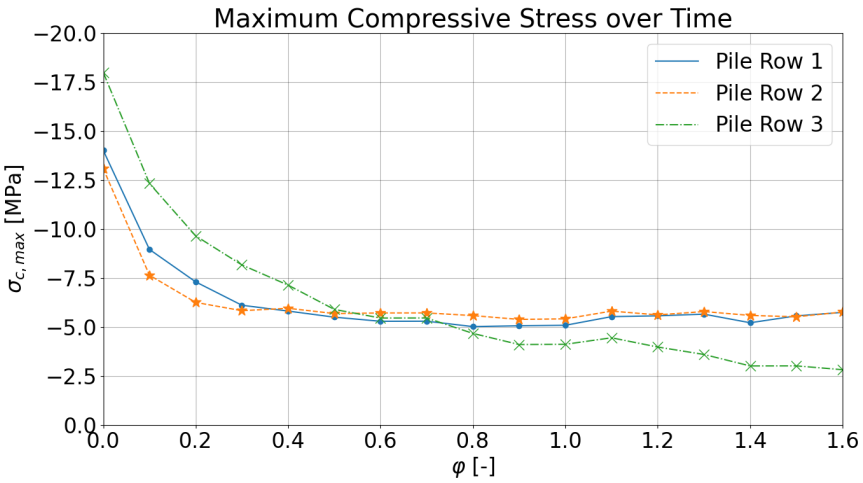

Figure 5.8: Maximum compressive stress per pile row over time, Herengracht case

Figure 5.8 shows how the maximum compressive stress in all pile rows decreases rapidly. However, for pile rows 1 and 2, the stress seems to stabilise around φ=0.4. For pile row 3 however, the one located at the back near the retaining screen, keeps on decreasing in stress. Furthermore, it initially started with a higher compressive stress but eventually ends up with a lower one compared to the other two pile rows.

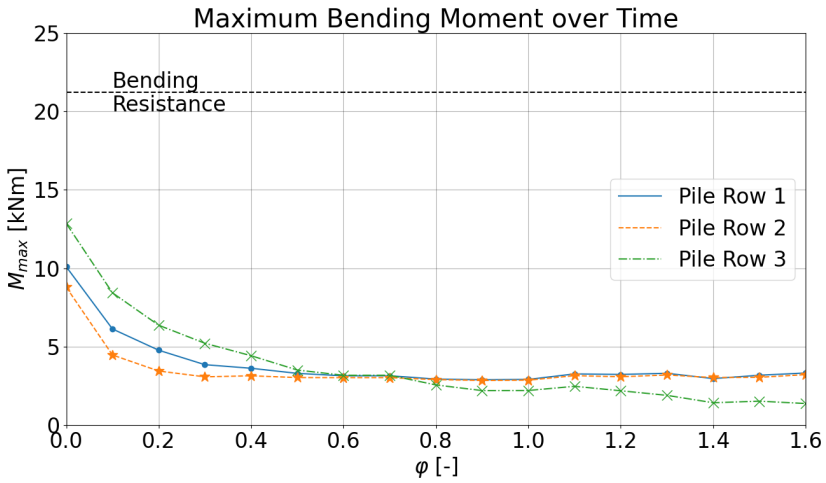

Figure 5.9: Maximum bending moment per pile row over time, Herengracht case

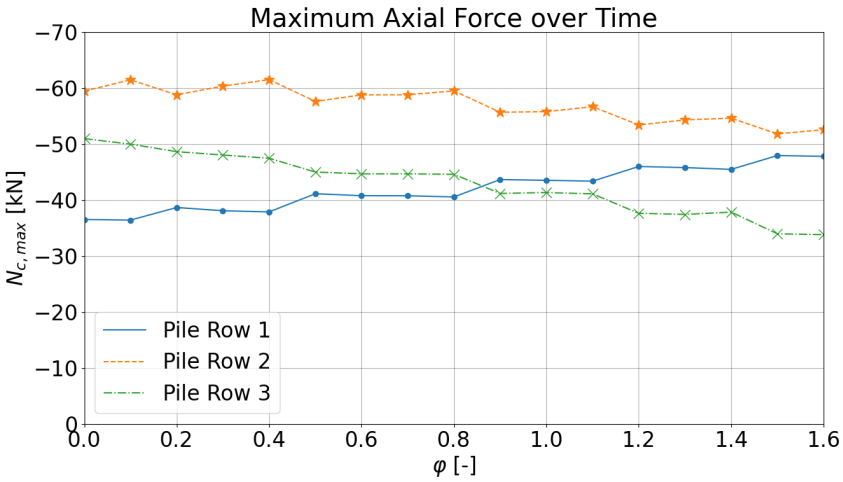

Figure 5.10: Maximum compressive axial force per pile row over time, Herengracht case

Figures 5.9 and 5.10 show the maximum bending moment and compressive axial force per pile row over time. In Figure 5.9, similar behaviour can be seen as has been observed in Figure 5.8. For all pile rows, the maximum bending moment decreases rapidly up to φ=0.4. For pile row 1 and 2, the maximum moment remains stable for following creep factors. For pile row 3, the maximum bending moment keeps reducing. It is possible that the different pile behaviour of row 3 is caused by influence of the nearby retaining screen. In Figure 5.10, it can be seen that the axial forces in rows 2 and 3 decreases over time. For pile row 1, the maximum axial force has increased after the creep process, but also show sudden jumps instead of a continuous increase. The increase in axial force in the front pile row is likely caused due to an overturning caused by the soil the quay wall is retaining. Comparing these figures with the stress-time curves in Figure 5.8, it seems that the maximum compressive stress is dominated by the bending moment, as the shape of stress curve is nearly identical to the one of the moment curve.

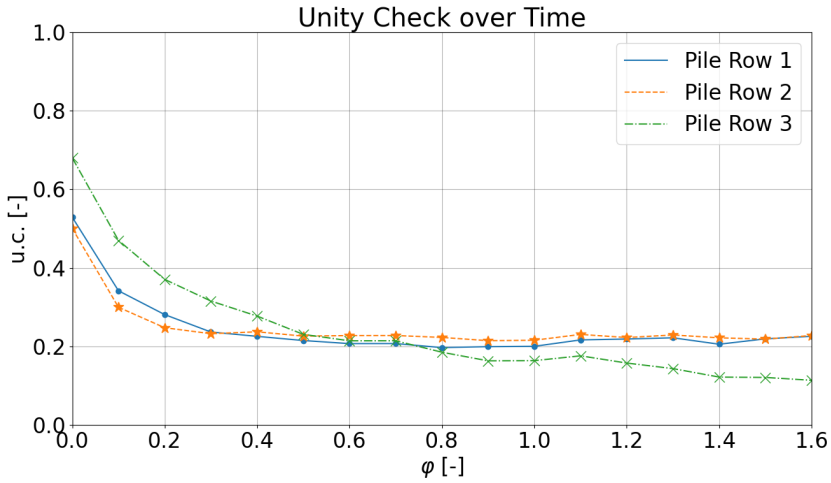

Figure 5.11: Unity check per pile row over time, Herengracht case

The combined unity check of bending and axial compression has been plotted in Figure 5.11. In here it can be seen that the unity check decreases for increasing creep factor, meaning the piles carry less load. This result would suggest relaxation behaviour occurs in the piles. The figure shows how the safety against structural failure of the piles due to compression goes up, for increasing creep factor.

5.2.3. Bending moment over depth over time Herengracht case

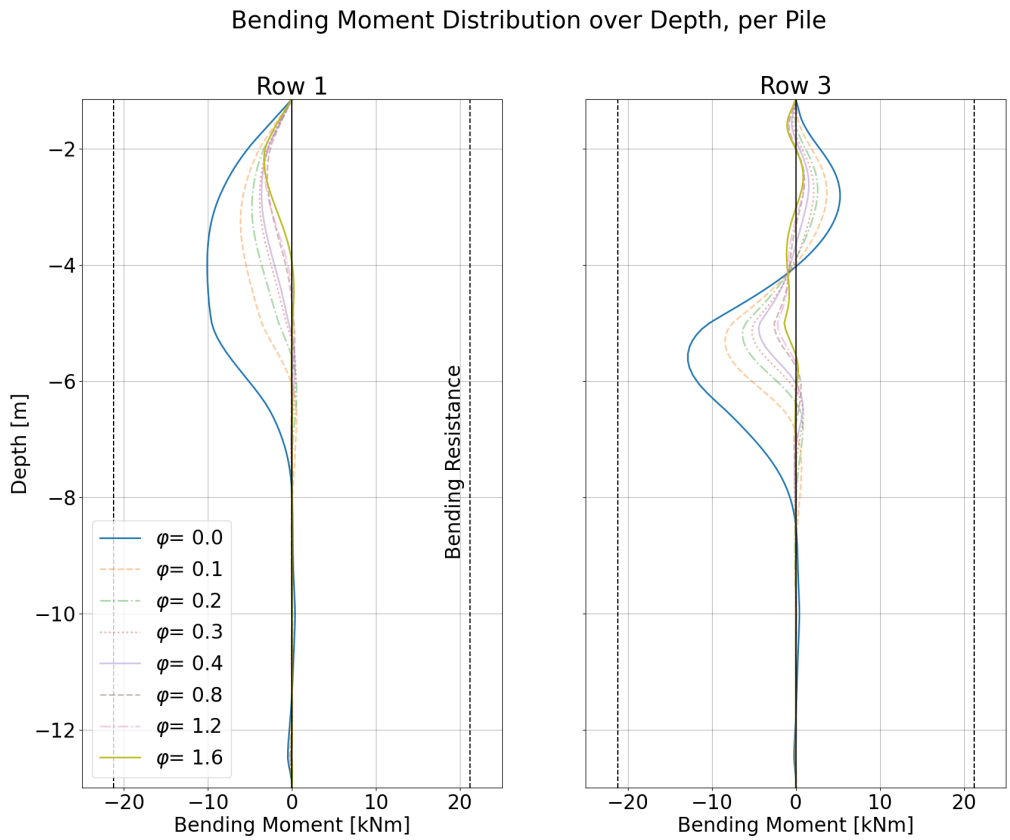

Figure 5.12: Bending moment distribution per pile over time for rows 1 and 3, Herengracht case

Figure 5.12 shows the bending moment distributions over time for pile rows 1 and 3. Pile row 2 showed a shape similar to the one from pile row 1 For both pile rows, it can be seen that the peak in bending moment decreases for increasing creep factors. Furthermore, the area enclosed by the moment-curve decreases over time. As discussed earlier, the area of the moment-curve can directly be related to the internal energy stored due to bending. Thus, the moment distribution over time reinforces the statement that the piles carry less as the creep factor increases.

As already discussed in Section 2.9, it might sound possible for bending moment, and thus stress, to reduce as a result of reduced bending stiffness. In Figures 2.11, Page 15, it can be seen how a reduction of relative pile flexibility ratio by a factor 1000 causes a reduction in moment of approximately 60 to 70%, depending on soil homogeneity. In this case study, a maximum bending stiffness reduction factor of 2.6 has been applied, which results in a similar reduction factor for the relative pile flexibility ratio. In this case however, a decrease in bending moment of 70 up to 90% has been calculated, depending on the pile row. With a factor 400 difference in relative pile flexibility ratio reduction but given the same maximum bending moment decrease, it is unlikely the results are just a result of bending stiffness reduction, and more likely to be caused by the timber creep.

5.2.4. Lateral traction over time Herengracht case

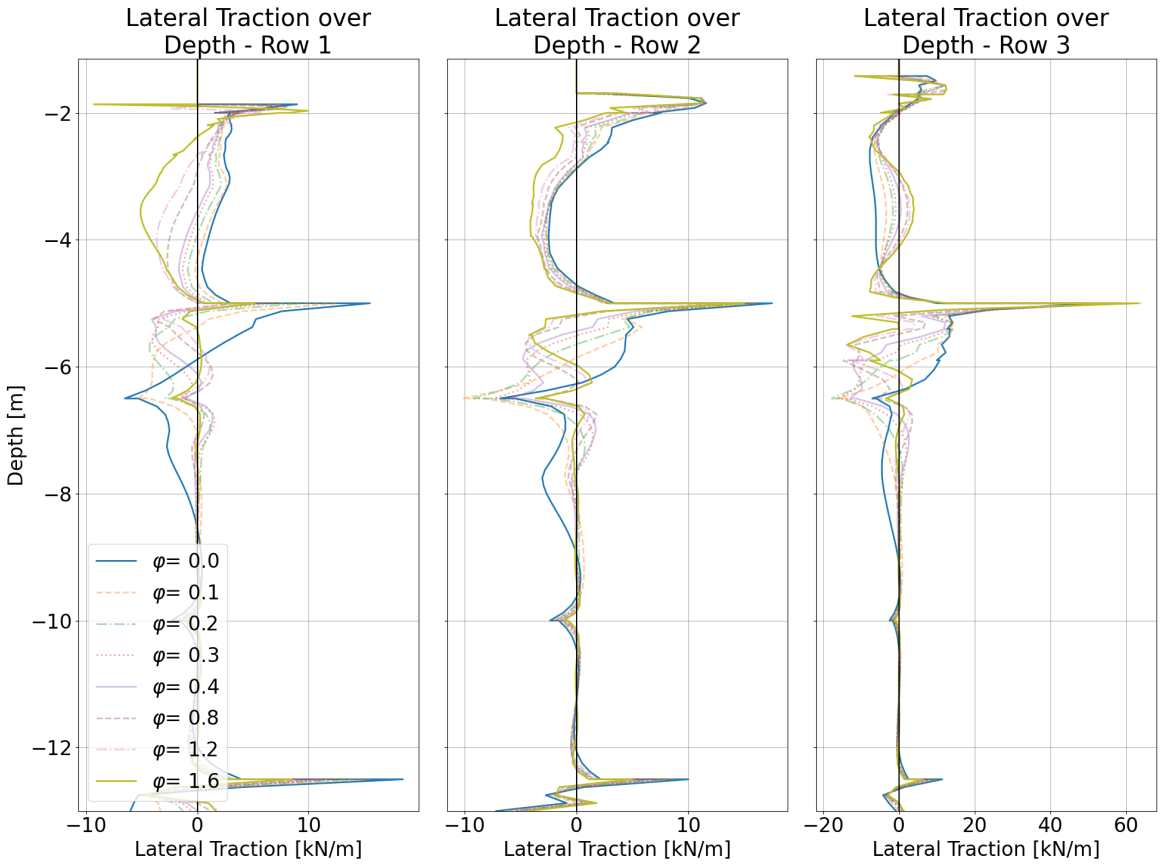

Figure 5.13: Lateral traction per pile over depth over time per row, Herengracht case

Figure 5.13 shows the lateral traction over depth per pile row for several creep factors. The most noticeable aspect of the curves present in this figure are the peaks occurring at certain depths. Independent of the creep factor, the location of these peaks are near constant. As mentioned before, these peaks coincide with soil boundary layers. For pile row 1, the lateral traction changes significantly over time. In the Holland Peat layer, between -2 and -5 m, the traction decreases over time until it flips sign. In the Clayey Mudflat Deposition between -5 and -6.5 m, the lateral traction begins relatively high compared to other depths but ends up near-zero in the final step. For Rows 2 and 3, the traction varies less over time. In both rows, the traction flips sign in a section in the Holland Peat layer, but not over the whole layer. This would indicate a transferal of load.

5.2.5. Force distribution retaining screen over time Herengracht case

From the moment distributions studied in Figure 5.12 it had been concluded that the piles carry less load for increasing creep factors. It had been suspected that more direct load transfer to the subgrade took place. This would result in an increase in soil pressure on the retaining screen. Hence, the moment and shear force distribution of the retaining screen at $\varphi = 0.0$ and $\varphi = 1.6$ have been plotted in Figure 5.14 for comparison. Furthermore, the net horizontal soil pressure acting on the retaining screen has been obtained by taking the derivative of the shear force.

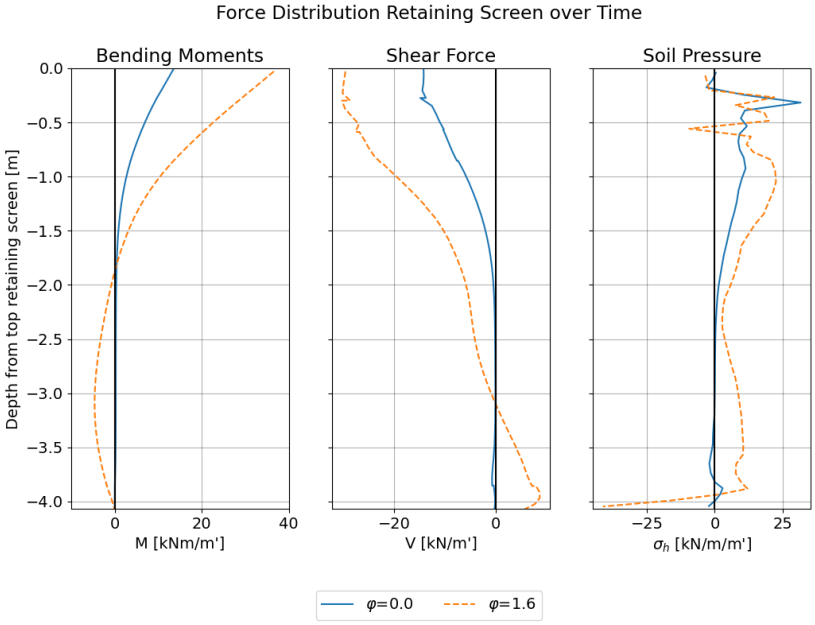

Figure 5.14: Force distribution retaining screen for $\varphi = 0.0$ and $\varphi = 1.6$, Herengracht case. Positive soil pressure means the soil is pushing towards the right, in the direction of the water

In Figure 5.14 it can be seen that the bending moments in the retaining screen are larger in the last step compared to the first step. This suggests more potential energy is stored with a higher creep factor, meaning that the screen carries more load in the final stage. Furthermore, the horizontal soil pressures acting on the screen are larger at $\varphi = 1.6$ than at $\varphi = 0.0$. This indicates that more of the surface load is transferred directly more to the subsoil instead of horizontally to the brick wall. As a result, the retaining screen has to carry more load as timber creep progresses.

5.3. Mesh analysis Plaxis 2D Herengracht case

For the results obtained in the previous sections, an element distribution of 0.04 has been used, corresponding to the "Medium" mesh setting in Plaxis 2D. The lower the element distribution, the finer the mesh. The same calculations have been performed using a "Coarse" and "Fine" element distribution. The results are presented in Tables 5.1 and 5.2. As determined in the previous section, there is a negligible difference of horizontal displacements between each pile row head.

Element distribution	**Coarse (0.08)**	**Medium (0.06)**	**Fine (0.04)**
# of Elements	1013	1378	2486
# of Nodes	8602	11604	20624
u_x $[mm]$	451.0	446.9	461.5
$\sigma_{max,1}$ $[MPa]$	-6.980	-7.282	-7.396
$\sigma_{max,2}$ $[MPa]$	-6.332	-6.267	-6.646
$\sigma_{max,3}$ $[MPa]$	-3.175	-3.510	-3.291

Table 5.1: Horizontal displacements and maximum compressive stresses per row per mesh setting, $\varphi = 1.6$, for Indirect phasing

Element distribution	**Coarse (0.08)**	**Medium (0.06)**	**Fine (0.04)**
# of Elements	1013	1378	2486
# of Nodes	8602	11604	20624
u_x $[mm]$	155.8	156.0	156.2
$\sigma_{max,1}$ $[MPa]$	-11.40	-11.40	-11.44
$\sigma_{max,2}$ $[MPa]$	-10.70	-10.70	-10.55
$\sigma_{max,3}$ $[MPa]$	-14.54	-14.52	-14.41

Table 5.2: Horizontal displacements and maximum compressive stresses per row per mesh setting, $\varphi = 1.6$, for Direct phasing

Table 5.1 above shows that, for the Direct phasing, there is a negligible difference between the three different mesh settings. Displacements as well as stresses are withing 1% of the reference case. For the Indirect phasing however, Table 5.2 shows differences going up to roughly 10%. For a more detailed comparison, the stress and displacements path over time for each mesh setting has been plotted in Figure 5.15. In here, it can be observed that on a local scale, deviations are present between the paths, especially in the stress path for the third row. These deviations however only occur after two or more time steps have been taken. Prior to this moment, the graphs coincide. On a global scale, the paths align for the majority. This would suggest that the few local deviations that occur are not due to the mesh size. It is likely the deviations are due to small numerical errors due to the tolerance.

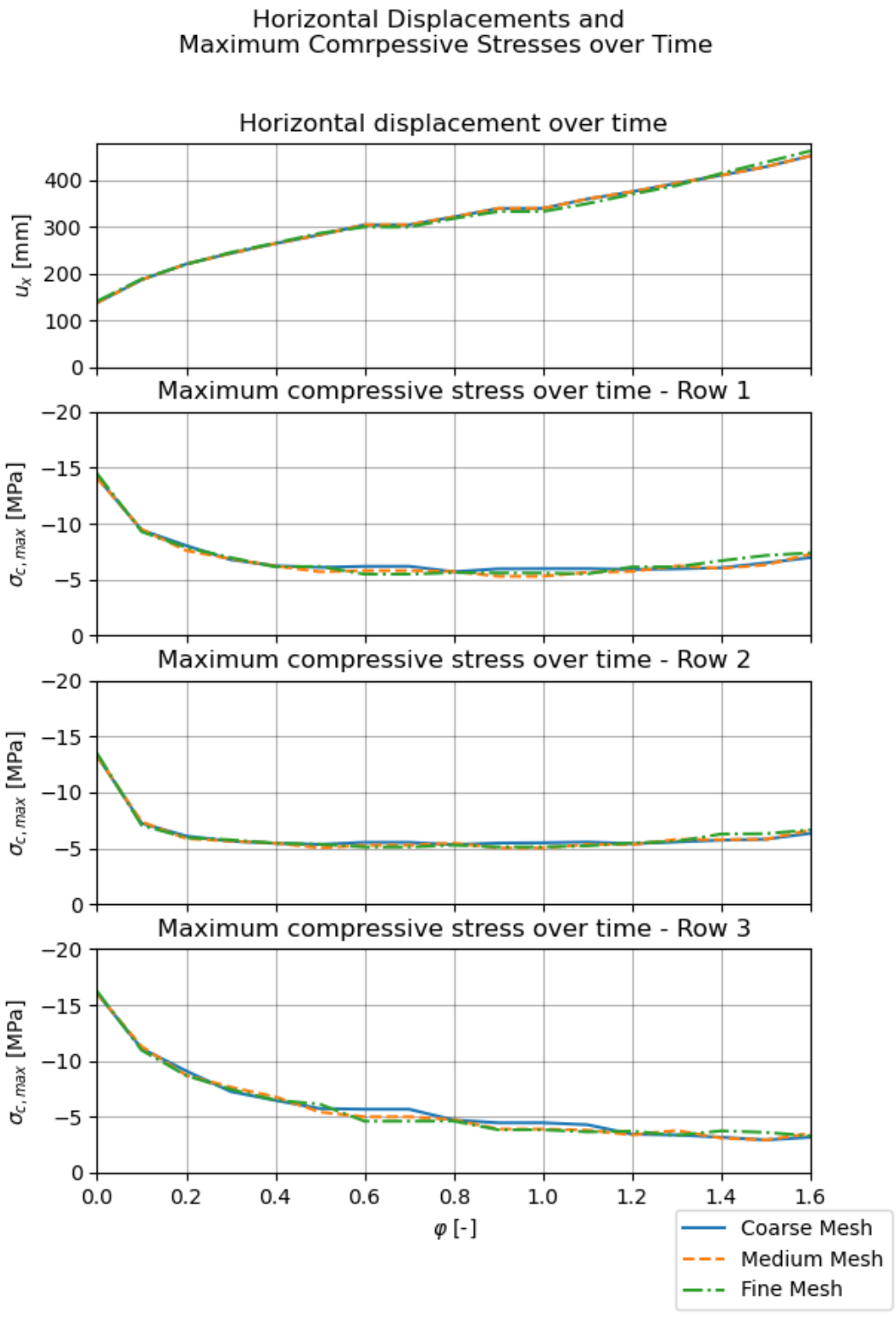

Figure 5.15: Horizontal displacements and maximum compressive stresses over time per row per mesh setting, obtained using Indirect phasing

5.4. Conclusion results timber creep Herengracht case

5.4.1. One step vs multiple steps

The creep has been modelled using two different methods; Direct, which applies the final creep factor in the same phase as the surface load, and Indirect, in which the final creep factor is applied in increments. From the results, it has been observed each method provides different results.

The Direct method resulted in smaller horizontal displacements, which were 75% lower than had been calculated using the Indirect method. When using the Direct method though, a larger final maximum compressive stress had been calculated in all pile rows In the Indirect method, calculated stresses were 49% up to 81% lower, depending on the pile row. This would suggest the piles carried less in the Indirect method. In addition, from the different bending moment distributions, it has been observed less potential energy due to bending is stored in the Indirect method. A load transferal from the piles to the subsoil and retaining screen had been observed to occur.

The difference in results is likely caused by the nonlinearity of the system. Material nonlinearity is introduced in the form of the soil models used. Furthermore, geometrical nonlinearity is present due to the updated mesh. Due to these nonlinearities, using one direct step or multiple ones results in different stress paths being followed. The Indirect method, using multiple increments, is considered to be the correct method for modelling creep. In reality, creep strains are being generated gradually and not in one instance. Using a final creep factor in this case is thus considered incorrect, as a different stress path could be triggered. The creep should be modelled using multiple steps, to better represent the gradual continuous creep generation that occurs in reality. As has been observed, using a single discrete step leads to different and possibly unsafe results. For these reasons, the Indirect method will be used for the sensitivity analysis in the next chapter.

5.4.2. Creep behaviour over time

When modelling the quay wall using increments in creep factor, more information can be obtained concerning the structural behaviour over time. It had been observed that the increase in horizontal displacement was larger for the first few creep steps. A good fit had been made using a power function in the form of $u = u_0 + A\varphi^m$. This form is often used to describe the primary and secondary stages of timber creep, with φ replaced with time. In the steps $\varphi = 0.7$ and 1.0, no new displacements had been calculated. This is likely due to a too small error created by the stiffness reduction from the creep factor.

The maximum compressive stress decreased in all pile rows for increasing creep factor. Similar to the displacements, the largest change occurred at lower creep factors. At around $\varphi = 0.4$, the maximum compressive stress in pile rows 1 and 2 stabilised. For row 3, the maximum compressive stress kept on decreasing, yet at a slower rate. The maximum bending moment showed similar behaviour as the compressive stress, whereas the maximum axial compressive force showed different behaviour, suggesting that the moment is governing for the stress. Bending moment distribution changes relatively more in the first creep steps and eventually stabilises. This suggests that most force redistribution within the pile takes place early on in the creep process. The surface area enclosed by the moment-curve, and hence the stored potential energy due to bending, decreases for increasing creep factors, again implying that the piles carry less load as time progresses. Thus, the safety against structural failure of the pile increases as creep progresses. While the piles carry less load, the retaining screen has to carry more, as a larger portion of the surface load is transferred downwards.

6

Sensitivity Analysis

A sensitivity analysis has been performed to study which parameters influence the creep behaviour of the quay wall. The following parameters have been varied by 20%; one calculation with a 20% higher value for the parameter, and one with a 20% lower value:

- Soil shear parameters, per layer, except the top sand layer:
  - c': Effective cohesion
  - $\tan(\varphi')$: Effective friction coefficient
  - G_0: Initial shear modulus. Due to Plaxis restrictions, this sometimes required E-moduli to be varied accordingly
  - $\gamma_{0.7}$: Shear strain at which the secant shear modulus has reduced to about 70% of G_0
- E_B: Initial elastic bending modulus timber
- Surface load
- ISF_{RN}: Lateral Interface Stiffness Factor (In addition, two calculations with +400% and -400% have been performed)
- Length retaining screen

In addition, the following:

- Applying the surface load only on top of the quay wall (x = 0 m to x = -4 m)
- Applying the surface load only behind the quay wall (x = -4 m to x = 10 m)
- Using a creep factor stepsize of 0.2, twice as large as in the reference case
- Using a creep factor stepsize of 0.05, twice as small as in the reference case
- Using a fixed pile-floor connection
- Adding a pile row at x = -2.35 m
- Inserting an unloading and a reloading phase after each creep step

For the analysis, the following measurements have been compared:

- The horizontal creep displacement
- The decrease in maximum compressive stress in pile row 1

The creep displacement and stress decrease have been determined as illustrated in Figure 6.1, based on the reference case. All measurements have been normalised to initial stress and displacement, as calculated after surface load application.

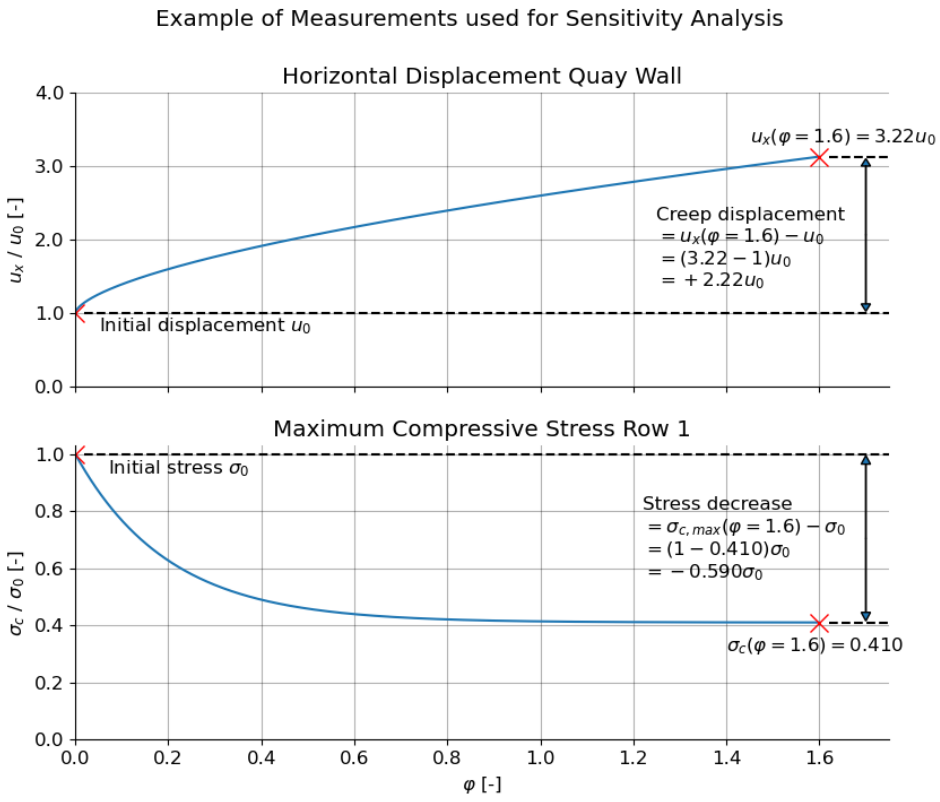

Figure 6.1: Illustration of the output used for comparison in the sensitivity analysis

For the reference case, the following stress and displacement ratios apply:

	$\varphi = 0.0$	$\varphi = 1.6$	**Net change**	**Relative net change**
u_x	131 mm	423 mm	+292 mm	+2.22
$\sigma_{c,max,row1}$	-14.0 MPa	-5.75 MPa	+8.27 MPa	-0.590

Table 6.1: Relative change due to creep in horizontal displacement and maximum compressive stress pile row 1, reference case

For the influence, the displacement and stress change is compared to that of the reference case. For the displacement, the reference number is +2.22, which was the relative creep displacement. For the stress, the reference number is -0.590. The influence is defined as how much the normalised creep displacement/stress is higher or lower compared to these numbers. This can be defined as:

$$
\begin{aligned}
Relative\ Influence\ Displacement &= \frac{\left(\frac{u_x(\varphi=1.6)-u_x(\varphi=0.0)}{u_x(\varphi=0.0)}\right)}{\left(\frac{u_{x,ref}(\varphi=1.6)-u_{x,ref}(\varphi=0.0)}{u_{x,ref}(\varphi=0.0)}\right)} - 1 \\
Relative\ Influence\ Stress &= \frac{\left(\frac{\sigma_{c,max,row1}(\varphi=1.6)-\sigma_{c,max,row1}(\varphi=0.0)}{\sigma_{c,max,row1}(\varphi=0.0)}\right)}{\left(\frac{\sigma_{c,max,row1,ref}(\varphi=1.6)-\sigma_{c,max,row1,ref}(\varphi=0.0)}{\sigma_{c,max,row1,ref}(\varphi=0.0)}\right)} - 1
\end{aligned}
\tag{6.1}
$$

In this chapter, results will primarily presented in tables. An example of such a table is presented in Table 6.2. At the end, the most influential parameters will be presented as a bar graph. A full overview of all results has been presented in Appendix G, Page 125.

Variation	**Creep displacement as factor of u_0 [-]**	**Relative to reference [-]**	**Stress decrease as factor of σ_0 [-]**	**Relative to reference [-]**
Reference case	*+2.22*	*0%*	*-0.590*	*0%*
Variation	+1.71 (*Example*)	$=\frac{+1.71}{+2.22}-1$ =-23.0%	-0.683 (*Example*)	$=\frac{-0.683}{-0.590}-1$ =+15.7%

Table 6.2: Example of results sensitivity analysis

Not all cases will be discussed in this chapter. For various cases, a negligible difference in relative change due to creep had been calculated. In addition, it has been observed that in some cases, calculated differences seemed to had been caused by numerical chance rather than having a real influence. An example has been presented in Figure 6.2. In here, the behaviour of the case in which the effective cohesion of layer 4, has been increased with 20%. It can be seen that the initial displacement and stress is near identical. In the last step, both stress and displacement are higher in the variance case than the reference one. However, for some creep factors the opposite is true, and in some cases the results are near identical. This phenomena is most likely from using a numerical method, in which results can deviate due to tolerances. Hence, cases with relative changes that only deviate 5 to 10% from the reference case might have negligible influence on the creep behaviour. Furthermore, some cases required the use of different numerical parameters to reach the final creep factor.

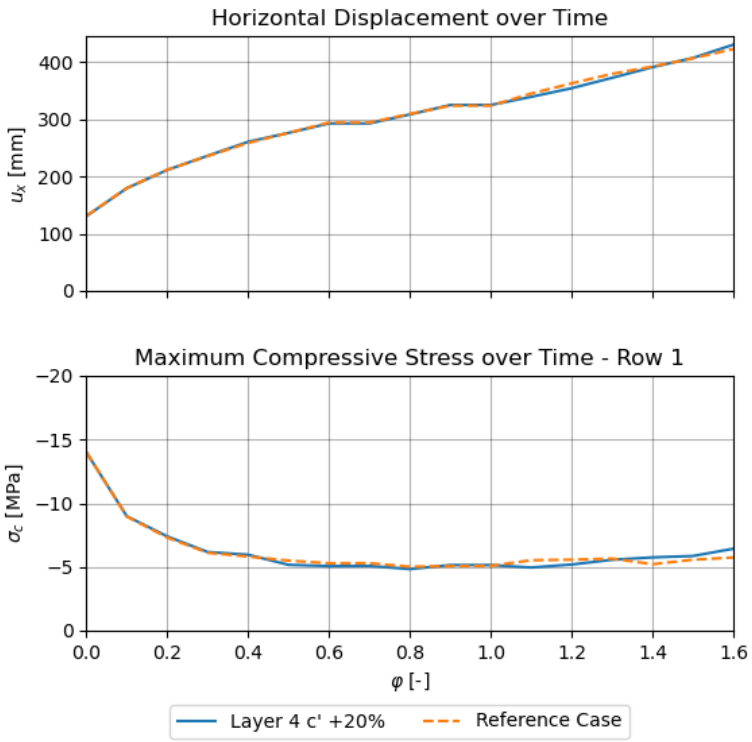

Figure 6.2: Comparison of the case "Layer 4 c'+20%" to the reference case. From the final step, it could be concluded that increasing the cohesion in layer 4 results in more displacement and stress. However, in some preceding steps, less displacement and stress has been calculated.

6.1. Influence geotechnical parameters on creep behaviour

Of all soil layers, the top Holland Peat layer has the most influence. This was to be expected, as the top layers are often dominant in the behaviour of laterally loaded piles. The results for this layer are presented in Table 6.3. When reducing either the effective cohesion or the friction coefficient with 20%, the soil body seemed to collapse and the final creep factor could not be reached. Increasing the cohesion resulted in 62% percent less relative creep displacement and 22% more stress reduction. Increasing the friction coefficient resulted in 31% less relative creep displacement and 31% more stress reduction. Changing the shear stiffness had a less significant influence; increasing it with 20% led to 11% less relative creep displacement and 5% more relative stress reduction. Reducing the shear stiffness had even less effect, with the difference in relative change reaching 5% or less. $\gamma_{0.7}$ seems to have no influence on the creep behaviour.

Results sensitivity analysis - Layer 2: Holland Peat

Variation	**Creep displacement as factor of u_0 [-]**	**Relative to reference [-]**	**Stress decrease as factor of σ_0 [-]**	**Relative to reference [-]**
Reference case	*+2.22*	*0%*	*-0.590*	*0%*
c' +20%	+0.843	-62.1%	-0.718	+21.8%
c' -20%	N.A. †	N.A.	N.A.	N.A.
G_0 +20%*	+1.99	-10.5%	-0.622	+5.40%
G_0 -20%*	+2.34	+5.19%	-0.583	-1.12%
$\gamma_{0.7}$ +20%	+2.15	-3.34%	-0.576	-2.33%
$\gamma_{0.7}$ -20%	+2.24	+0.82%	-0.562	-4.70%
tan(φ') +20%*	+1.54	-30.8%	-0.77	+30.5%
tan(φ') -20%	N.A. †	N.A.	N.A.	N.A.

Table 6.3: Results sensitivity analysis creep influence - layer 2 "Holland Peat"
*: different numerical parameters have been used in one or more phases to reach final creep factor
†: the quay wall had collapsed before reaching the final creep factor

For the deeper layers, most variations result only deviate 5% compared to the reference case. In addition, several variations resulted in a 5 to 10% change, of which a part had been obtained using different numerical parameters. Only two variations showed a variation larger than 10%. One of these variations is the increase of $\gamma_{0.7}$ of layer 6, the first sand layer. However, decreasing $\gamma_{0.7}$ in the same layer has a negligible influence. Furthermore, varying $\gamma_{0.7}$ in any other layer has shown to have little influence. Hence it has been chosen to disregard this result. The other variation that showed more than 10% influence was the decrease of tan(φ') of the third layer.

6.2. Influence surface load on creep behaviour

The results of the sensitivity analysis concerning the surface load are presented in Table 6.4 on the next page. From the results it can be observed that both the magnitude as well as the location of the load has a significant influence on the creep behaviour. When increasing the load by 20%, the relative creep displacement is 93% larger compared to the reference case, and the relative stress decrease is only 9.3% of the reference one. This means that for larger loads, creep displacements increase significantly while compressive stresses remain high. When reducing the load by 20%, relative creep displacements are 31% less and the stress reduction is 18% more. The results of varying the magnitude of the surface load have been plotted in Figure 6.3 for closer inspection.

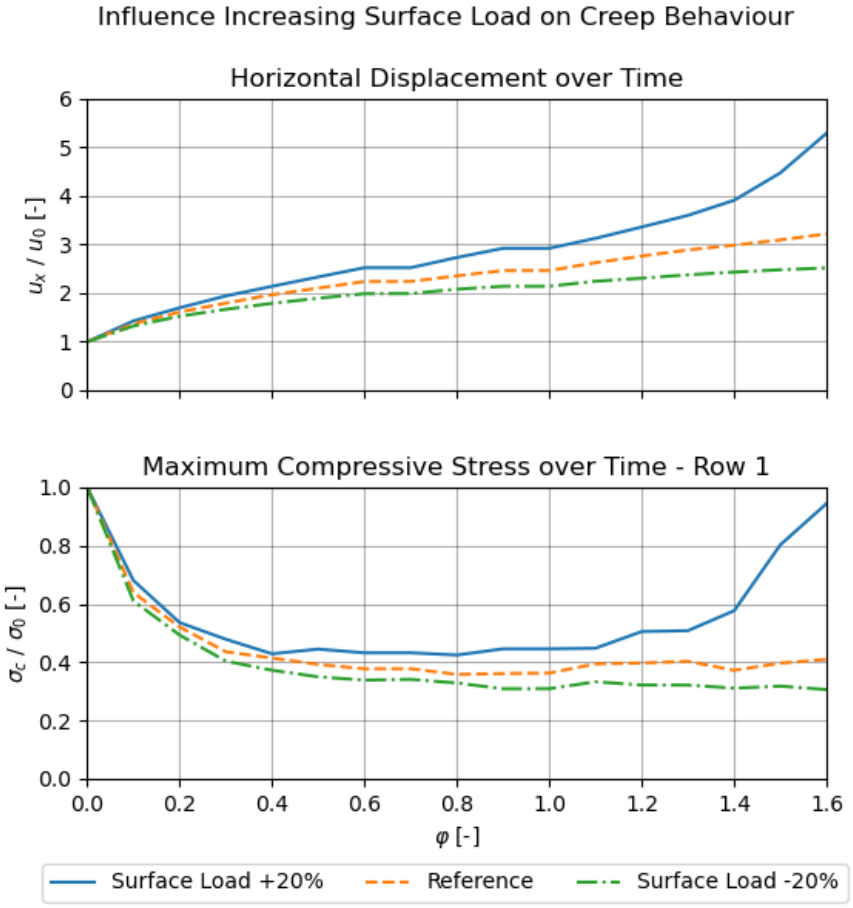

Figure 6.3: Influence magnitude surface load on creep behaviour

In Figure 6.3 it can be seen that the behaviour of the case with 20% larger surface load deviates from other observed behaviour. At around $\varphi = 1.2$, the displacement rate increases, and the total displacement seems to increase exponentially. This last section of the displacement curve takes a shape similar to the tertiary stage presented in the general creep curve presented in Figure 2.7, Page 9. This is the final stage of creep, which eventually ends in failure of the structure. Furthermore, Figure 6.3 shows how the maximum compressive stress starts to increase around the same $\varphi = 1.2$. It can be concluded that this case had entered the final tertiary stage. This is the only case this has been observed in.

When the surface load was only present on top of the quay wall, the relative creep displacement drops significantly, to only 78% of the initial displacement, 65% less than in the reference case. The stress decrease increases with 13%. Similar numbers have been obtained when applying the load only behind the quay wall; the relative creep displacement decreases with 57% and the relative stress relaxation increases with 33%, in comparison to the reference case. A part of this change is most likely due to the total amount of surface load.

A calculation has been performed with an unloading and a reloading phase after each creep factor increment. This has been performed to see whether the creep behaviour is susceptible to hysteresis. The behaviour of the unloading and reloading calculations has been plotted over time in Figure 6.4. From both Table 6.4 as well as Figure 6.4 it can be seen that unloading and reloading resulted in a negligible difference in creep behaviour.

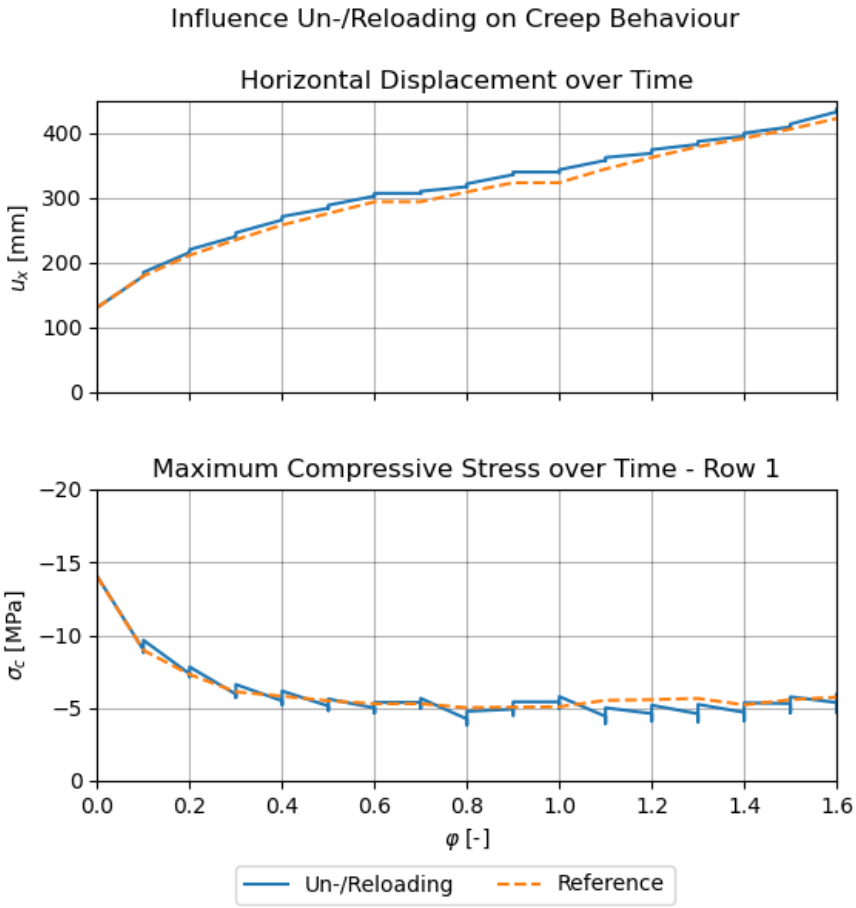

Figure 6.4: Influence unloading/reloading on creep behaviour

Variation	**Creep displacement as factor of u_0 [-]**	**Relative to reference [-]**	**Stress decrease as factor of σ_0 [-]**	**Relative to reference [-]**
Reference case	*+2.22*	*0%*	*-0.590*	*0%*
Surface load +20%*	+4.29	+93.2%	-0.0550	-90.7%
Surface load -20%*	+1.52	-31.5%	-0.693	+17.6%
Load behind quay wall	+0.969	-56.4%	-0.782	+32.6%
Load on top quay wall	+0.778	-65.0%	-0.672	+14.0%
Un-/reloading	+2.33	+4.99%	-0.577	-2.27%

Table 6.4: Results sensitivity analysis creep influence - surface load
*: different numerical parameters have been used in one or more phases to reach final creep factor

6.3. Influence structural elements on creep behaviour (Retaining screen, additional pile row, pile-floor connection)

In the determination of the geometrical several assumptions have been made concerning the layout of the structure. Therefore, calculations have been made to study the influence of these assumption. These assumptions included the length of the retaining screen as well as the rigidity of the pile-floor connection. Moreover, it is suspected that at other locations an additional pile row would be present between the second and third one, at x=-2.35 m. The results of these calculations are presented in Table 6.5.

Changing the length of the retaining screen shows a noticeable effect on the creep behaviour. When increasing the length, the relative creep displacement decreases with 29%, whilst the relative stress decrease is 10% larger. Decreasing the length results in 13% more displacement and 15% less stress reduction. In addition, the initial displacement and stress have been found to be equal to the reference case.

Adding an additional pile row results in a decrease in creep displacement and an increase in stress relaxation. This situation is alike the case for which the surface load had been reduced, in which the net load per pile had also been reduced. When adding a pile row, the total load is distributed over four piles instead of three, resulting in a lower net load per pile.

Using a fixed pile-floor connection instead of hinged provided peculiar results. For most other variations, the relative creep displacement would increase and the stress reduction decrease, or vice versa, given a non-negligible change occurred. However, in the case of the fixed pile-floor connection, both the relative creep displacement as well as the stress reduction increased, with respectively 8.2% and 19%. Both initial and final displacement and stress were lower compared to the reference case.

Variation	**Creep displacement as factor of u_0 [-]**	**Relative to reference [-]**	**Stress decrease as factor of σ_0 [-]**	**Relative to reference [-]**
Reference case	*+2.22*	*0%*	*-0.590*	*0%*
Retaining screen +20%	+1.58	-29.0%	-0.647	+9.74%
Retaining screen -20%	+2.51	+13.1%	-0.502	-14.9%
Additional pile row	+1.91	-14.2%	-0.643	+8.95%
Fixed pile-floor connection	+2.40	+8.19%	-0.704	+19.4%

Table 6.5: Results sensitivity analysis creep influence - structural elements

6.4. Influence initial bending modulus on creep behaviour

The results of varying the initial bending modulus of the timber are presented in Table 6.6. The results show that changing the initial bending stiffness has a significant influence on the creep behaviour. When increasing the initial modulus, relative creep displacements drop with 23% and the stress relaxation increases with 16%. When reducing E_B, effects are even more pronounced, with the relative creep displacement being 42% more and the stress relaxation 68% less compared to the reference case. In both cases, the initial displacement and stress deviated only 10%.

Variation	**Creep displacement as factor of u_0 [-]**	**Relative to reference [-]**	**Stress decrease as factor of σ_0 [-]**	**Relative to reference [-]**
Reference case	*+2.22*	*0%*	*-0.590*	*0%*
E_B +20%	+1.71	-23.0%	-0.683	+15.7%
E_B -20%	+3.15	+41.5%	-0.188	-68.2%

Table 6.6: Results sensitivity analysis creep influence - initial bending stiffness E_B

6.5. Influence Lateral Interface Stiffness Factor on creep behaviour

During the verification it had already been observed that a drastic change in ISF-value is required to obtain noticeable changes in results. Hence, in addition to varying the value with 20%, two supplementary calculations have been executed in which the ISF has been varied with a factor 5. The results of these calculations are presented in Table 6.7. The only noticeable result had been obtained by decreasing the ISF with a factor 5. By doing so, the relative creep displacement increased with 6.5% and the stress relaxation decreased with 16%.

As already discussed Chapter 3, Page 16, the influence of the ISF is limited. Here it had been stated that the Embedded Beam Row interface and the soil can be modelled as springs in series. Increasing the ISF, and thus the stiffness of the EBR interface, has no influence on the system stiffness when above a certain value. It seems that also for the creep behaviour, the ISF has an upper limit on the range of values for which it has an influence on the pile behaviour.

Variation	**Creep displacement as factor of u_0 [-]**	**Relative to reference [-]**	**Stress decrease as factor of σ_0 [-]**	**Relative to reference [-]**
Reference case	*+2.22*	*0%*	*-0.590*	*0%*
ISF_{RN} +20%	+2.18	-2.04%	-0.562	-4.66%
ISF_{RN} -20%	+2.17	-2.57%	-0.609	+3.23%
ISF_{RN} x5	+2.25	+1.13%	-0.569	-3.51%
ISF_{RN} /5	+2.37	+6.53%	-0.493	-16.4%

Table 6.7: Results sensitivity analysis creep influence - Lateral Interface Stiffness values

6.6. Influence creep factor stepsize on creep behaviour

In Chapter 5 it had already been observed that it matters if the final creep factor is applied immediately or using increments. Therefore, two calculations have been performed in which the size of the creep factor increments has been halved or doubled. The final relative creep displacement and stress decrease are presented in Table 6.8. In addition, the behaviour over time has been plotted in Figure 6.5 alongside the reference case.

Variation	**Creep displacement as factor of u_0 [-]**	**Relative to reference [-]**	**Stress decrease as factor of σ_0 [-]**	**Relative to reference [-]**
Reference case	*+2.22*	*0%*	*-0.590*	*0%*
$\Delta\varphi$=0.05*	+2.16	-2.77%	-0.600	+1.70%
$\Delta\varphi$=0.2	+1.83	-17.6%	-0.584	-1.07%

Table 6.8: Results sensitivity analysis creep influence - creep factor step size
*: different numerical parameters have been used in one or more phases to reach final creep factor

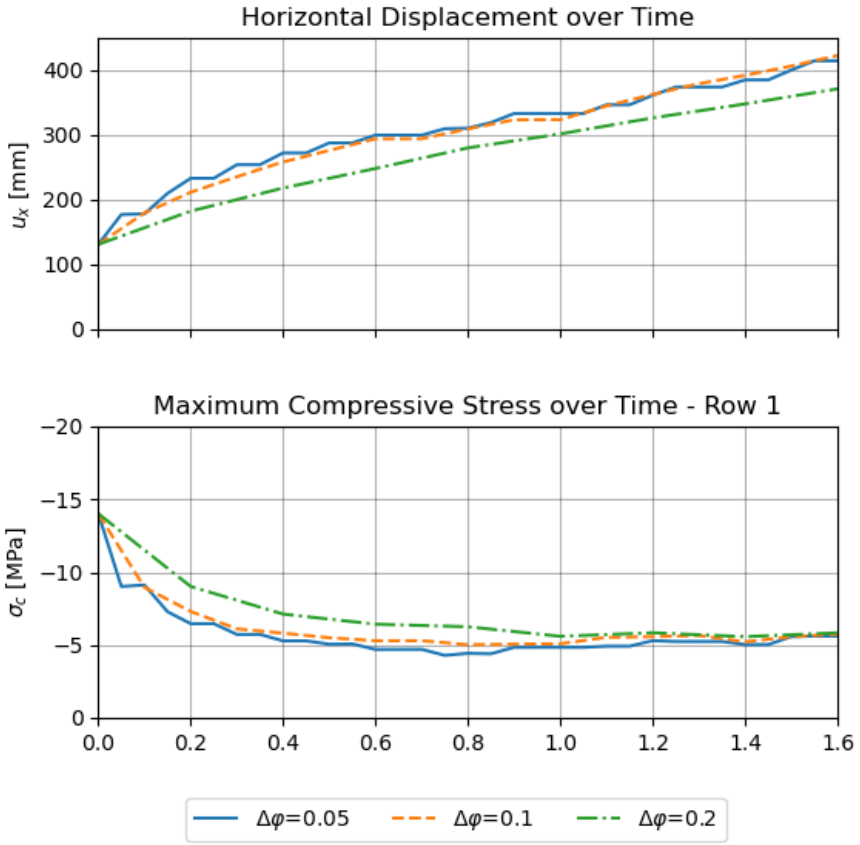

Figure 6.5: Creep behaviour over time for various creep factor step sizes

The results in Table 6.8 show that for a smaller step size, the results are close to those obtained in the reference case. On the other hand, when increasing the step size, the results for the displacement deviates. When using $\Delta\varphi$=0.2, the relative creep displacement is 18% lower. When looking at Figure 6.5, it can also be observed how the larger step size results in smaller displacements in each time step. Furthermore, the stress calculated using the larger stepsize aligns with the other two graphs in the final creep steps, but deviates in those prior. For creep factors smaller than 1.0, the larger step size predicts higher stresses.

When using smaller step sizes, the behaviour over time does deviate significantly from the reference case. Figure 6.5 shows how the graph from $\Delta\varphi$=0.05 follows the one from $\Delta\varphi$=0.1 closely. As stated in Section 5.2, Page 42, the displacements and stress have not been updated for each creep step. For the smaller step size, this occurred more often in comparison to the reference case. As explained earlier, Plaxis does not perform a calculation these phases, as the force imbalance introduced due to the creep strength reduction was too small. Given that these phases do not require computation time, and that the results in φ = 1.6 are not influenced either, there seems to be no harm in using smaller step sizes.

6.7. Conclusion sensitivity analysis creep behaviour

The results of the parameters deemed most influential are presented in Figures 6.6 and 6.7. The figures show the result of a 20% increase or decrease of the various parameters.

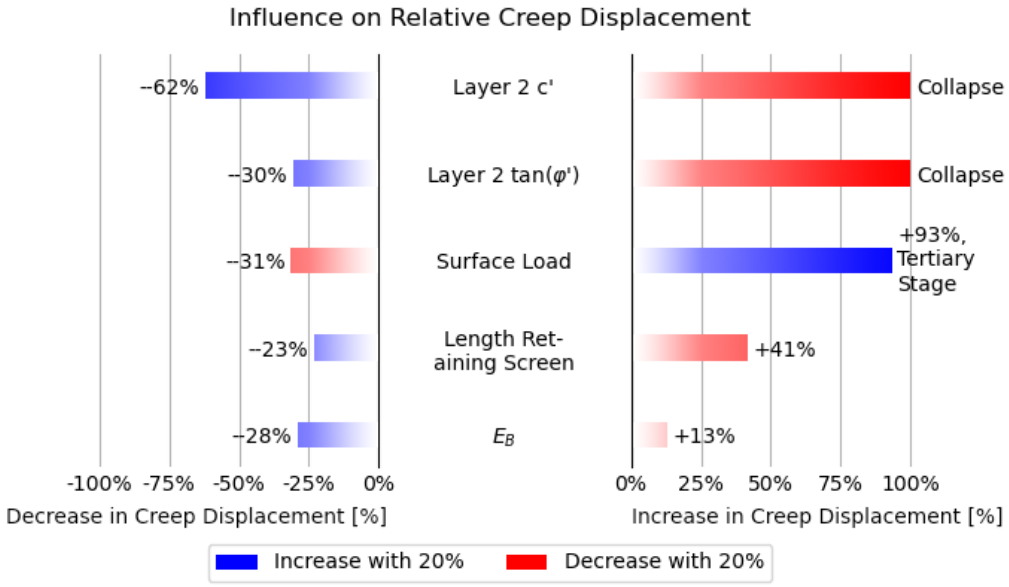

Figure 6.6: Influence of important parameters on relative creep displacement

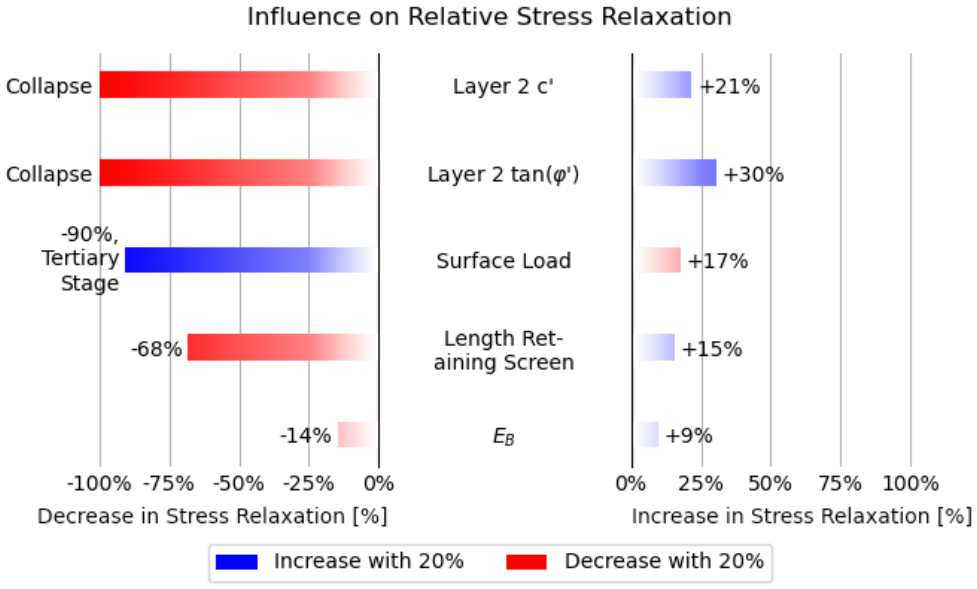

Figure 6.7: Influence of important parameters on relative stress decrease

The results showed that only the top Holland Peat layer showed significant influence on the creep behaviour of the quay wall. Variations of parameters in other layers mostly resulted in negligible differences. The shear strength parameters c' and $\tan(\varphi')$ have the largest influence, as lowering these seemed to cause collapse over time. Varying the initial shear stress stiffness G_0 presented a lower variation in results, and the influence of $\gamma_{0.7}$ can be considered as insignificant.

Calculations have shown the influence of the surface load on the quay wall. Increasing the load with 20% nearly doubled the relative creep displacement, whereas reducing it by the same value led to 65% less dis-

placement. Respectively, stress reduction decreased with 91% for larger loads and increased with 31% for smaller ones. It had been concluded that the case with increased surface load had entered the tertiary creep stage. From $\varphi = 1.2$, displacements grew exponentially and stresses started to increase. Changing the area over which the surface load is applied resulted in different creep behaviour. However, it is possible this has partially been caused by a change in total surface load. Unloading and reloading appeared to have little influence on the creep behaviour.

It has been observed that the elastic bending modulus of the piles has a significant influence on both the relative creep displacement as well as the stress change. Besides increasing the surface load, reducing E_B led to the largest relative creep displacement as well as the smallest stress reduction. Hence, it can be concluded that the bending stiffness of the piles has a major influence on the creep behaviour. When taking into account a reduced bending stiffness due to damage and deterioration, this effect could worsen.

Similar to the direct response, the Interface Stiffness Factor has limited influence on the creep behaviour of laterally loaded piles. From a certain point onward, increasing the ISF does not influence the results, as the stiffness of the interface elements has become too large compared to the stiffness of the soil. Reducing the ISF-value sufficiently can result in relatively larger creep displacements and less stress reduction.

Knowing the exact geometry of the quay wall has shown to result in considerable more accurate results. Changing the length of the retaining screen resulted in reasonably large differences in relative creep displacements and stress changes. Furthermore, the number of piles has shown to affect the creep behaviour. Adding a fourth pile gave results which were alike those obtained with a smaller surface load; the initial load and stress are lower, but the relative creep displacement larger and the stress reduction less. Modelling the pile-floor connection as fixed resulted in more stress reduction, but also more creep displacement. This is opposite to all other variations, in which either the reduction increased and the displacement decreased, or vice versa.

7

Varying Creep Factors per Pile Row

For all previous calculations, the same creep factors have been used for each structural element. However, as has been stated in the literature study, the creep rate is often stress-dependent. In the results from Chapter 5 it has been observed how the pile rows each have different stresses. Hence, each pile row should have had a different creep rate and thus different creep factor increment. Furthermore, it has been calculated that the stress decreases over time. A lower stress often means the creep rate decreases, resulting in less displacement.

A calculation has been performed in which different creep factors have been applied per pile row. For pile row 2, the default creep factors have been applied, increasing the factor in steps of 0.1 until the final creep factor of 1.6 has been reached. For pile row 1, the final creep factor, and hence the step size, has been increased with 20%. For pile row 3, the creep factor have been reduced with 20%.

Pile Row	$\Delta\varphi$	φ_{final}
1	0.12	1.92
2	0.10	1.60
3	0.08	1.28

Table 7.1: Values used for the calculation with different creep factors per pile row

The creep behaviour of these calculations have been plotted in Figure 7.1 on the next page. In the final stage, 8.3% less creep displacement has been calculated. The stresses calculated in the final step are nearly identical to those in the reference case. However, the stress paths over time deviate from the reference case. For row 1, stresses at some creep steps are larger compared to the reference. For row 2 and 3, the stress is sometimes lower compared to the reference. It is unclear what caused these deviations. The results suggest that using different creep factors per pile has little influence on the creep behaviour. The displacement curve is close to the reference case. Furthermore, the final stresses calculated are near identical to the reference case. Nevertheless, given the deviations occurring at some creep factors, these results should not be considered conclusive.

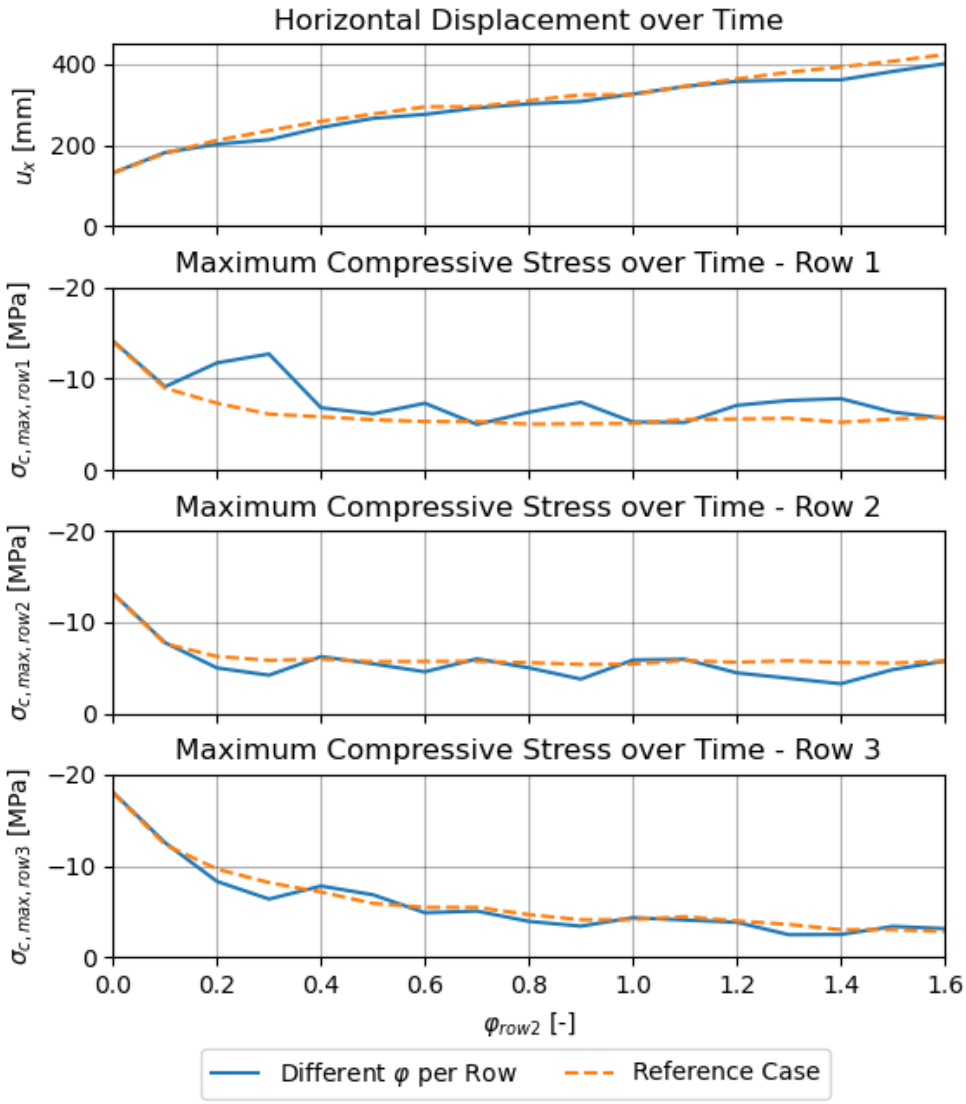

Figure 7.1: Creep behaviour over time, for different and same creep factors per pile

8

Interaction with Soil Creep

In all previous calculations, the influence of the soil creep has been left out. In reality, soil creep will likely occur alongside the wood creep. There are two reasons as of why the soil creep has been omitted from this study. The first reason is the lack of adequate material model. At the time of writing, no proven material model was present that could model both creep as well as lateral loading properly. The model that has been used, the Hardening Soil model with small strain stiffness, allows for modelling of shear loading as is the case with quay walls. However, HSsmall does not incorporate soil creep. Models that do accommodate for creep, such as the Soft Soil Creep model, lack the ability to properly simulate shear loading inherent to laterally loaded piles. Secondly, little research was available concerning the influence of soil creep on laterally loaded piles. Kuppusamy and Busloc (1987) performed an elastic-creep analysis to predict horizontal displacements of laterally loaded piles, but did not include force distribution. Moubarak et al. (2018) modelled laterally loaded piles using FEM, in which it had been reported maximum bending moment increases due to soil creep, Nevertheless, results had been obtained by using the Soft Soil Creep model, which is unsuitable for modelling laterally loaded piles. It is recommended to include soil creep as a part of further study after this MSc project.

However, research on a similar problem can be used; the behaviour of laterally loaded piles embedded in ice or permafrost. Ice has shown to also have time-dependent properties. Multiple studies have been found concerning the influence of ice creep on the response of the pile-subgrade system. For example, Puswewala et al. (1993) modelled the creep response of laterally loaded piles in ice using plane strain finite element analyses, validated by 3D continuum element analyses. As presented in Figure 8.1, they predicted an increase in maximum bending moment and total bending energy over time. This is the opposite as to what was happening during the wood creep, as was presented in Figure 5.12, Page 45. In this figure it had been observed how due to timber creep, the maximum bending moment as well as total internal bending energy decreased for increasing creep factor. The soil creep might thus negate a part of the stress reduction that has been predicted as part of the wood creep.

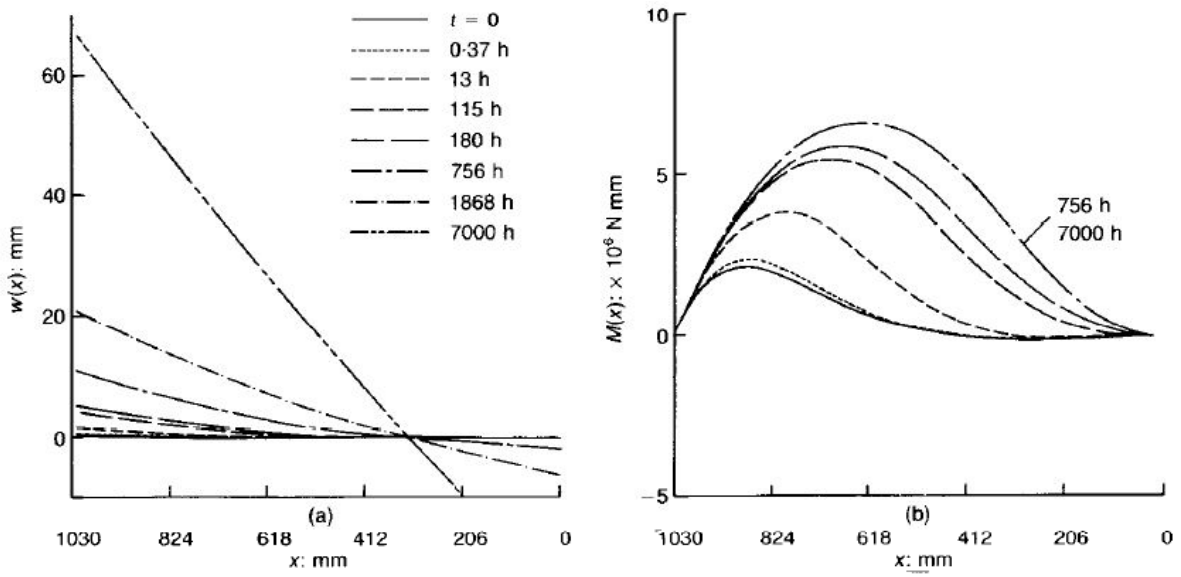

Figure 8.1: Example of predicted response of laterally loaded piles in ice. (a) Horizontal displacement over depth at various moments in time. (b) Bending moment over depth at various moment in time (Puswewala et al., 1993)

The soil creep is expected to have an effect on the creep behaviour. Using the same analogy of modelling the soil-pile systems as springs coupled in series, as used earlier in Figures 3.9 and 3.10, Page 23, Figure 8.2 has been made. When using the pseudo-elasticity principle to model soil creep, the first graph can be formed. In here, a less stiff force-displacement curve is shown to model creep response. The second graph shows how the pseudo-elasticity influences the stress-strain behaviour of the pile. In the third graph, the equivalent spring stiffness of the pile-soil-series system has been plotted. This has been done for various cases:

- No creep included
- Including wood creep
- Including soil creep
- Including wood and soil creep

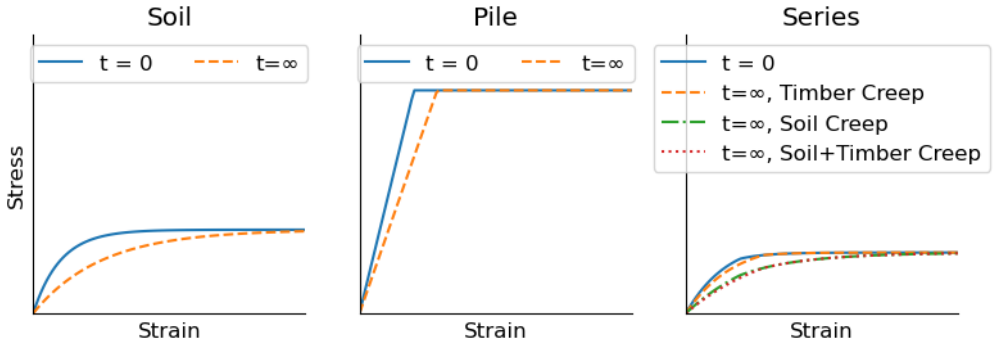

Figure 8.2: Schematisation of response of pile-soil system, prior and after the creep process, using pseudo-elasticity

It is likely that in most cases, the stiffness of the piles is far larger than the stiffness of the soil. In Figure 8.2, when applying wood creep using pseudo-elasticity, the system stiffness changes only slightly. It can also be observed that the system stiffness changes more significantly when applying soil creep via pseudo-elasticity. As long as the stiffness of the pile is sufficiently larger in comparison to the soil stiffness, it is likely for the soil creep to be dominant. The lower the pile stiffness will become in comparison, the larger its part in the overall pile-soil behaviour. This does not suggest that the wood creep is negligible, the contrary has been observed in Chapter 5. It is recommended to carry out research concerning the influence of the soil creep on the behaviour of laterally loaded piles. This is both due the analogy presented in Figure 8.2 as well as the results from Puswewala et al. (1993) concerning the influence of ice creep, as has presented in Figure 8.1.

Conclusions

The main goal was to study the influence of timber creep on the assessment of quay walls by evaluating the structural behaviour. The quay walls have been modelled using the Embedded Beam Row from Plaxis 2D. The EBR has been validated using the full-scale pile loading carried out in Salt Lake City, consisting of a 3x5 laterally loaded pile group in a mix of cohesive and non-cohesive soils. Using the EBR, a model of a typical Amsterdam quay wall has been modelled, which was based on the Herengracht. The following step consisted of implementing creep into the EBR material model in the form of pseudo-elasticity, in which the stiffness decreases with increasing creep factors. The stiffness reduction had been applied by using a custom moment-curvature diagram to invoke out-of-balance forces. The results implied that wood creep has a noticeable effect on the structural behaviour of the quay wall. Based on the results, the research questions can be answered as follows:

1. To what extent is the Plaxis 2D Embedded Beam Row adequate for modelling the structural behaviour, that is force distribution and displacements, of laterally loaded foundation piles in multi-layered cohesive and non-cohesive soils?

The results from the Salt Lake City model have shown that the Embedded Beam Row is able to provide reasonably accurate results when simulating laterally loaded piles. The force-displacement curve obtained from Plaxis 2D showed good correspondence with the experimental results. In addition, the group efficiency was close to those as had been reported, only deviating at small displacements. These deviation was most likely caused by the exclusion of installation effects in the EBR model. The force distribution within the piles differed slightly from those during the experiment. Some piles carried more load in comparison to as had been reported, others less. Furthermore, the maximum bending moments obtained using the EBR were lower than had been measured. The manual of the EBR suggests that the Interface Stiffness Factors should be varied in order to calibrate the Plaxis model. Yet, it has been observed that beyond a certain value, increasing the ISF no long has a noticeable impact on results. Above a certain value, the ISF values will have made the interface elements significantly stiffer than the soil, rendering them as practically rigid links. Furthermore, during the sensitivity analysis on the timber creep with the Herengracht case, it has been observed that the ISF had limited influence on the results, as only a noticeable change occurred when the factor was decreased by a factor 5. Nevertheless, it has been concluded that the Embedded Beam Row provides sufficiently realistic results when used for modelling laterally loaded pile groups in cohesive soils. The overall behaviour as predict for the Salt Lake City case showed good correspondence with the experimental data. In addition, it must be noted whether this full-scale test can be considered 2D, as there were only 3 pile rows parallel to the modelled plain. It is important to answer the question whether a situation can be represented as 2D, prior to using the Embedded Beam Row model.

2. What is the influence of timber creep on the structural behaviour of quay walls?

The results show that the inclusion of timber creep in a combined structural and geotechnical finite element model of a quay wall has a noticeable effect on the force distribution and displacements. The horizontal displacement increased over time. In the final time step, additional creep displacements equal to 2.22 times the initial displacement had been reached. The displacement rate was larger for lower creep factors. Furthermore, the displacement-creep factor curve could be described using a power law, which is often used for describing the first two stages of timber creep. It has also been observed that for increasing creep factor, the maximum compressive stresses decreased. During the creep process, the stresses in the front two pile rows reduced by 59% relative to the initial stresses. This reduction had been reached at $\varphi = 0.4$, after which the stresses stabilised. In the third pile row, the most landin one, stress continued to reduce over time. From the bending moment distributions it has been observed that the potential energy stored within the pile rows decreased over time. Due to the decrease in stored bending energy, as well as the decreased stress, it can be concluded that the total group of piles carry less shear load over time. The lateral traction over depth showed that the soil pressure along the pile changes over time, indicating a redistribution of forces. The sensitivity analysis showed that the creep behaviour is dominated by the shear parameters of the top section of the sub-

soil. In the Herengracht case, only the top layer had an affect on creep behaviour, all others layers showed negligible influence. In addition to the top layer, the creep behaviour is heavily influenced by the surface load, initial bending modulus of the wood and the geometry of the quay wall structure. For the case with an increased surface load, the displacement rate increased towards the end. At the same time, the stresses increased within the piles. It has been concluded that in this case, the quay wall had entered the tertiary creep stage, which would end in rupture of the wood and thus structural failure.

3. How is the creep behaviour affected by the the time step discretisation?

It has been observed that different results for creep behaviour are obtained when applying the final creep factor directly or incremental, here labelled as "Direct" and "Indirect". In the case of Direct modelling, less creep displacement but more stresses were predicted compared to the Indirect modelling. Using one step as in the Direct method is deemed incorrect, as it does not realistically model the gradual generation of creep strains. When studying the behaviour over time, it has been observed that the total creep displacement and stress change are influenced by the size of the time step. When using more time steps, the results converge to one result. Using smaller time steps than necessary results in Plaxis not performing calculations each step, but does not affect final displacement and stress. Using too large steps leads to underestimating the displacement and overestimating stresses. It can thus be argued that the Direct modelling is incorrect, as it uses one large time step. Sufficiently small time steps are required to properly model the creep behaviour over time.

How does the inclusion of timber creep influence the modelling and assessment of urban quay walls?

Including timber creep in the modelling of the urban quay wall has shown to have a significant impact on the structural behaviour of the urban quay wall. By taking into account the creep via pseudo-elasticity, it has been observed how results in stresses and displacement change over time. When including wood creep, additional strains are being generated resulting in more horizontal displacement. In addition, a stress reduction has been observed in the foundation piles of the quay wall. The stress reduction in the front two pile rows had been reached at $\varphi = 0.4$, after which stresses stabilised. During the sensitivity analysis, the case with a higher surface load showed that stresses could increase. In this case, the stress decreased up to $\varphi = 0.4$, then stabilised, and started to increase at $\varphi = 1.2$. The inclusion of timber creep can change our view on the state, and the actual stress state, of the quay wall. One of the failure mechanisms of quay walls is failure due to excessive displacements. Including creep behaviour in the calculation models can attribute a part of the observed deformations to creep. When considering creep deformation in service life assessments, the serviceability limit state could be exceeded earlier. Nevertheless, occurrence of excessive displacements due to creep does not mean the quay wall has reached an ultimate limit state. Instead, timber creep can also lead to a relaxation of stresses under permanent load and a higher safety margin for variable load. Another failure mechanism of quay walls is the structural failure of the foundation piles due to bending and compression. As the results show an initial stress reduction, it has been concluded that the timber creep can lead to a better safety against this failure mechanism. However, as the piles carry less, more load is transferred to the retaining screen.

Including the creep of laterally loaded piles can change the modelling and assessment of quay walls. This study has shown how the inclusion of timber creep can result in different stresses and displacements. If excessive deformations are being measured in existing quay walls, it is possible a part of these deformations are due to timber creep. Observing these excessive deformations does not necessarily mean structural failure of the timber elements has occurred.

Recommendations

Whilst it is not one of the originally intended purposes, the Embedded Beam Row can be used for the modelling of laterally loaded pile groups, to some extent though. It was shown that relatively accurate results can be obtained concerning force distribution and displacements, especially in comparison to other 2D methods such as the use of anchors to model piles. Nevertheless, more verification with focus on cohesive soils is recommended. The default Interface Stiffness Factors have been derived from tests performed in non-cohesive soils. In the Salt Lake City case as well as the Herengracht case, these factors were deemed to be too low. Furthermore, the effective range of the ISF parameters has an upper bound; increasing the ISF value beyond this has a negligible influence, limiting how well the model can be calibrated.

The second recommendation is to take the timber creep into account during the modelling and assessment of old urban quay walls. The results have shown that displacement and force distributions differ significantly hen compared to a case for which the creep is omitted. To properly model the creep behaviour, sufficient increments in creep factor are required. Too large steps will result in an underestimation of the creep displacement and stress decrease.

The next recommendation is to determine which age corresponds to the creep factors used in this study. The quay wall has been modelled at different moments in time. The chronological order of these moments is known. However, their location in real-time, as well as the time between moments, is unknown. As of now, this type of calculation only provides possible states as in which the quay wall can be in. For example, results have shown that stress decreases until it stabilises at around φ=0.4, but it is unknown when this creep factor has been reached. Furthermore, in the case of increased surface load, a point of inflection had been found around φ = 1.2, after which displacement rate and stresses increased. To obtain more accuracy concerning the current state of quay walls, research should be carried out in order to convert the creep factors to years. To do so, it is suggested to perform creep tests on laterally loaded piles, or preferably a quay wall, to obtain an empirical creep law. Gressel (1984) suggests that data from creep tests lasting 5000 hours, approximately 7 months, can be used to reasonably predict creep behaviour over a time span of 10^6 hours, or 114 years. With experimental data on timber creep, it is likely that the current safety of quay walls can be assessed more accurately.

For further research, it is recommended to investigate the possibility of taking into account soil creep in the analysis of laterally loaded piles. As has been stated in Chapter 8, no adequate soil model was available to incorporate both shear loading as well as creep. However, it is expected to influence the deformations and stresses within the quay wall structure. Kuppusamy and Busloc (1987) used a simple one-dimensional finite element formulation to perform elastic-creep analyses. From field data as well as calculation results they concluded that the soil creep has a significant influence on the displacement of laterally loaded piles in cohesive soils.

For the validation of the results, it is recommended to perform a physical test and not numerical ones. A 3D FEM program can be used to validate the EBR. However, this would not help with validating the timber creep. Furthermore, the results in this study have been obtained using pseudo-elasticity in the form of creep factors. In order to properly validate these results, a creep model for the timber is required, which can be empirical or mechanical. At the time of writing, no empirical creep law was deemed to be applicable for quay walls. As for mechanical models, these can be implemented in FEM software, but requires validation themselves. A load test would be the preferred method. As stated above, Gressel (1984) suggests that a load test of approximately 7 months can be used to predict creep behaviour for up to 114 years.

Bibliography

Alpan, I. (1970). The geotechnical properties of soils. *Earth-Science Reviews*, 6:5–49.

Amsterdam, G. (2020). Bruggen en kademuren. `https://www.amsterdam.nl/parkeren-verkeer/bruggen-kademuren/`. Date accessed: 2020-07-06.

Banerjee, P. and Davies, T. (1978). The behaviour of axially and laterally loaded single piles embedded in non-homogeneous soils. *Geotechnique*, 28(3):309–326.

Bentley Systems (2013). Reduction of stiffness does not lead to a change in displacements. `https://www.plaxis.com/support/tips-and-tricks/reduction-of-stiffness-does-not-lead-to-a-change-in-displacements/`. Date accessed: 2020-05-14.

Bentley Systems (2014). Points of interest for pile modelling in a 2D plane strain model. `https://www.plaxis.com/support/tips-and-tricks/points-of-interest-for-pile-modelling-in-a-2d-plane-strain-model/`. Date accessed: 2020-03-17.

Blaß, H. and Sandhaas, C. (2017). *Timber Engineering - Principles for Design*. KIT Scientific Publishing, Straße am Forum 2, D-76131 Karlsruhe.

Brinch-Hansen, J. (1961). The ultimate resistance of rigid piles against transversal forces. *The Danish Geotechnical Institute Bulletin*, 12.

Buffon, G. L. L. D. (1741). *Experiences sur la force du bois*, volume 453. Paris L'Academie Royale des Sciences.

Dabek, A. and van Geloven, I. W. (2019). 1900913-XL. Technical Report 1820215, Lankelma Geotechniek Zuid B.V.

DIN-52-186 (1978). Testing of wood; bending test. Technical report, Deutsches Institut für Normung.

Gijt, J. G. d. (2010). *A History of Quay Walls*. PhD thesis, Delft University of Technology.

Gressel, P. (1984). Zur Vorhersage des langfristigen formänderungsverhaltens aus kurz-kriechversuchen. *Holz als Roh- und Werkstoff*, 42:293–301.

Hardin, B. O. and Drnevich, V. (1972). Shear modulus and damping in soils: design equations and curves. *Journal of the Soil Mechanics and Foundations Division*, 98:667–692.

Herbschleb, J. (1999). Parameterset holocene lagen. Technical Report (12)11.435, OMEGAM.

Holzer, S. M., Loferski, J. R., and Dillard, D. A. (1989). A review of creep in wood: Concepts relevant to develop long-term behavior predictions for wood structures. *Wood and Fiber Science*, 21(4):376–392.

Kelder, M. A. o. (2015). 2D FEM analysis compared with the in-situ deformation measurements: A small study on the performance of the HS and HSsmall model in a design. *Plaxis Bulletin*, 38:10–17.

Kránitz, K. (2014). *Effect of natural aging on wood*. PhD thesis, ETH Zürich.

Kuppusamy, T. and Busloc, A. (1987). Elastic-creep analysis of laterally loaded piles. *Journal of Geotechnical Engineering*, 113(4):351–365.

Lemnitzen, A., Khalili-Tehrani, P., Ahlberg, E. R., Rha, C., Taciroglu, E., Wallace, J. W., and Stewart, J. P. (2010). Nonlinear efficiency of bored pile group under lateral loading. *Journal of Geotechnical Engineering*, 136:1673–1685.

Maagdelijn, D. W. and Philippart, M. A. (1988). Brug 112 over de Lauriergracht; grondconstanten. Technical Report 6014.0, Grondmechanica Amsterdam.

Mayne, P. and Kulhawy, F. (1982). K0–OCR relationships in soil. *Journal of the Geotechnical Engineering Division*, 108:851–872.

Moubarak, A. H., Hafez, K. H., and Ibraheem, K. M. (2018). Behaviour of laterally loaded flexible piles in soft clay. *Life Science Journal*, 15(7).

Plaxis (2019a). *Plaxis 2D Reference Manual Connect Edition V20*. Plaxis.

Plaxis (2019b). *Plaxis Material models manual 2019*. Plaxis.

Poulos, H. and Davis, E. (1980). *Pile Foundation Analysis and Design*. John Wiley & Sons Inc., New York.

Puswewala, U. G. A., Rajapakse, R. K. N. D., Domaschuk, L., and Shields, D. (1993). Creep response of laterally loaded piles in ice and permafrost. *Geotechnique*, 43(2):223–240.

Ravenshorst, G., Gard, W., and de Vries, P. (2016). Timber structures 1 CIE4110. TU Delft Lectures.

Rollins, K. M., Peterson, K. T., and Weaver, T. J. (2003). Lateral load behaviour of full-scale pile group in clay. *Journal of Geotechnical and Geoenvironmental Engineering*, 124(6):468–478.

Ruiter, L. H. J. d. (2015). Funderingsinsepctie brug 20 + 21 incl. aangrenzende kades. Technical Report 26442, NEBEST adviesgroep.

Sluis, J. (2012). Validation of embedded pile row in Plaxis 2D. Master's thesis, Delft University of Technology.

Sluis, J., Besseling, F., Stuurwold, P., and Lengkeek, A. (2013). Validation and application of the embedded pile row-feature in Plaxis 2D. *Plaxis Bulletin*, pages 10–13.

Snyder, J. L. (2004). Full-scale lateral-load tests of a 3x5 pile group in soft clays and silts. Master's thesis, Brigham Young University, Brigham, Utah.

Thurston, R. H. (1895). *Materaials of Construction*. John Wiley, New York.

van de Dienst Openbare Werken; Centraal Tekeningen Archief, A. (1905). 17523 kademuren. vernieuwen kademuren Herengracht voor nieuwe spiegelstraat en beulingstraat. `https://archief.amsterdam/inventarissen/details/10057/keywords/17523`.

Verkuil, D., van Riessen, M., and van Straaten, D. (2011). *Geschiedeniswerkplaats: De Republiek in een tijd van vorsten*. Noordhoff Uitgevers bv, Groningen / Houten.

Vicat, L. T. (1834). Note sur l'allongement progressif du fil de fer soumis à diverses tension. *Annales, Ponts et Chaussées*, 7.

Visser, G. T. (1988). Gegevens grondgesteldheid en de geohydrologie ter plaatse van de jordaan. Technical Report 4351.0, Grondmechanica Amsterdam.

Walraven, J. C. and Braam, C. R. (2018). *CIE4160 Prestressed Concrete*. Delft University of Technology; Faculty of Civil Engineering and Geosciences, Delft.

Wichtmann, T. and Triantafyllidis, T. (2009). On the correlation of "static" and "dynamic" stiffness moduli of non-cohesive soils. *Bautechnik*, 86:28–39.

Yong Technology Inc. (2020). PyPile. `http://www.yongtechnology.com/pypile/`. Date accessed: 2020 June 24.

I

Appendices

A

Input and Modelling EBR Verification Case

This appendix contains the information on verification of the Embedded Beam Row. A brief overview of the verification case, based on Salt Lake City load-tests, is provided. The appendix contains the input data used to model the Embedded Beam Row verification case, with derivation of the data included. Furthermore, the method of modelling is explained in full detail. This is done for each software that has been used. Finally, a full overview of the results is provided. The analysis of the results has been done in Chapter 3, Page 16.

A.1. EBR verification case description: Salt Lake City

The case that has been used for the verification of the Embedded Beam Row is the load-test on a laterally-loaded pile group at Salt Lake City International Airport, as reported by Snyder (2004). The report covers the testing of a single pile as well as a 3x5 group. The pile group was connected via a rigid frame. The load and displacement applied on each pile were measured. Furthermore, strain versus depth was measured at the front and back of all centre piles, which was in turn used to calculate resulting bending moments. The top section of the soil consists mainly of soft cohesive layers with some sandy layers, similar to the Herengracht subsoil. An overlying gravel layer was excavated prior to testing, and later testing showed the subsoil was overconsolidated.

The remainder of this section will provide a brief summary of Original report including relevant information. For the full description of the field case, please review the original report by Snyder (2004).

A.1.1. Pile group setup

The testing setup consisted of a single pile, a 3x5 pile group and a pair of drilled shafts. A top view of the pile plan is presented in Figure A.1

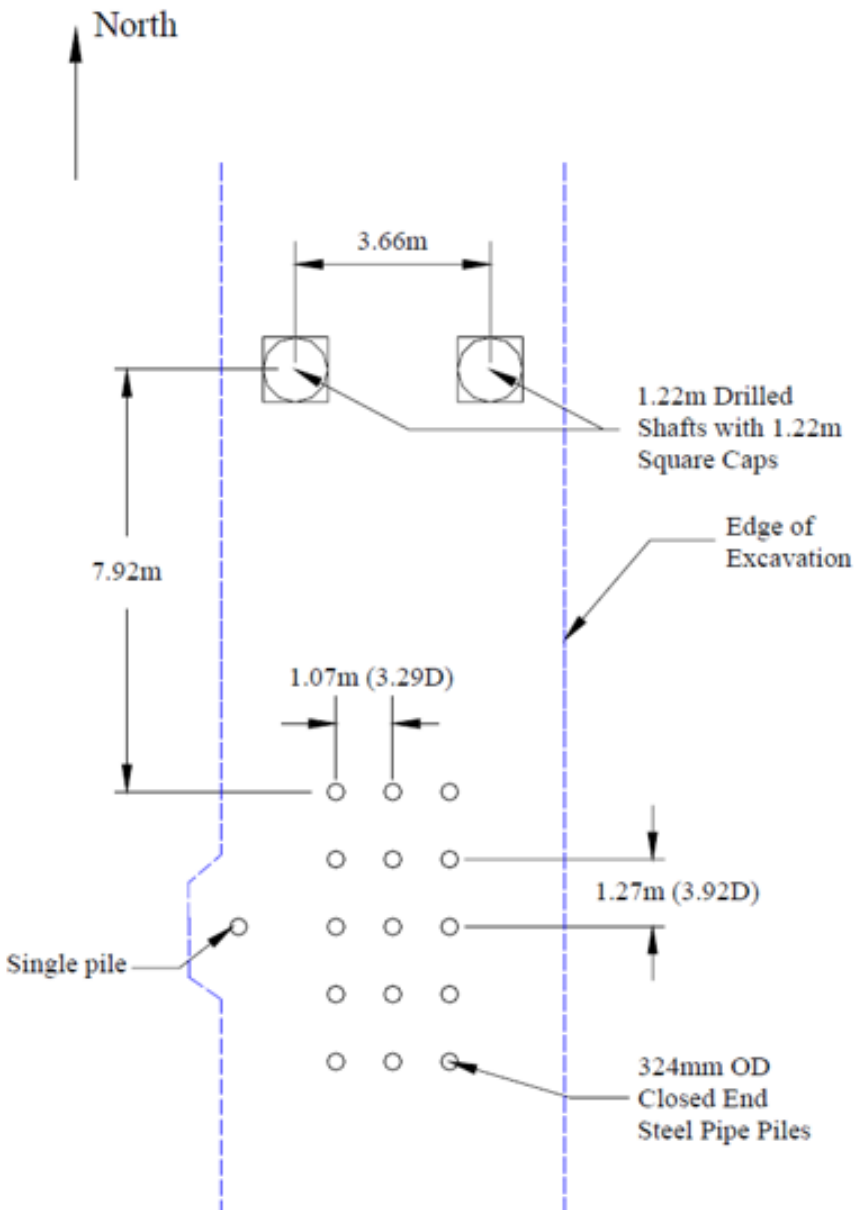

Figure A.1: Topview pile plan Salt Lake City case (Snyder, 2004)

First, testing was performed on the single pile. The data of the single pile test was to be used later to determine group efficiencies. Furthermore, computer modelling was used to validate the test data using p-multipliers. The testing was done by attaching a steel beam to the pile group and connecting a hydraulic jack to it and the single pile. The connection was realised using a swivel, meaning only horizontal loads should occur. The load was applied 0.495 m above surface level. The pile group was deemed to be relatively stiff and used as a reference point for measuring displacements. A top view of the setup can be found in Figure A.2.

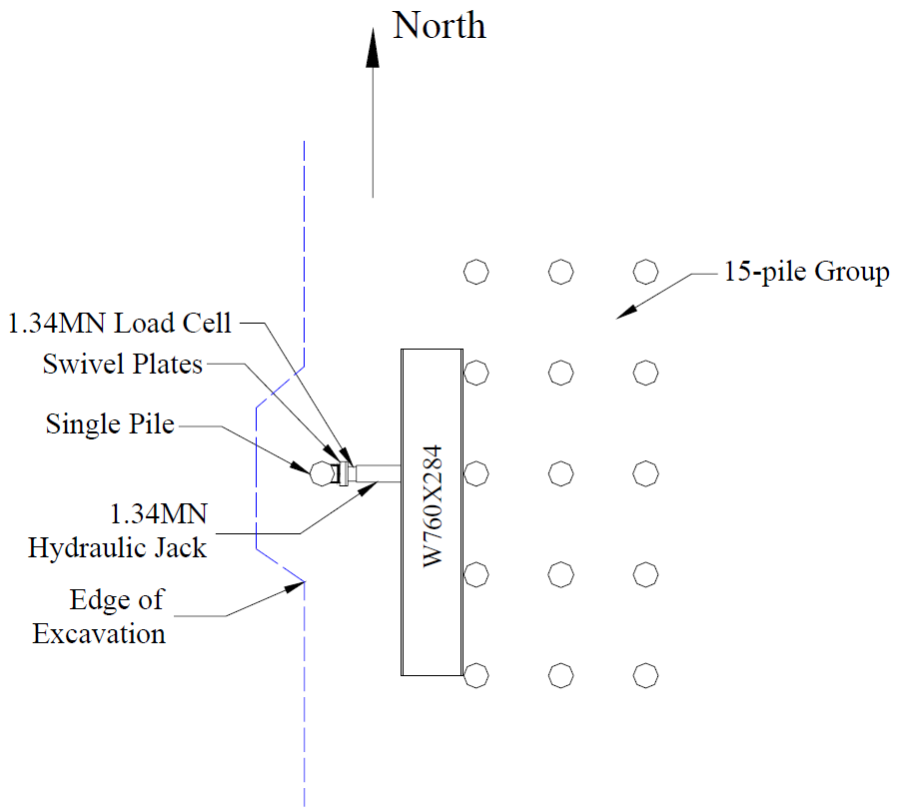

Figure A.2: Topview single pile loading test Salt Lake City case (Snyder, 2004)

For the testing of the group, two drilled shafts were used as "fixed points". On each of the shafts, a hydraulic jack was placed, which in turn would push against a steel beam. The steal beam was connected via rods to the frame of the pile group, thus introducing the load. Again, the loads were introduced using swivel plates, as to allow for free rotation and vertical displacement. The pile group consists of 5 rows in direction of loading, and 3 perpendicular. The longitudinal c.t.c pile spacing was equal to 3.92D, the perpendicular one 3.29D. Schematised top and side views have been presented in the following figures, along with several photographs.

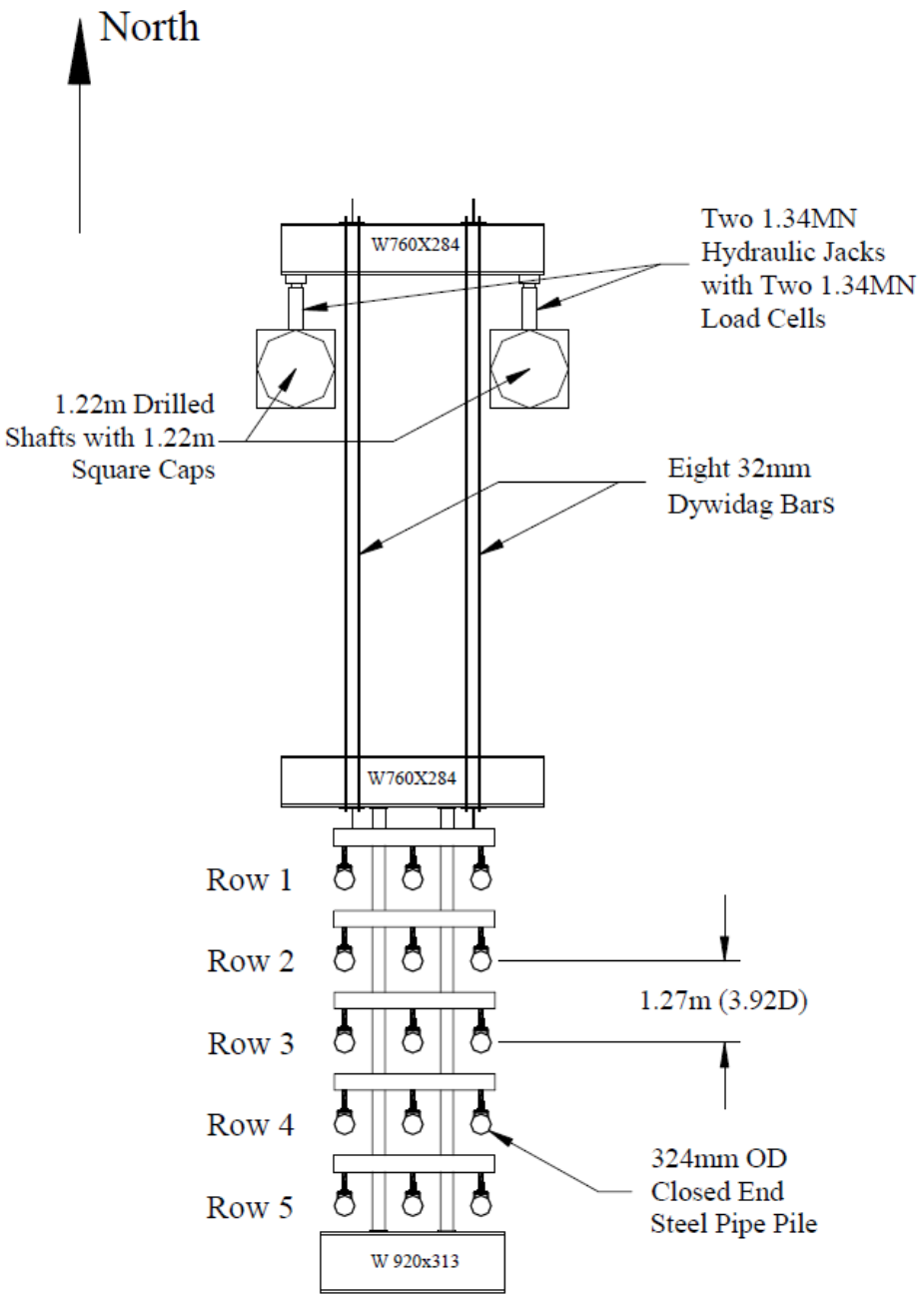

Figure A.3: Topview pile group loading test Salt Lake City case (Snyder, 2004), with North row being row 1

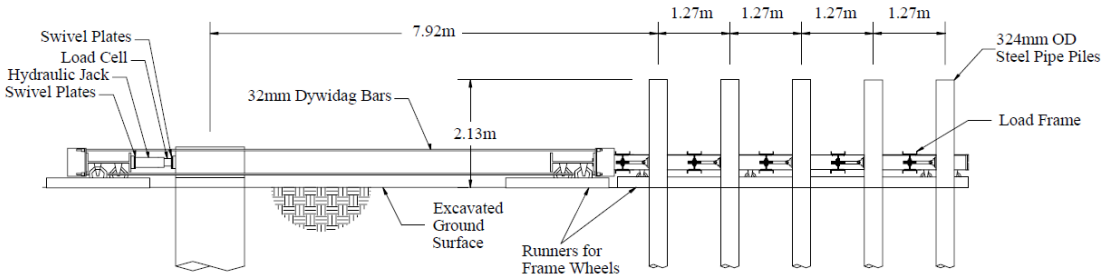

Figure A.4: Side view pile group loading test Salt Lake City case (Snyder, 2004), with left row being row 1

Figure A.5: Pile group loading tests Salt Lake City case (Snyder, 2004)

Each pile was outfitted with an LVDT and a tie-rod cell to measure displacement and load. Furthermore, the two drilled shafts were also hooked up to tie-rod cells. In order to measure bending moments over depth, strain gauges were applied to all centre piles. They were applied in pairs, one at the north and one at the south side of the pile. Pairs of gauges had been placed at several depths along the pile.

A.1.2. Geotechnical site description

The site had been used multiple times for load-testing of piles prior to 2002. As a result, there was already a collection of data available on the site. Further field- and lab-tests had been performed, including CPTs, triaxial tests and oedometer tests. An idealisation of the soil was made by Snyder, presented in Figure A.6

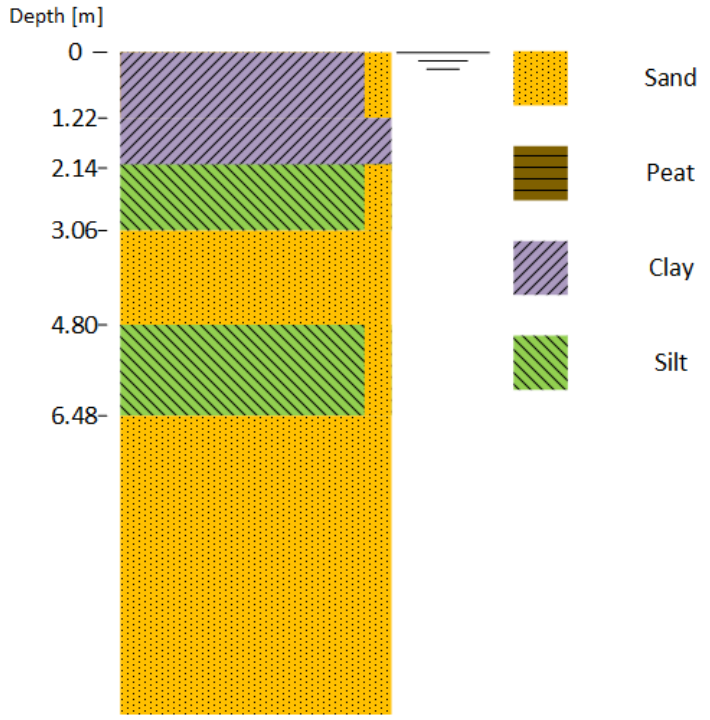

Figure A.6: Idealised soil profile Salt Lake City case

For the computer modelling performed afterwards, the following soil properties had been determined:

Layer	**P-y curve**	**Depth bottom** $[m]$	$\gamma'[kN/m^3]$	$s_u[kPa]$	$\epsilon_{50}[-]$	$\varphi[°]$	$k[kN/m^3]$
1 Sandy lean clay	Soft Clay (Matlock)	1.22	9.05	41.4/100 [1]	0.010	N.A.	N.A.
2 Lean clay	Soft Clay (Matlock)	2.14	9.05	60.0	0.010	N.A.	N.A.
3 Sandy silt	Soft Clay (Matlock)	3.06	9.05	40.0	0.010	N.A.	N.A.
4 Silty sand	Sand (Reese)	4.80	8.14	N.A.	N.A.	38.0	25.5E+06
5 Sandy silt	Soft Clay (Matlock)	5.33	9.05	56.9	0.010	N.A.	N.A.
6 Sandy silt	Soft Clay (Matlock)	5.87	9.05	25.0	0.015	N.A.	N.A.
7 Sandy silt	Soft Clay (Matlock)	6.48	9.05	54.0	0.010	N.A.	N.A.
8 Poorly graded sand	Sand (Reese)	N.A.	8.14	N.A.	N.A.	33.0	14.9E+06

Table A.1: Determined soil properties Salt Lake City case according to Snyder (2004). 1: A value of 100 kPa was determined from field tests, but a value of 41.4 kPa was used for the computer models, as this provided a better fit

A.1.3. Piles

For the Salt Lake City case, 324x9.5 steel tubular piles were used. Within each of the five rows, the centre pile was outfitted with strain gauges at intervals along the pile. In order to protect the measuring equipment, steel angular segments were welded the pile, covering the gauges. This resulted in an increase in the moment of inertia and cross-sectional area of the pile. Hence, the moment of inertia of the centre piles differ from the outer ones. In the computer modelling, it seems the increased cross-sectional area was not used, presumably under the assumption that axial deformation was negligible. The pile had a total stickup of 2.13 m, but the load was applied 0.495 m above the surface level. The following properties apply for the piles:

Parameter	**Value**	**Unit**
$D_{outside}$	324	mm
t	9.5	kN/m^3
A	9400	mm^2
E	200	GPa
I_{outer}	1.16E+08	mm^4
I_{centre}	1.43E+08	mm^4
$L_{embedded}$	11.575	m
L_{free}	2.13	m
Height load application above surface level	0.495	m

Table A.2: Pile properties Salt Lake City case

A.1.4. Testing procedure

The pile group testing consisted of eight target deflections. Cyclic testing was to be performed on the pile group. The following procedure has been followed:

1. Apply load until target deflection has been reached
2. Sustain load for 5 minutes for manual collection of data and instrumentation check
3. Release load
4. Reload and unload the pile group 14 additional times, with the same target deflection
5. Repeat steps 1-4 for each target deflection

Several problems had occurred during the testing:

- At higher deflections, fewer cycles had been performed due to time limitations
- Target deflections were not reached exactly, which was corrected for in the original data
- Discrepancies were found in peak loads between the load-cells at the piles and the drilled shafts. It was claimed the cause was due to misalignment of the hydraulic jacks on the load cells, as well as excessive friction on the swivel heads connecting the piles to the frame. Thus, realignment was carried out and additional grease was applied. This took place after the cycle for 38 mm deflection was completed
- Not all strain gauges on the pile function. Several had been damaged during transport, installation or testing of the pile group. If for a given depth only one strain gauge was malfunctioning, it had been assumed the strain was equal and opposite to the other gauge in the pair. In some cases, both gauges in a pair were damaged
- Cave-in occurred during loading at the active side of the piles, preventing them to return to their original position after unloading

A.1.5. Computer modelling

LPile

Both the single pile as well as the pile group loading was modelled using P-y curve based software. For the single pile, the software LPile was used. The software models the pile as a beam-column and uses Finite Difference Method to determine bending moments and deflections (Snyder, 2004). The soil parameters and models are as described in Table A.1 and a pile as described in Table A.2, using the properties of a centre pile. As stated earlier in Table A.1, a different undrained shear strength was used for the top layer to better fit results. No information was found concerning the analysis settings of the software, such as tolerated error or amount of elements.

GROUP

For the simulation of the pile group, the software GROUP was used. GROUP uses similar P-y software as LPile. To take into account group effects, p-multipliers are used, which scale the P-y curve. In this case, the p-multiplies were back-calculated to fit the results of the field test. Different p-multipliers had been calculated for displacements smaller than 38 mm and larger. The following p-multipliers have been obtained:

Row	1	2	3	4	5
Displacement [mm]					
<38	1.0	0.87	0.64	0.81	0.70
>38	1	0.81	0.59	0.71	0.59

Table A.3: Calculated p-multipliers Salt Lake City case

The results of the computer modelling have been presented alongside the field test in the following section.

A.2. Results Testing and Computer Modelling Salt Lake City Case

Multiple variables had been measured during the Salt Lake City testing. In this section, the group load as function of average group displacement are presented. Furthermore, the average load per pile per row is presented, as function of the displacement of the corresponding row. Next, the maximum moment per pile per row is presented as function of the pile load. Several remarks have to be made on the data beforehand:

- All data has been read from graphs from the original report
- It was reported that average row displacements could vary up to 10 % compared to the average group displacement. However, all load-displacement data was plotted against average group displacement

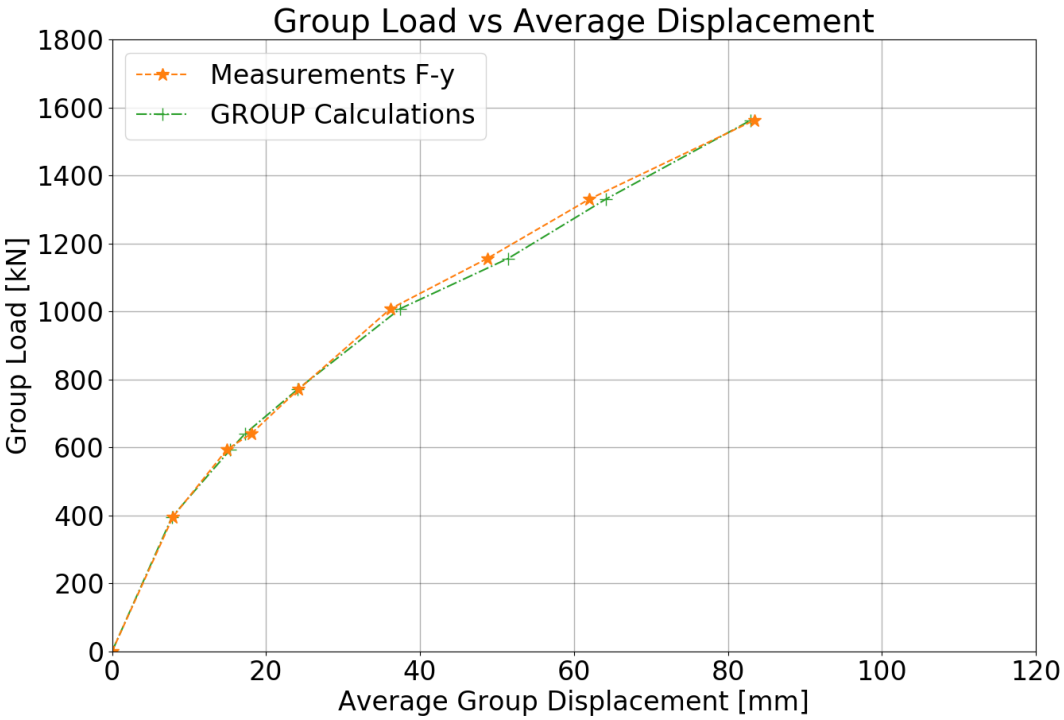

Figure A.7: Load-displacement curve pile group, field measurements and GROUP calculations from Salt Lake City case

In Figure A.7, a shift in the curves can be seen between 38 and 51 mm target group displacement. As stated earlier, the hydraulic jacks had been realigned between these steps, alongside the application of additional grease to reduce friction. It is most likely this is the cause for this shift. As the input of GROUP is based on the measurements, a shift can be seen here as well.

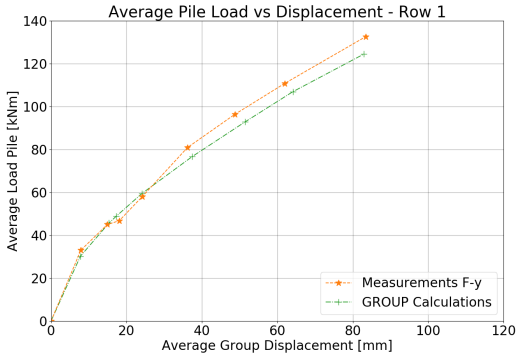

(a) Average pile load versus group displacement, row 1

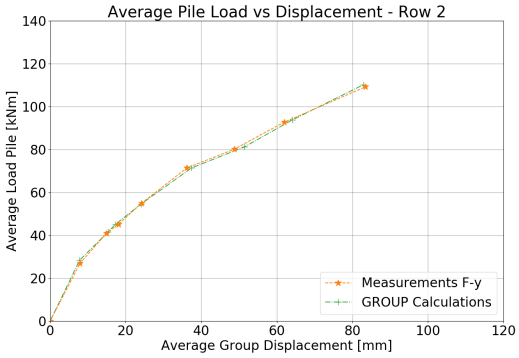

(b) Average pile load versus group displacement, row 2

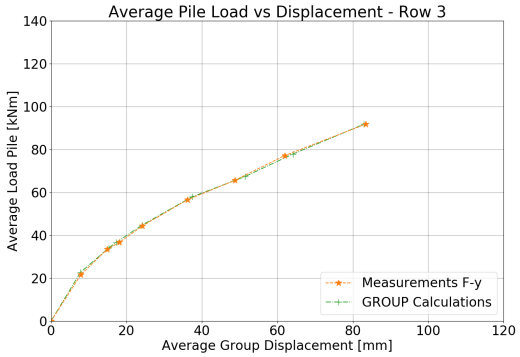

(c) Average pile load versus group displacement, row 3

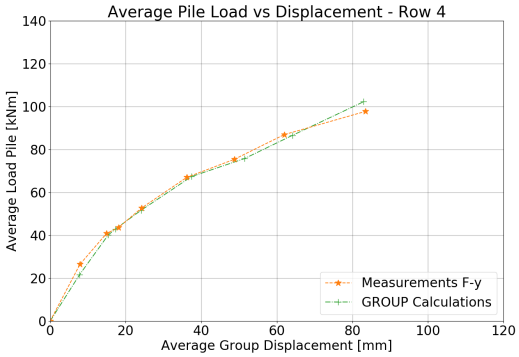

(d) Average pile load versus group displacement, row 4

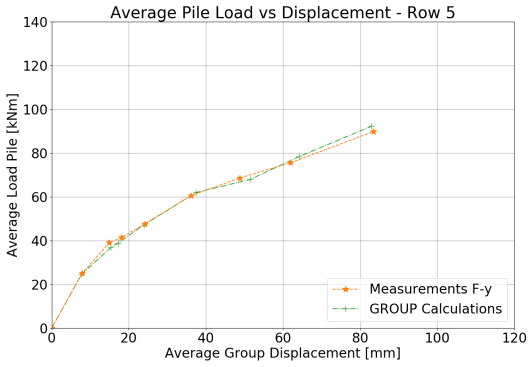

(e) Average pile load versus group displacement, row 5

Figure A.8: Load-displacement curve averaged per pile row, field measurements and GROUP calculations from Salt Lake City case

Figures A.8a through A.8e show the load-displacement curve for each pile row. Generally speaking, the front row carries the most load. For other rows, different results have been found. Lemnitzen et al. (2010) provides a summary of obtained row efficiencies from different tests. In here, it can be found that in some cases, the trailing rows carry more load than the centre ones. In other cases, the trailing rows carry the least. In the case of the Salt Lake City testing, the trailing row seems to carry less than the centre ones. However, the 3rd row carries less load than rows 2 and 4. The original author claims this is unlikely behaviour and most likely due to local difference in soil composition.

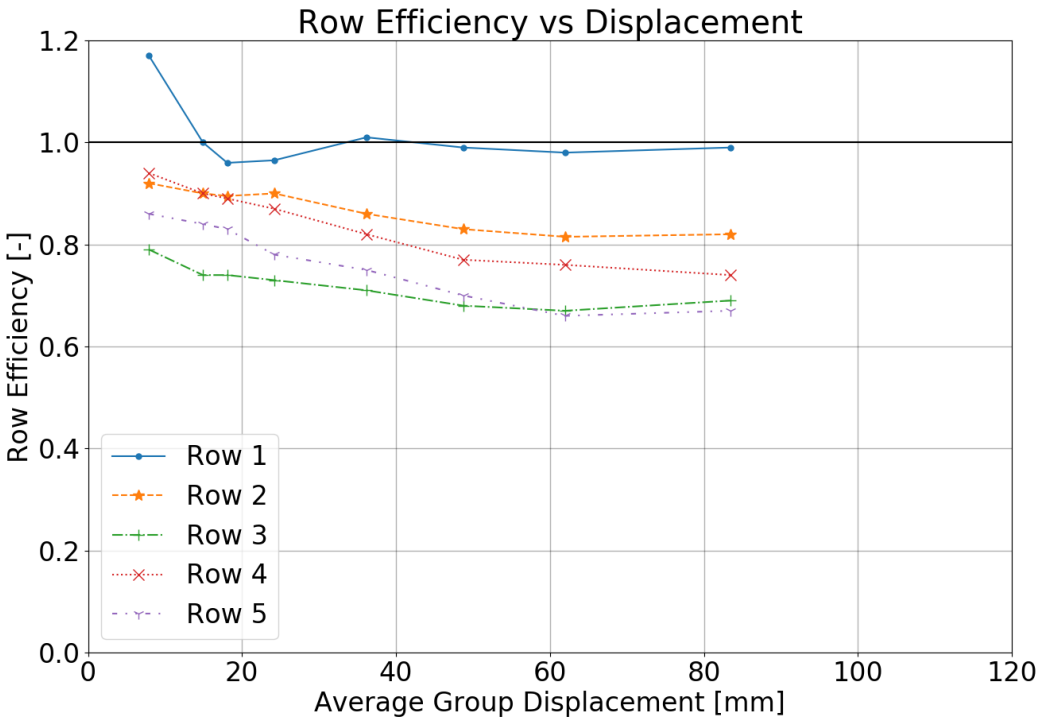

Figure A.9: Efficiency per row as function of average group displacement, Salt Lake City case

Figure A.9 shows the efficiencies of each row. As stated earlier, the 1st row carries the most load. Remarkable however is how, as the first target deflection, the row efficiency is higher than 1. This means the front piles are carrying on average more load than they would individually. Row efficiencies larger than 1 are possible, but for design purposes are capped at 1.

The figure also shows how the trailing row carries less load than the leading row, as well as centre rows 2 and 4. Again, row 3 carries on average the least, which the author claimed to be likely due to local soil variations.

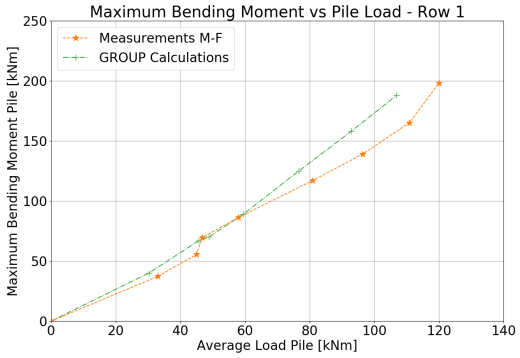

(a) Maximum bending moment versus average pile load, row 1

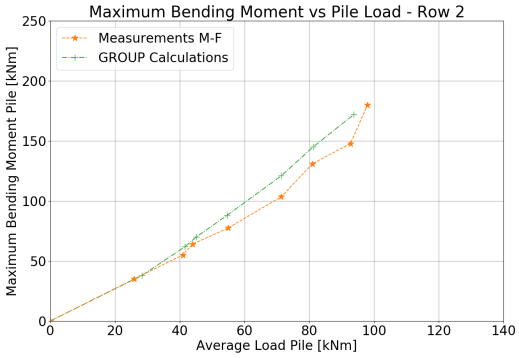

(b) Maximum bending moment versus average pile load, row 2

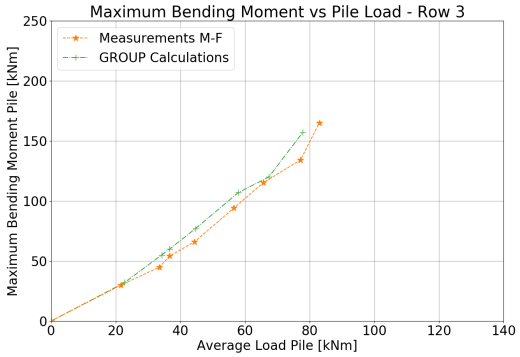

(c) Maximum bending moment versus average pile load, row 3

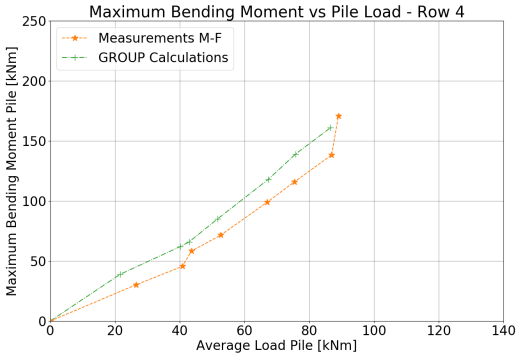

(d) Maximum bending moment versus average pile load, row 4

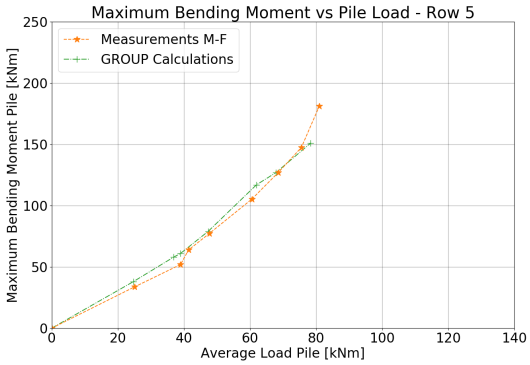

(e) Maximum bending moment versus average pile load, row 5

Figure A.10: Moment-load curve averaged per pile row, field measurements and GROUP calculations from Salt Lake City case

Figures A.10a through A.10e show the maximum bending moment per pile row. The measurements do not provide a smooth curve. As stated earlier, several strain gauges were damaged prior or during testing. Furthermore, strain gauges were placed at intervals of 0.6 m, meaning it is possible the maximum bending moment could lie in between measuring points. These are possible causes for the kinks in these graphs. As the results

A.3. P-y curve modelling Salt Lake City case

The Salt Lake City case has been recreated using P-y curve based software for two reasons. First of, it is used to compare results of the original report and the Embedded Beam Row model. Secondly, the EBR requires an input for the lateral resistance of the pile as function of depth. For this case, it has been decided to calculate the lateral resistance using P-y method. The field tests that were performed can be considered as undrained loading concerning the soft soils, making the P-y curve method applicable for this case.

A.3.1. Single pile modelling

For the modelling of the test of the single pile, the software PyPile, created by Yong Technology Inc., has been used. The software allows for multiple layers to be used and provides multiple different P-y curves (Yong Technology Inc., 2020). PyPile uses the Finite Element Method for modelling. The input for PyPile is similar to that of LPile. Hence, the same soil and pile parameters have been introduced as input as defined in Tables A.1 and A.2. The following analysis settings have been used:

Parameter	Value	Unit
Number of elements	100	–
Max. number of iterations	500	–
Convergence tolerance on deflection	1E-06	*m*
Deflection limit	1.00	*m*

Table A.4: Analysis settings PyPile single pile Salt Lake City Case

The results of the PyPile calculations are presented in the following figures, together with the field measurements and the LPile calculations.

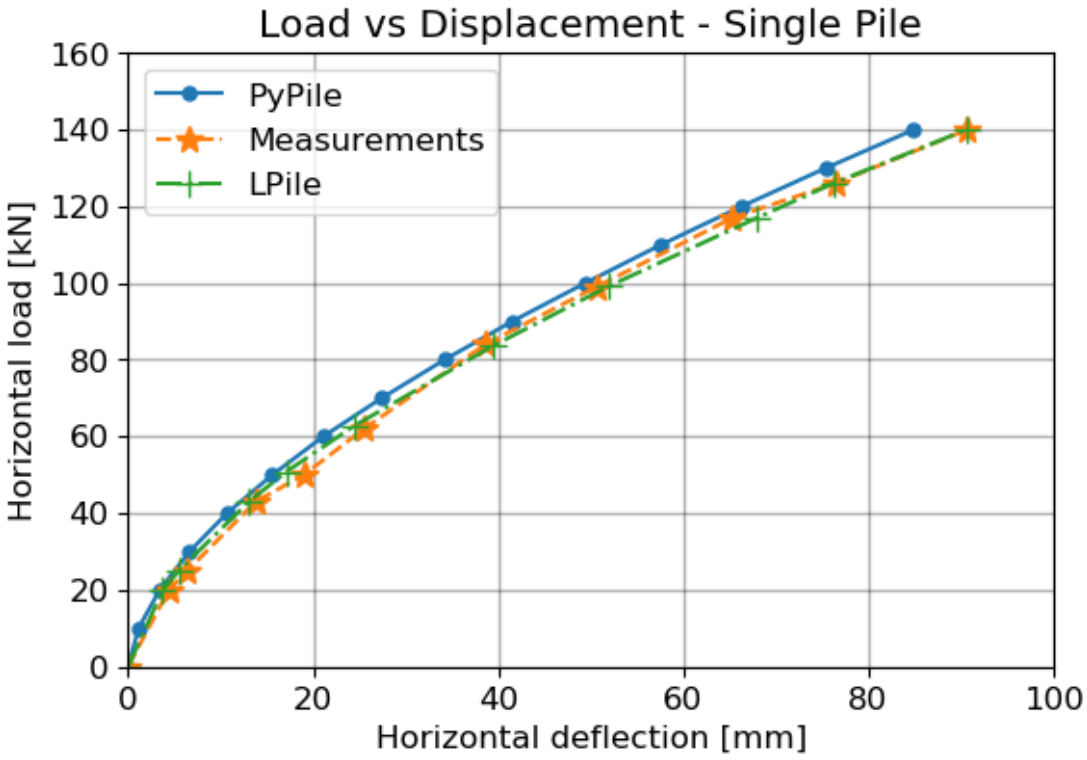

Figure A.11: Force-displacement curve PyPile, compared to field measurement and LPile calculations, Salt Lake City case

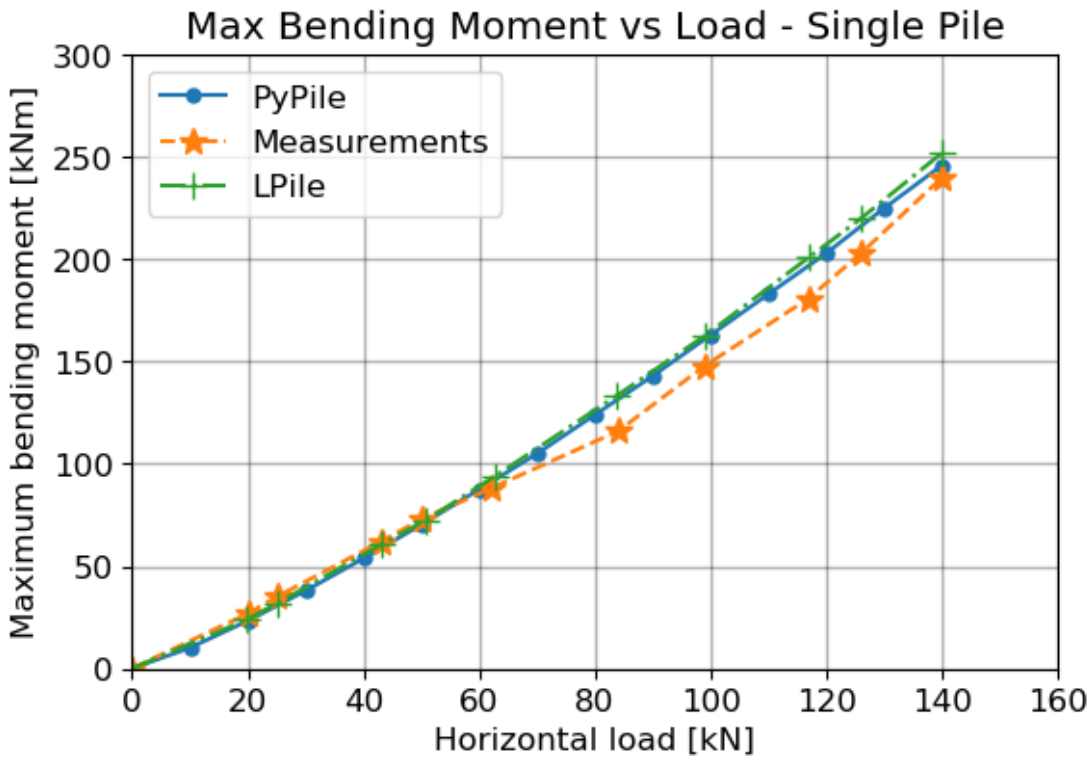

Figure A.12: Moment-force curve PyPile, compared to field measurement and LPile calculations, Salt Lake City case

As can be seen in Figure A.11, the force-displacement curve calculated using PyPile is almost exact to the one obtained from the field measurements or LPile. The PyPile curve shows less deflection for the same force compared to the other two curves. A possible explanation is the fact that PyPile does not take into account the additional pile above the point of load application. In PyPile, the pile stops at the point of load application, which is 0.495 above surface level. However, in reality, the pile continues to 2.13 m above the surface level. In the tests, this section of the pile creates a second order moment, increasing deflection. This could be taken into account by applying a moment in the PyPile software, based on the displacement. Nevertheless, the differences in deflection are within 5%.

A.4. Plaxis 2D model pile group loading Salt Lake City case

A.4.1. Plaxis 2D model input

A portion of the data used in the Plaxis 2D model has been obtained from the original report by Snyder (2004). However, some data was derived via relations, and some data was not available at all and had to be estimated. This is one possible cause for any differences in the output compared to the field measurements.

Soil parameters

For the modelling of the soil, the Hardening Soil small strain stiffness model has been used, similar as to what will be used for the Herengracht case. An overview of the parameters is presented in the following table:

Layer	**1**	**2**	**3**	**4**	**5**	**6**	**7**	**8**	
Parameter									**Unit**
Drainage type	Undr. (B)	Undr. (B)	Undr. (B)	Drained	Undr. (B)	Undr. (B)	Undr. (B)	Drained	–
γ_{sat}	19.05	19.05	19.05	18.14	19.05	19.05	19.05	18.14	kN/m^3
e_0	0.5	0.5	0.5	0.5	0.5	0.5	0.5	0.5	–
φ'	25.0	25.0	25.0	38.0	25.0	25.0	25.0	33.0	°
c'	N.A.	N.A.	N.A.	0.00	N.A.	N.A.	N.A.	0.00	kPa
s_u	41.4	60.0	40.0	N.A.	56.9	25.0	54.0	N.A.	kPa
ψ	0.00	0.00	0.00	8.00	0.00	0.00	0.00	3.00	°
ν_{ur}	0.15	0.15	0.15	0.20	0.15	0.15	0.15	0.2	–
m	0.7	0.8	0.7	0.5	0.7	0.7	0.7	0.5	–
E_{50}^{ref}	4.97	7.20	4.80	75.0	5.69	1.67	5.40	60.0	MPa
E_{oed}^{ref}	5.25	7.60	5.07	83.3	6.01	1.76	5.70	66.7	MPa
E_{ur}^{ref}	14.9	21.6	14.4	225	17.1	5.00	16.2	180.	MPa
G_0	5.4	7.83	5.22	93.8	7.42	2.17	7.04	75.0	MPa
$\gamma_{0.7}$	1.50E-4	1.50E-4	1.50E-4	1.59E-4	1.50E-4	1.50E-4	1.50E-4	1.97E-4	–
OCR_{centre}	2.68	2.48	2.30	2.04	1.82	1.72	1.61	1.02	–
K_0	0.876	0.847	0.821	0.597	0.744	0.726	0.706	0.460	–

Table A.5: HSsmall properties per layer, with reference pressure p_ref = 100 kPa, with layers defined as:
1: Sandy lean clay
2: Lean clay
3: Sandy silt
4: Silty sand
5: Sandy silt
6: Sandy silt
7: Sandy silt
8: Poorly graded sand.
All other parameters have been left to the default Plaxis setting

Unit weights and initial void ratio

The effective unit weights have been determined within the report itself. No initial void ratio data was found, thus the default value of 0.5 suggested by Plaxis has been used.

Shear strength and dilatency parameters

For the cohesive soil, Undrained Unconsolidated triaxial tests had been performed, as well as literature study to previous tests carried out on site. Based on this, undrained shear strengths had been determined. Table A.5 also shows friction angles for the cohesive soils. These have been estimated based on the Herengracht case and are only used to determine K_0. For the cohesionless soils, it is unclear how the shear strength parameters were determined.

It has been assumed the dilatency angle for the cohesive soils is equal to 0. For the cohesionless soils, the following relation has been used:

$$\psi \approx \varphi' - 30° <= 0 \tag{A.1}$$

Elasticity parameters
No data was available for the Poisson's values or the stress-dependency factor. Hence, these values have been estimated.

For the cohesive soils, the E_{50} has been determined based on the undrained shear strength and the strain at 50% mobilisation:

$$E_{50} = \frac{s_u}{\varepsilon_{50}} \tag{A.2}$$

With:
- E_{50}: elastic modulus at 50% mobilisation for primary loading [kPa]
- s_u: undrained shear strength [kPa]
- ε_{50}: vertical strain at 50% mobilisation [-]

From this value, the oedometer and unloading-reloading moduli E_{oed}^{ref} and E_{ur}^{ref} were calculated as follows (Alpan, 1970):

$$\begin{aligned} E_{oed}^{ref} &= \frac{(1-\nu)\, E_{50}^{ref}}{(1+\nu)\,(1-2\nu)} \\ E_{ur}^{ref} &\approx E_{50}^{ref} \end{aligned} \tag{A.3}$$

It was unclear how the values for ε_{50} has been obtained. After testing, the E-moduli of the top three layers had been increased with 20 %, which provided a better response of the Plaxis model. It also became clear how much influence this parameter had, as displacements decreased with approximately 25 % under the same load.

For the cohesionless soils, the E_{50} has been based on CPT results in combination with the indicative soil properties as provided by Eurocode 7 NEN-EN9997.
Shear stiffness parameters
The initial shear modulus G_0 have been calculated using elasticity theory (Wichtmann and Triantafyllidis, 2009):

$$G_0 = \frac{E_0}{2\,(1+\nu)} \tag{A.4}$$

For the threshold shear strain, the relation as described by Kelder (2015) has been used:

$$\gamma_{0.7} \approx \frac{1}{9G_0}\left[2c'\left(1+cos\left(2\varphi'\right)\right)+\sigma_1'\,(1+k_0)\,sin\left(2\varphi'\right)\right] \tag{A.5}$$

However, this relation includes several parameters that, for the cohesive layers, have been estimated themselves. Hence, it has been decided to use a value of 1.50E-4 for all cohesive layers. The equation above has thus only been used for the cohesionless layers.

OCR and K_0
The OCR had been determined using oedometer tests. From these tests, the author provided a linear relation for the OCR. At the excavated surface level m, an OCR of 2.8 was determined, at 8.3 m depth an OCR of 1.2. The OCR in the centre of each layer has been determined from this linear relationship.

The value for K_0 has been calculated by hand using the following relation (Mayne and Kulhawy, 1982):

$$K_0 = (1 - sin(\varphi')) * OCR^{sin(\varphi')} \tag{A.6}$$

Embedded Beam Row properties

For the modelling of the pile row, the Embedded Beam Row has been used. The following material properties have been used:

Parameter	Value	Unit
Material Type	Elastic	–
E	200	GPa
γ	0	kN/m^3
Beam type	User-defined	–
A	9.40E-03	m^2
I	1.25E-4	m^4
$L_{spacing}$	1.07	m
Rayleigh α	0.00	–
Rayleighβ	0.00	–
Axial skin resistance	Linear	–
$T_{skin,start,max}$	10.0	kN/m
$T_{skin,end,max}$	10.0	kN/m
Lateral resistance	Multi-linear	–
F_{max}	100	kN
Axial stiffness factor	10.0	–
Lateral stiffness factor	10.0	–
Base stiffness factor	10.0	–

Table A.6: Plaxis Embedded Beam Row properties Salt Lake City case

The lateral resistance of the Embedded Beam Row has been determined using PyPile. This has been done by imposing a displacement of 100 mm and calculating the corresponding horizontal pressure. This has been done under the assumption that the soil had reached its ultimate limit state. This has been checked by also calculating the earth pressure at a displacement of 50 mm. As can be seen in Figure A.13, this assumption holds for the current situation, as there is little to no difference in both graphs. The self-weight of the piles has been deemed to be of negligible influence

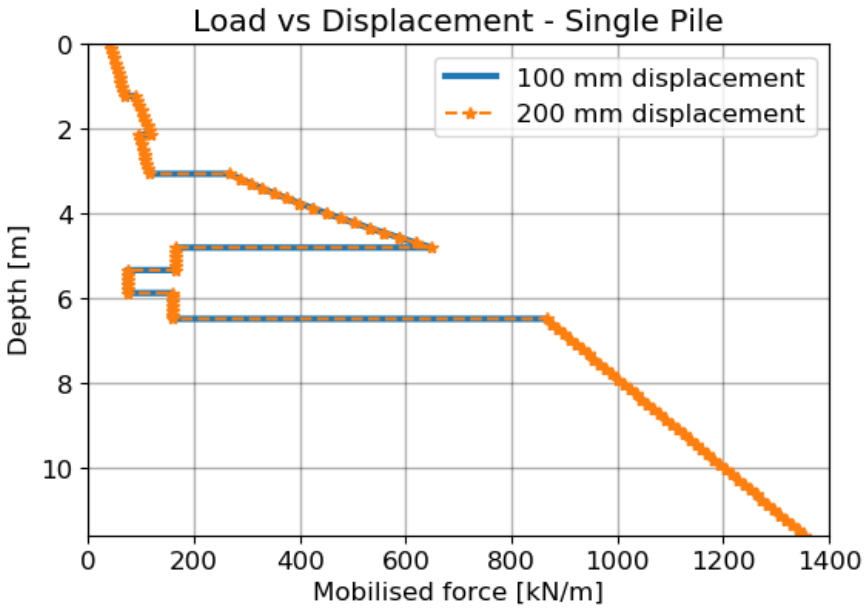

Figure A.13: Ultimate soil resistance based on P-y calculations from PyPile, Salt Lake City case

Frame properties

In the original report, the frame connecting the piles was considered to be infinitely stiff, with no further information provided. Based on Figure A.5, Page 76, it had been assumed the beams were similar to IPE400. The self-weight of the frame has been neglected. As such, the following parameters have been used:

Parameter	**Value**	**Unit**
Material Type	Elastic	–
Isotropic	True	–
E	210	GPa
EA_1	1.11E+06	kN/m
EI	1.51E+03	km^2/m
w	0.00	$kN/m/m$
ν	0.00	–
Rayleigh α	0.00	–
Rayleigh β	0.00	–
Prevent punching	False	–

Table A.7: Plaxis plate-frame properties Salt Lake City case

Modelling input

The Plaxis model created can be seen in Figure A.14. In here, the load is applied on the top right corner, at x=0 m, into the right direction. A top layer of 0.30 m was created with identical properties to Layer 1: Sandy lean clay, but was given a tensile strength of 1 kPa. This was done due to numerical issues that would arise otherwise, in which the top layer would become plastic in the initial phase.

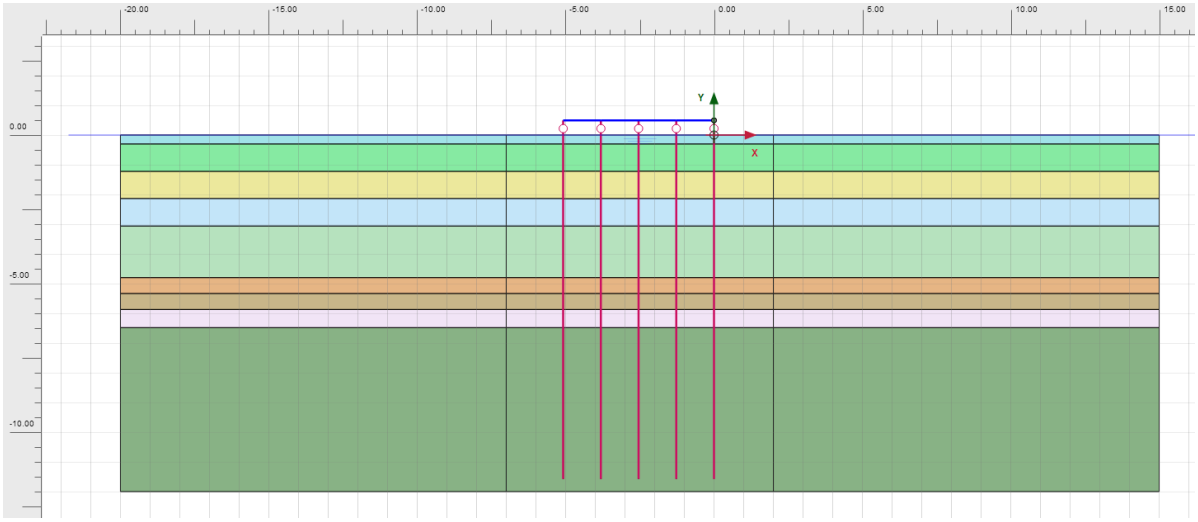

Figure A.14: Plaxis model Salt Lake City case

For the simulation, force-based loading method was used, as the overall behaviour shows softening. The force to be applied is equal to:

$$F_{Plaxis} = \frac{F_{Total}}{n_{piles,perpendicular} * L_{spacing,perpendicular}} \tag{A.7}$$

With:

- F_{Plaxis}: Force to be applied in Plaxis 2D [kN/m]
- F_{Total}: Total load applied on pile group [kN]
- $n_{piles,perpendicular}$: number of piles perpendicular to loading direction [-]
- $L_{spacing,perpendicular}$: c.t.c. pile spacing perpendicular to loading direction [m]

Hence, the following loading steps have been applied:

Phase	$\mathbf{F}_{Plaxis}$ $[kN/m]$
1	123
2	185
3	200
4	240
5	314
6	360
7	433
8	487

Table A.8: Applied loads Plaxis 2D model Salt Lake City case

For the analysis, the following settings have been used:

Parameter	**Value**
General	
Calculation type	Plastic
Loading type	Staged construction
$\sum M_{stage}$	1.00
$\sum M_{weight}$	1.00
Pore pressure calculation type	Use pressures from previous phase
Thermal calculation type	Ignore temperature
Time interval	0.00 day
Deformation control parameters	
Ignore undr. behaviour	False
Reset displacements to zero	False / Phase 1: True
Reset small strains	False / Phase 1: True
Reset state variables	False
Reset time	False
Updated mesh	True
Updated water pressure	True
Ignore suction	True
Cavitation cut-off	True
Cavitation stress	100 kN/m^2
Numerical control parameters	
Max cores to use	256
Max numbers of steps stored	1
Use default iter parameters	True

Table A.9: Deformation and numerical control parameters Plaxis 2D model Salt Lake City case

The mesh generation options was set to a "Very fine" element distribution for the final simulation, using enhanced mesh refinements. Some areas were marked to use a more coarse or fine mesh, as illustrated in Figure A.15. The resulting mesh is presented in Figure A.16.

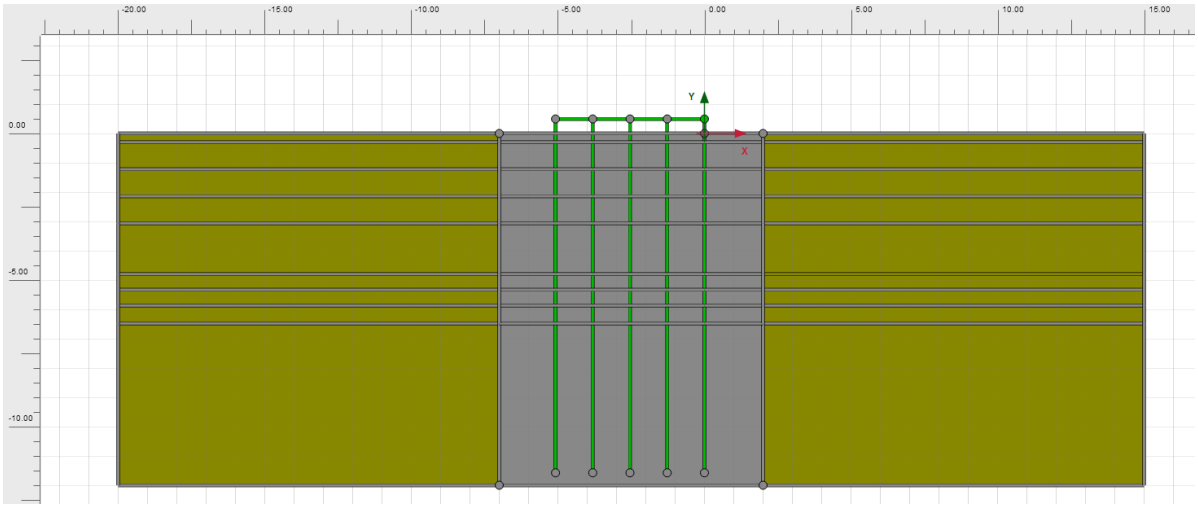

Figure A.15: Plaxis mesh settings Salt Lake City case

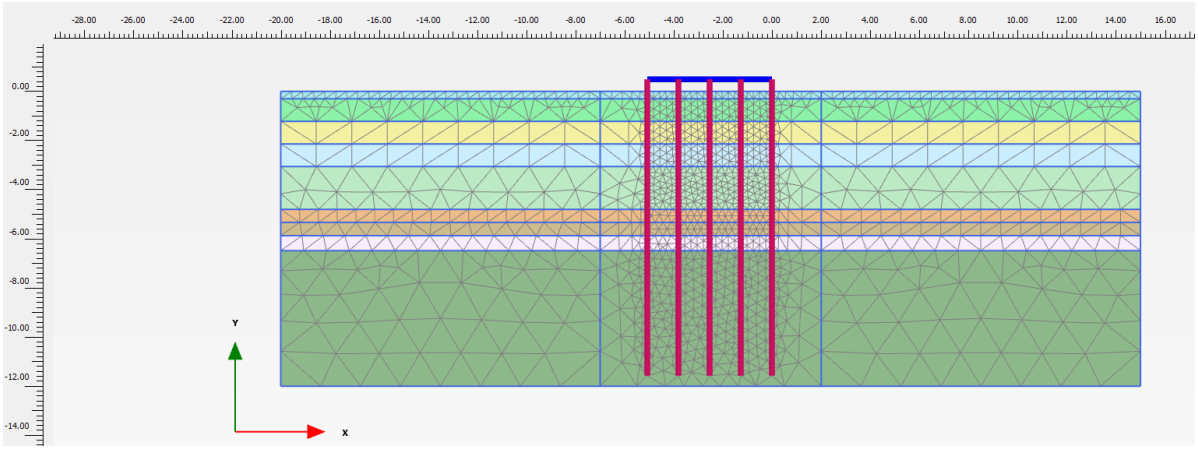

Figure A.16: Plaxis mesh Salt Lake City case

A.4.2. Results Plaxis 2D modelling

The results of the Plaxis 2D model have been plotted in the following figures.

Force-displacement

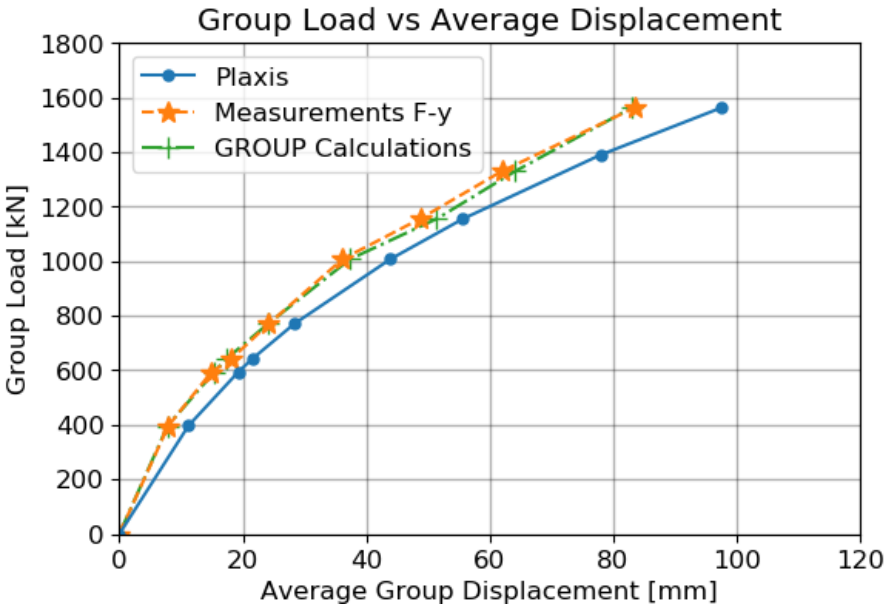

Figure A.17: Load-displacement curve pile group, from Plaxis modelling and compared to measurements and GROUP calculations Salt Lake City case

Figure A.17 shows that the Plaxis model results in a less stiff response compared to the field measurements. At the first measurement point around 400 kN, the Plaxis model predicted displacements 40 % larger than was measured. For higher loads, in this case from 600 kN and onward, Plaxis over-estimates the displacements with an average 20 %. The initially larger difference in stiffness is most likely due to installation effects. With driven piles, the surrounding soil is compressed during installation, increasing the initial resistance during lateral loading. At larger deflections, the share of these installation effects on the total resistance decreases. With increasing deflection, soil further away from the pile is mobilised in order to provide passive resistance. The further away the soil that is mobilised, the less influence this soil has undergone from the installation. As of the time of writing, it is not able to model the installation effects of driven piles using the Embedded Beam Row of Plaxis 2D (Bentley Systems, 2014).

A second possible explanation for why the Plaxis model provides a less stiff response it the question whether the Salt Lake City case is a truly 2-dimensional. The tests consisted of 3 pile rows perpendicular to the plane of loading. Of the three out-of-plane rows, two were side rows. For side rows, the resistance is higher than centre rows. This is because the edge effect, or sideways overlapping of passive soil wedges, only occurs from one side instead of two, thus leaving more resistance. However, the Embedded Beam Row assumes that there are an infinite number of piles rows perpendicular to the plane of loading.

Furthermore, as stated earlier, there is uncertainty in the E-moduli used for the model. The moduli for the cohesive soils have been derived from data in the original report, of which the source is unclear. Subsequently, the moduli of the cohesionless soils have been determined using relations involving CPTs.

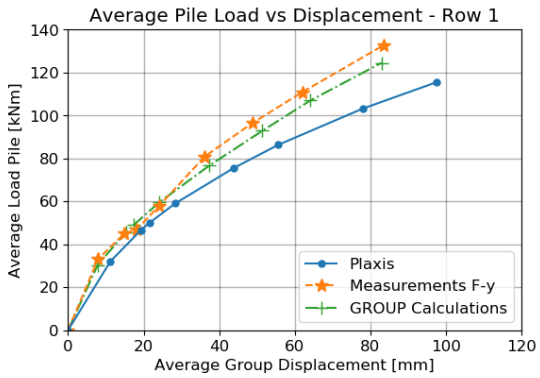

(a) Average pile load versus group displacement, row 1

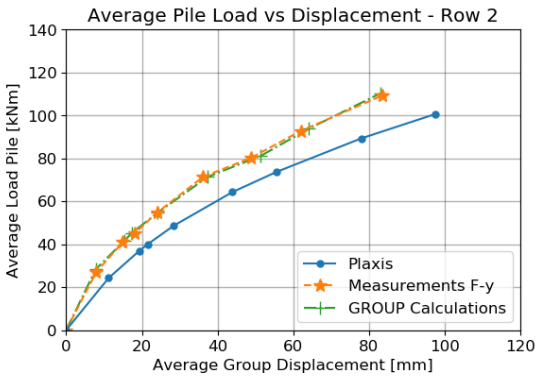

(b) Average pile load versus group displacement, row 2

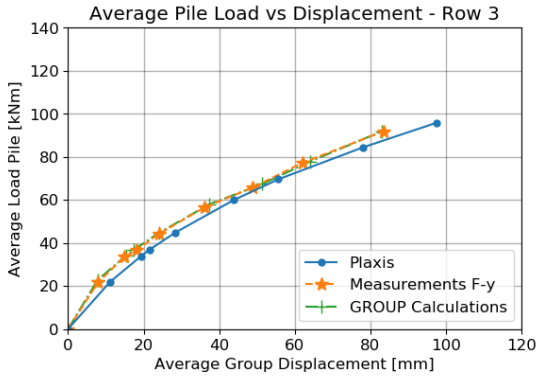

(c) Average pile load versus group displacement, row 3

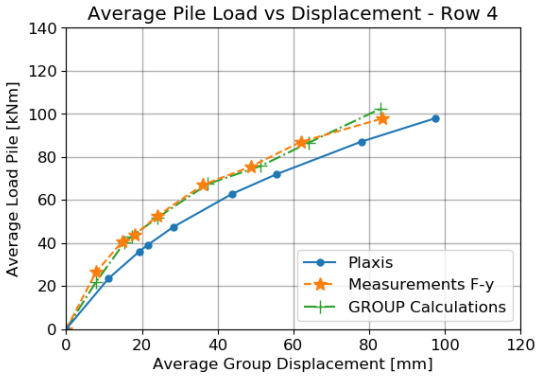

(d) Average pile load versus group displacement, row 4

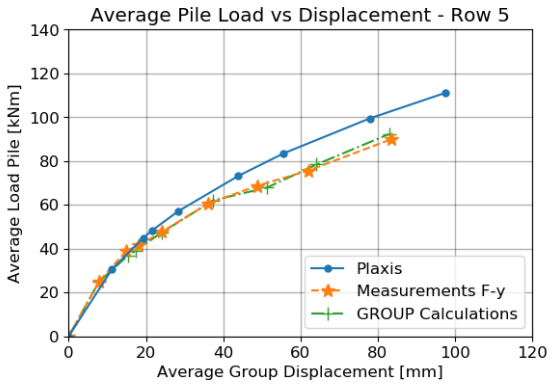

(e) Average pile load versus group displacement, row 5

Figure A.18: Load-displacement curve averaged per pile row, from Plaxis modelling and compared to measurements and GROUP calculations Salt Lake City case

Figures A.18a through A.18e show the force-displacement curves per pile row. From the force-displacement curve it had already been observed the total group behaviour was less stiff compared to the measurements and GROUP calculations. In most cases, the Plaxis curve lies below the other two curves. However, for the trailing row, or the fifth row, Plaxis predicted a higher pile load given the same displacement.

Efficiencies

In Figure A.19, the group efficiencies of the Plaxis modelling as well as the measurements have been presented. Again, the group efficiency is defined as the total load applied on the group, divided by the load a single pile would carry multiplied by the total number of piles, both systems undergoing the same displacement. The efficiencies of the Plaxis model have been based on the PyPile model discussed in Section A.3, Page 85. The efficiencies of the measurements had been presented in the original case report.

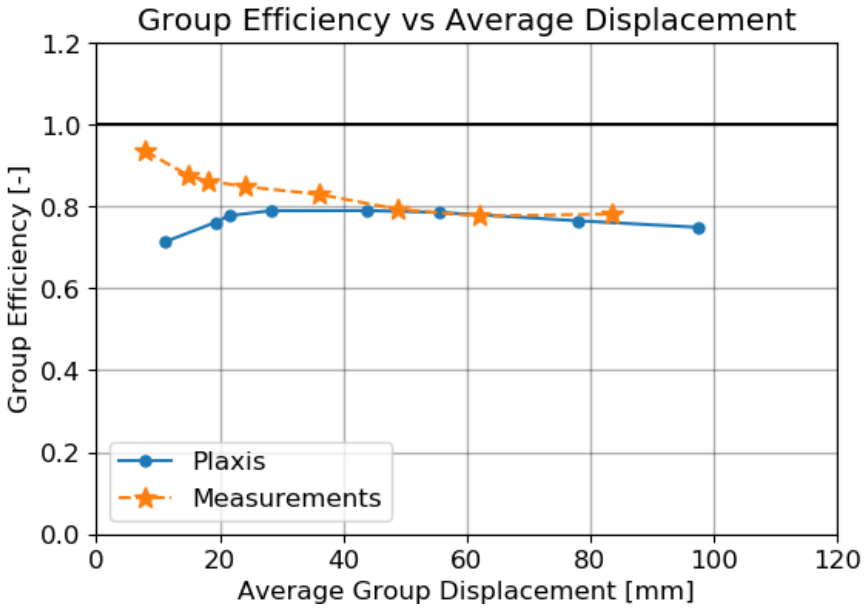

Figure A.19: Group efficiency as function of displacement, from Plaxis modelling and compared to measurements of Salt Lake City case

For displacements smaller than 38 mm, it can be observed that the efficiency of the Plaxis model is below the measurements. For larger displacements, the efficiencies of the model and the measurements roughly align. This sort of transition was also found in the force-displacement results in the previous section. In there, an initially large difference was found between the measurements and the Plaxis model, which reduced with increasing displacement. With increasing loads, the Plaxis results start to approach the measurements. As was stated then, the initial difference in behaviour is likely due to the lack of inclusion of installation effects in the model.
Figures A.20a and A.20b show a side by side comparison of the row efficiencies obtained from the measurements and Plaxis model. As was seen in Figure A.19, the efficiency of the Plaxis model starts low. In Figure A.20b, it can be seen all rows have an initially low efficiency. Once more, this is likely due to the exclusion of installation effects in Plaxis 2D.

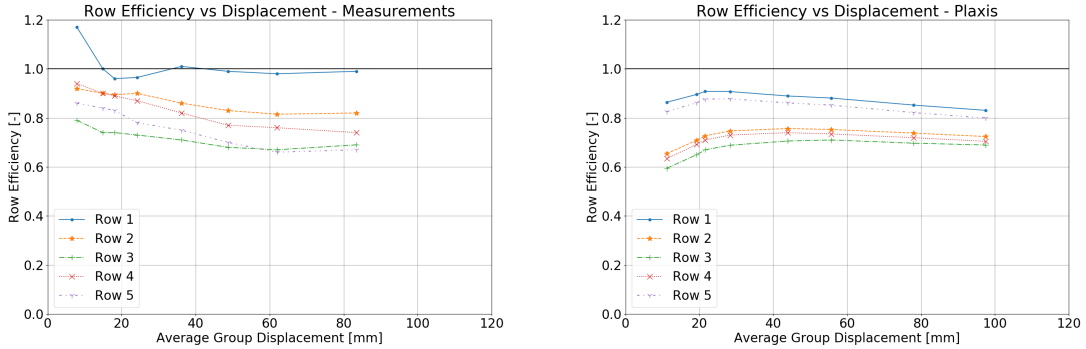

(a) Row efficiency as function of displacement, measurements Salt Lake City case

(b) Row efficiency as function of displacement, Plaxis results

Figure A.20

Both the measurements as well as the model results show that row 3 has a lower efficiency compared to the other centre rows, row 2 and 4. The original author attributed this problem to local soil differences. However, the Plaxis model assumed homogeneous soil conditions in the horizontal plane. Thus, it can be realistic that the third row exhibited less efficient behaviour compared to the other centre rows. However, it can still be

possible local soil variations were present, as row 3 was the only centre row that provided higher efficiency in the Plaxis model compared to the measurements, as can be seen in Figure A.21

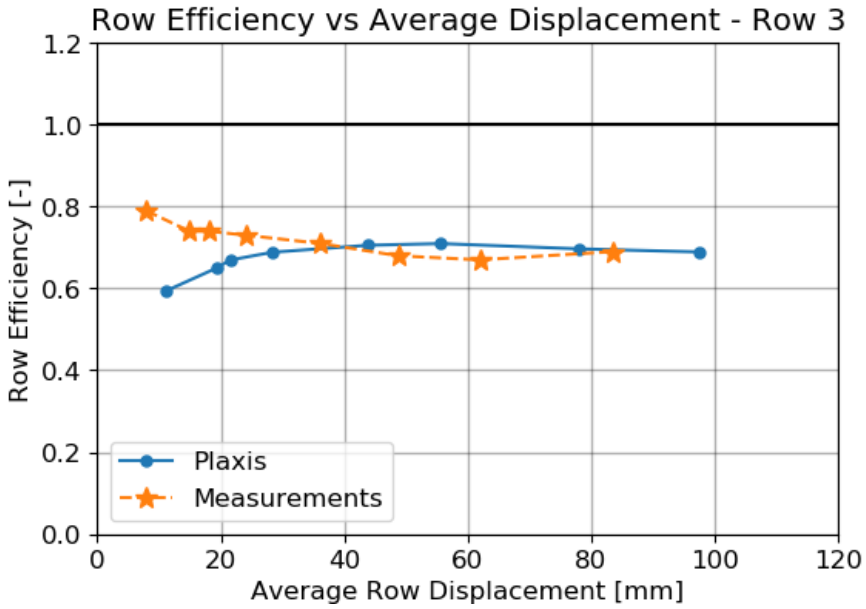

Figure A.21: Row efficiency as function of displacement, row 3, from Plaxis modelling and compared to measurements of Salt Lake City case

Comparing the trailing row in Figures A.20a and A.20b shows that the trailing row shows a larger efficiency in the Plaxis model compared to the measurements, for all displacements. Similar to what had already been observed in Figure A.18e, Page 94, it seems the trailing row has a larger contribution to the total load bearing capacity relative to the centre rows 2 and 4. This is contrary to the measurements, which showed that the trailing row carried less load compared to these centre rows. As stated earlier, and can be seen in the overview provided by Lemnitzen et al. (2010), it can be uncertain whether the trailing row carries more or less than the centre row. As mentioned in Section A.1.2, Page 77, multiple pile group tests had been carried out at this site. As reported by Rollins et al. (2003), a 3x3 driven pile group had been tested at the same location. The resulting row efficiency as function of displacement can be found in Figure A.22. In this figure, it can be seen that the trailing row, or back row, has a higher proficiency compared to the centre row. It is thus unclear what the reason for the the discrepancy between the Plaxis model and the measurements is. It is possible the difference was caused by the modelling, or that the problem was on the side of the testing, for example a local variation in soil.

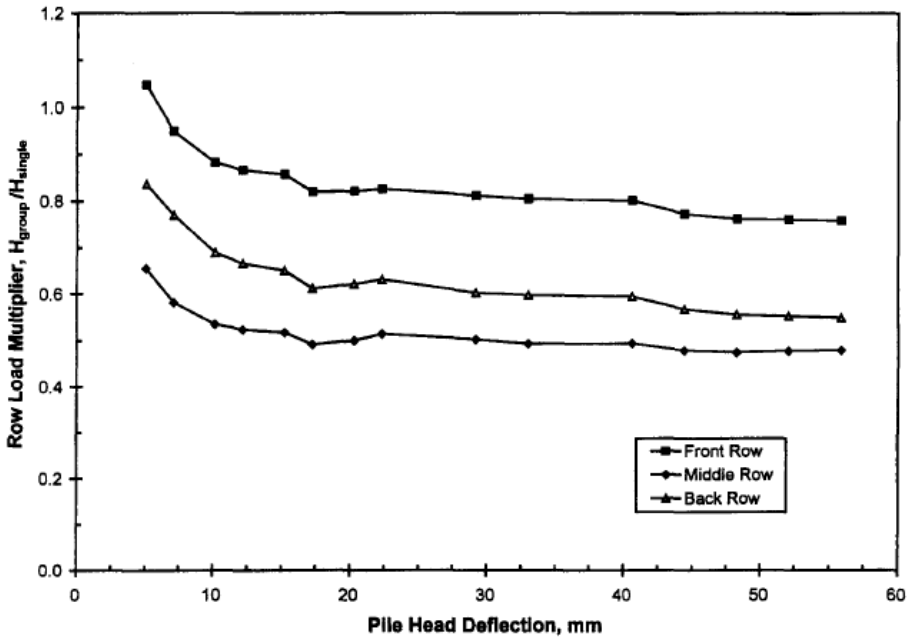

Figure A.22: Row efficiency as function of displacement, from a 3x3 driven pile group tested at the Salt Lake City site (Rollins et al., 2003)

Bending moments

Figures A.23a through A.23e show, per row, the average maximum bending moment as a function of the average pile load. It can be observed that in all cases, the Plaxis model underestimates the maximum occurring bending moment. However, the difference in maximum bending moment varies per pile row. For rows 1, 2 and 4 the Plaxis model predicts maximum bending moments 15 to 25 % lower than was measured. For row 3, a maximum difference of the Plaxis result compared to the measurement of 30% appears at certain loads. For the trailing row, the Plaxis result can be up to almost 50% lower than what had been measured. The results for rows 1, 2 and 4 are similar to those reported by Sluis et al. (2013). Their results of a laterally loaded pile group in soft clay have been presented in Figure A.29. Here it can be seen that the maximum bending moment calculated using the 2D Embedded Beam Row is roughly 20 % lower than the one obtained using 3D volume elements.

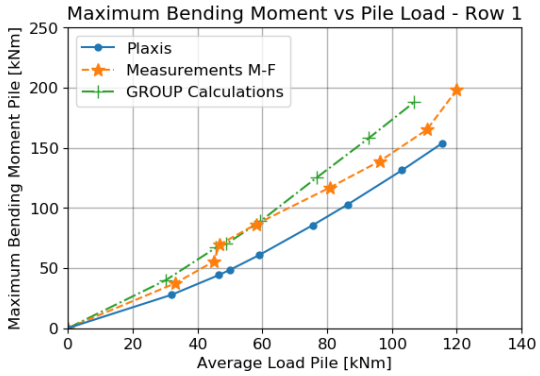

(a) Maximum bending moment versus average pile load, row 1

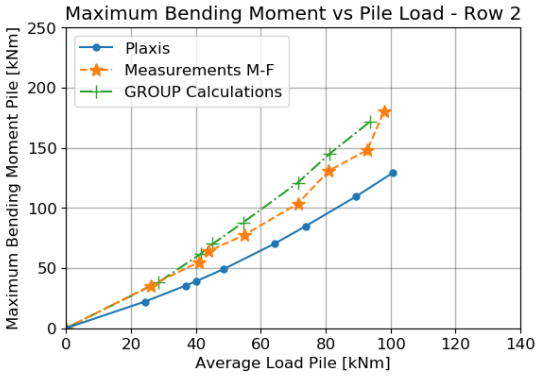

(b) Maximum bending moment versus average pile load, row 2

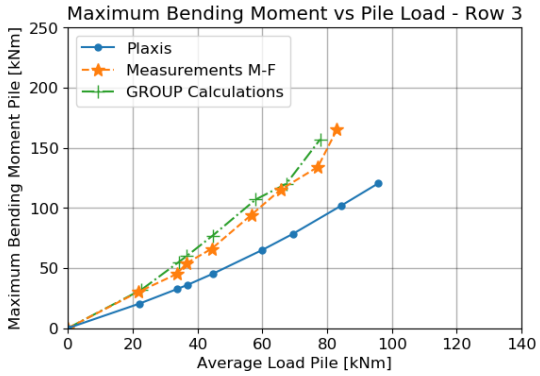

(c) Maximum bending moment versus average pile load, row 3

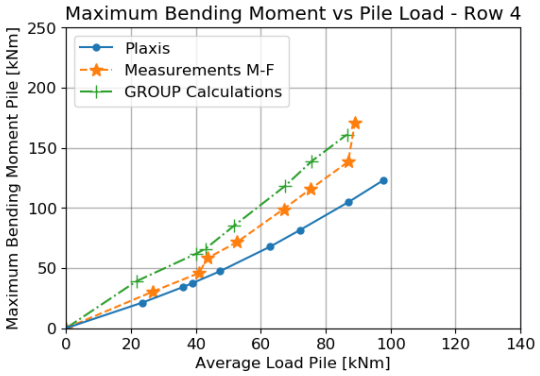

(d) Maximum bending moment versus average pile load, row 4

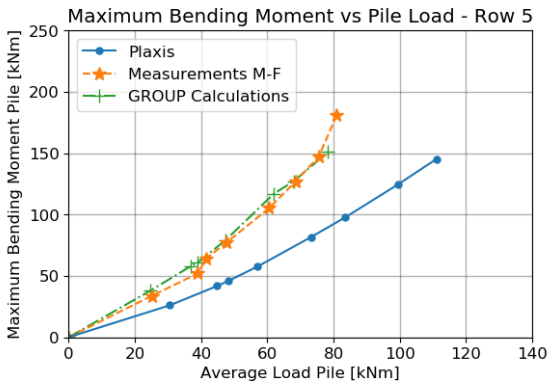

(e) Maximum bending moment versus average pile load, row 5

Figure A.23: Moment-load curve averaged per pile row, from Plaxis modelling and compared to field measurements and GROUP calculations Salt Lake City case

Figures A.24a through A.28b show the bending moment curve over the length of the pile per row, for both a group load of 770 kN and 1330 kN. The measurements have been plotted alongside the Plaxis results. Furthermore, the location of the maximum absolute value of bending moment has been marked. It has been chosen to plot the bending moments for 770 kN and 1330 kN group load, as the original author has chosen these two loads as well. The values for the measurements have been obtained from graphs in the original report. However, for lower bending moments, difficulties arose due to image quality. Hence, there is a possible error in bending moment values with an absolute value smaller than 3 kNm. This area has been marked in red.

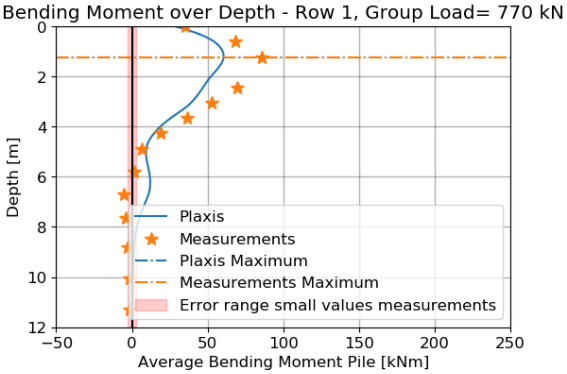

(a) Bending moment over depth, row 1, Plaxis results compared to measurements, row 1, group load = 770 kN

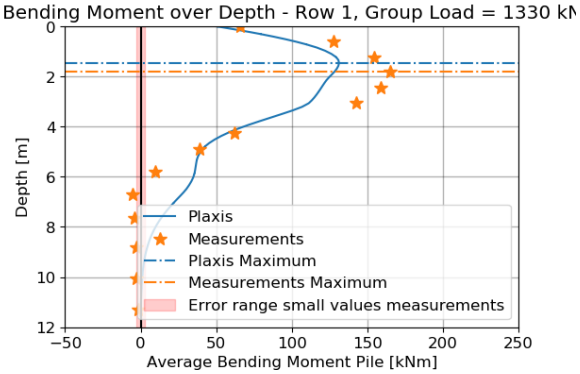

(b) Bending moment over depth, row 1, Plaxis results compared to measurements, row 1, group load = 1330 kN

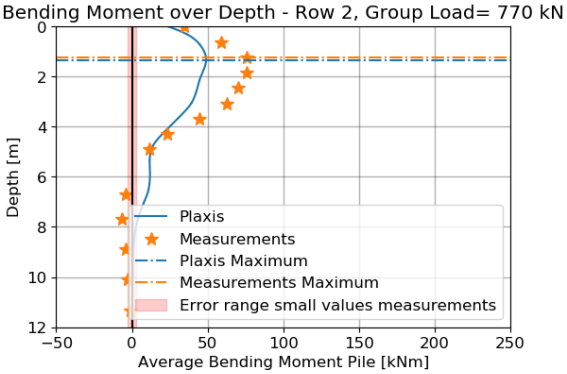

(a) Bending moment over depth, row 2, Plaxis results compared to measurements, row 2, group load = 770 kN

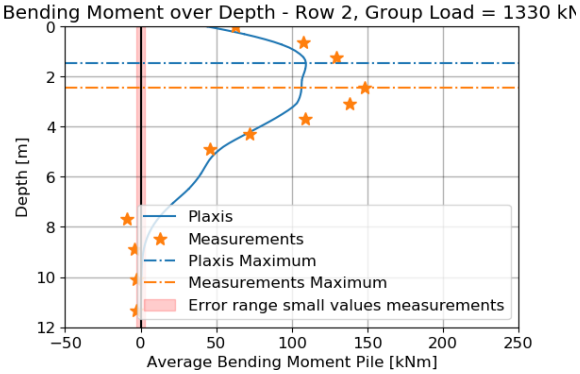

(b) Bending moment over depth, row 2, Plaxis results compared to measurements, row 2, group load = 1330 kN

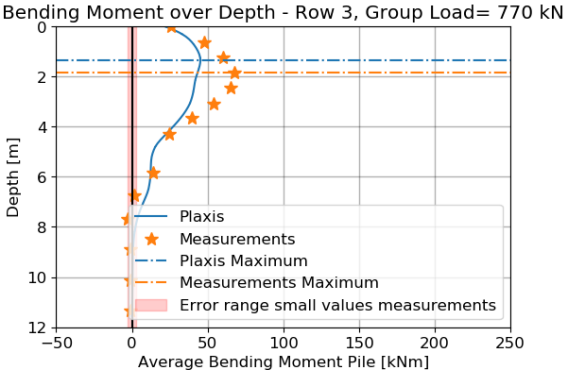

(a) Bending moment over depth, row 3, Plaxis results compared to measurements, row 3, group load = 770 kN

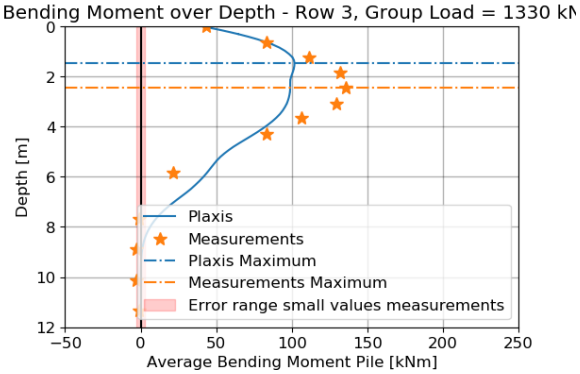

(b) Bending moment over depth, row 3, Plaxis results compared to measurements, row 3, group load = 1330 kN

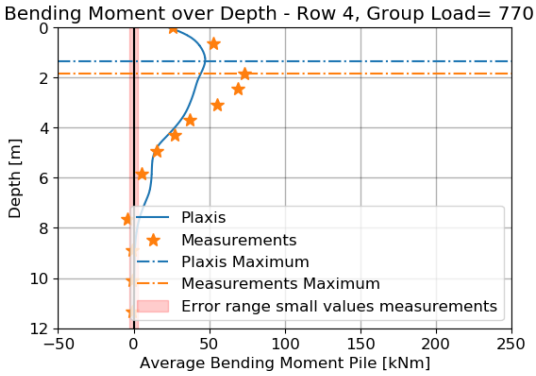

(a) Bending moment over depth, row 4, Plaxis results compared to measurements, row 4, group load = 770 kN

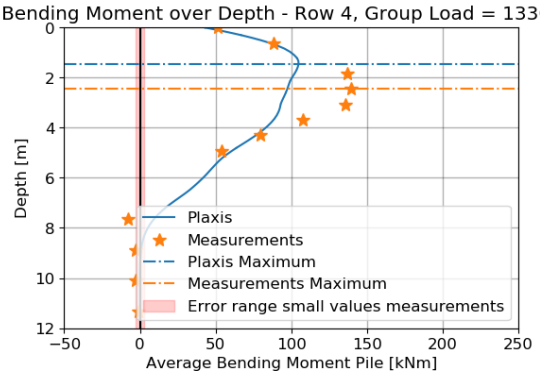

(b) Bending moment over depth, row 4, Plaxis results compared to measurements, row 4, group load = 1330 kN

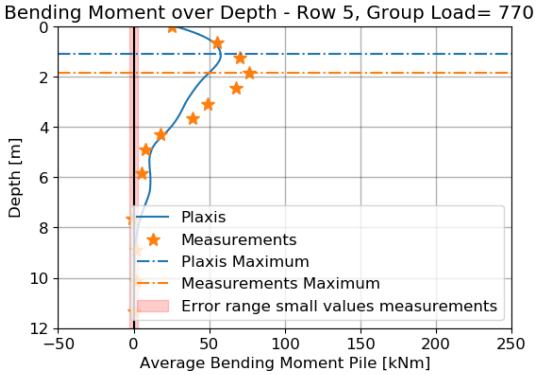

(a) Bending moment over depth, row 5, Plaxis results compared to measurements, row 5, group load = 770 kN

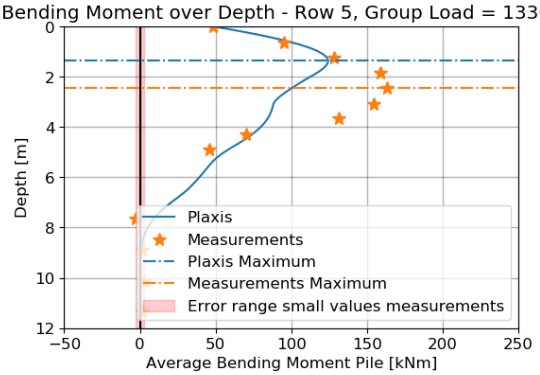

(b) Bending moment over depth, row 5, Plaxis results compared to measurements, row 5, group load = 1330 kN

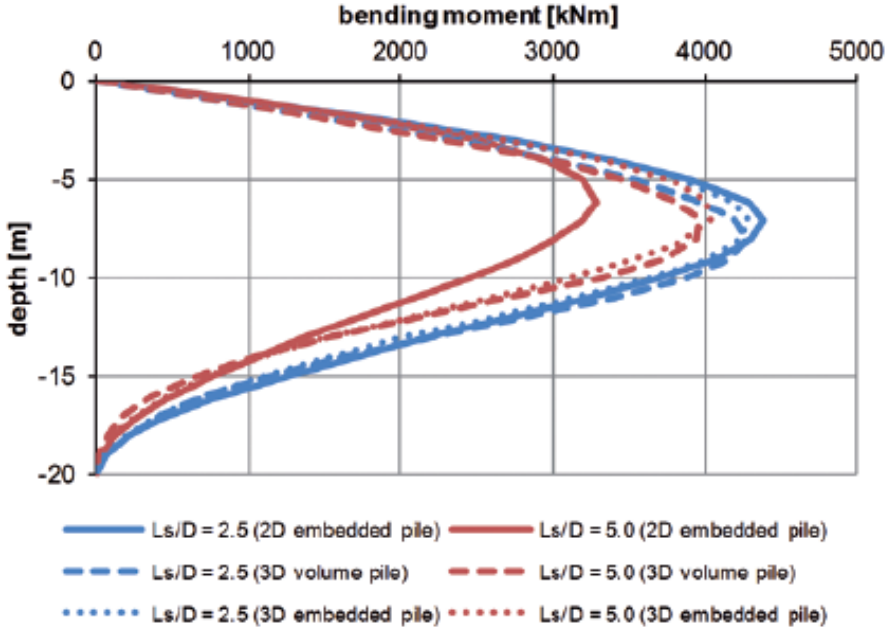

Figure A.29: Bending moment over depth for a laterally loaded pile in soft clay, $L_{spacing}$/D=5.0, using 2D Embedded Beam Row, 3D Embedded Beam and 3D volume elements, as reported by Sluis et al. (2013)

For the smaller group load of 770 kN, the Plaxis model predicted the depths of maximum within 0.6 m of what had been measured. For the first two rows, the depths of the model and the measurements coincided. The largest difference in depth occurred in row 5. For rows 3 through 5, the depth of maximum bending moment predicted by Plaxis was shallower than had been measured. For the larger group load of 1330 kN, the difference in depths increased. None of the depths calculated by Plaxis corresponded to those measured, and the maximum difference in depth had increased to approximately 1.0 m, once more for the trailing row.

The shape of the bending moment curve of the Embedded Beam Row appears similar to the one presented in Figure A.29, Page 100. In here, the Embedded Beam Row not only predicted lower bending moments, but also that the maximum value occurred at shallower depth.

B

Determination Dimensions Quay Wall

The quay wall has been schematised as follows:

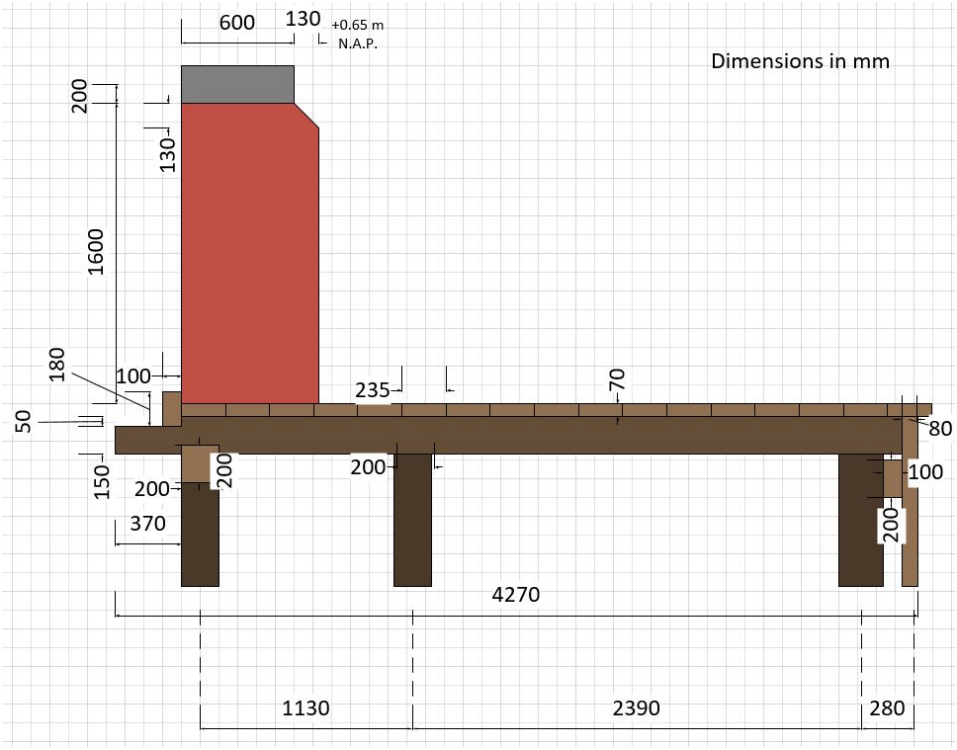

Figure B.1: Schematisation cross-section quay wall Herengracht, dimensions in mm

Element	Dimension	Value [mm]
Pile spacing	Row 1-2	1130
	Row 2-3	2370
	Longitudinal	1000
Pile	Diameter top	200
	Length	11 500
	Length embedded in first sand layer	500
Cross beam	Length	4180
	Width	250
	Height	200
Longitudinal beam	Width	200
	Height	200
Wall	Width bottom	730
	Height front	1800
Floor planks	Width	235
	Height	70
Screen	Thickness	80
	Length	4000

Table B.1: Main dimensions quay wall

No cross-sectional drawing of the Herengracht quay wall was available. Hence, a large portion of the dimensions of the quay wall have been obtained from an inspection performed near bridge 20 and 21 at the Herengracht (Ruiter, 2015). Another part has been based on a drawing from the Amsterdam Central Archive, see Figure B.2. This drawing gives a cross-sectional view of a different section of the Herengracht, approximately 500 m away. Even though it is the same canal, it does not mean the same dimensions can be used. The remainder of parameters have been estimated.

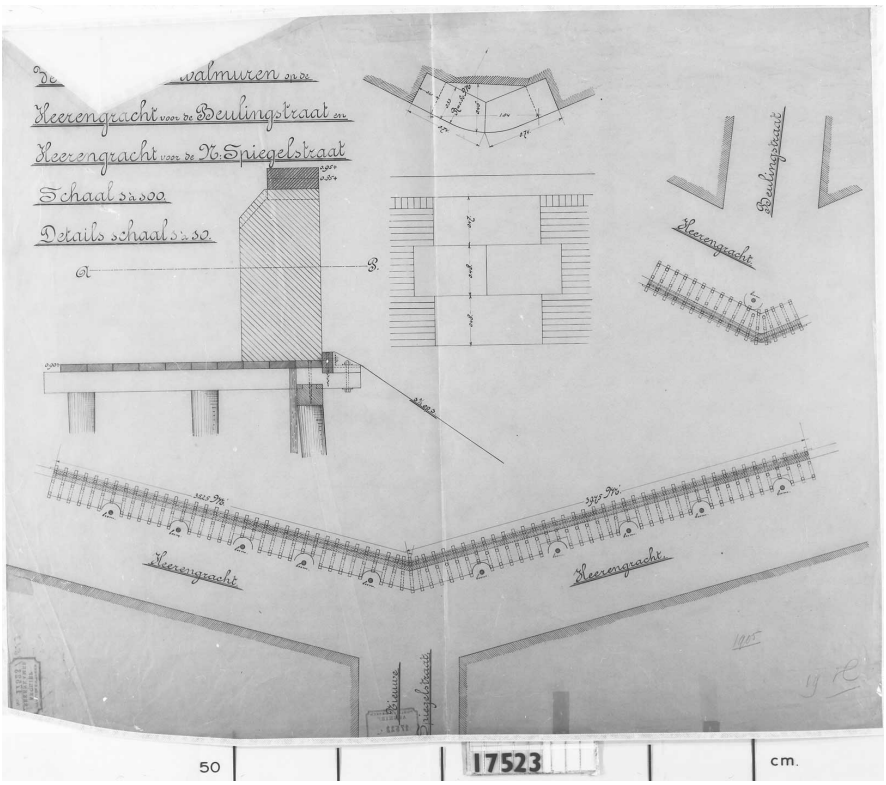

Figure B.2: Cross-section quay wall Herengracht at Beulingstraat, approx. 500 m away from case study (van de Dienst Openbare Werken; Centraal Tekeningen Archief, 1905)

The dive inspection could not find a third pile or rows or a screen within 3 metres from the front of the quay

wall. Hence, their position has been estimated.

C

Determination Soil Parameter Set Herengracht case

For the determination of the soil parameter set for the Herengracht case, several sources have been used. The main source of information consists are thee on-site drillings and corresponding lab classifications and triaxial tests (Dabek and van Geloven, 2019).

C.1. Soil profile

Three soil drillings were executed at the Herengracht. These drillings have been compared to other reports to check whether the classification of the soil was correct. Based on the drillings, the following soil profile has been determined:

Layer	**Elevation layer top [m NAP]**	**Elevation layer bottom [m NAP]**
1. Anthropogonic sand	+0.65	-2.00
2. Holland peat	-2.00	-5.00
3. Mudflat deposition - clayey	-5.00	-6.50
4. Mudflat deposition - sandy	-6.50	-10.0
5. Hydrobia clay	-10.0	-12.5
6. First sand layer	-12.5	N.A.

Table C.1: Soil profile Herengacht, Natural Surface Level at +0.65 m NAP

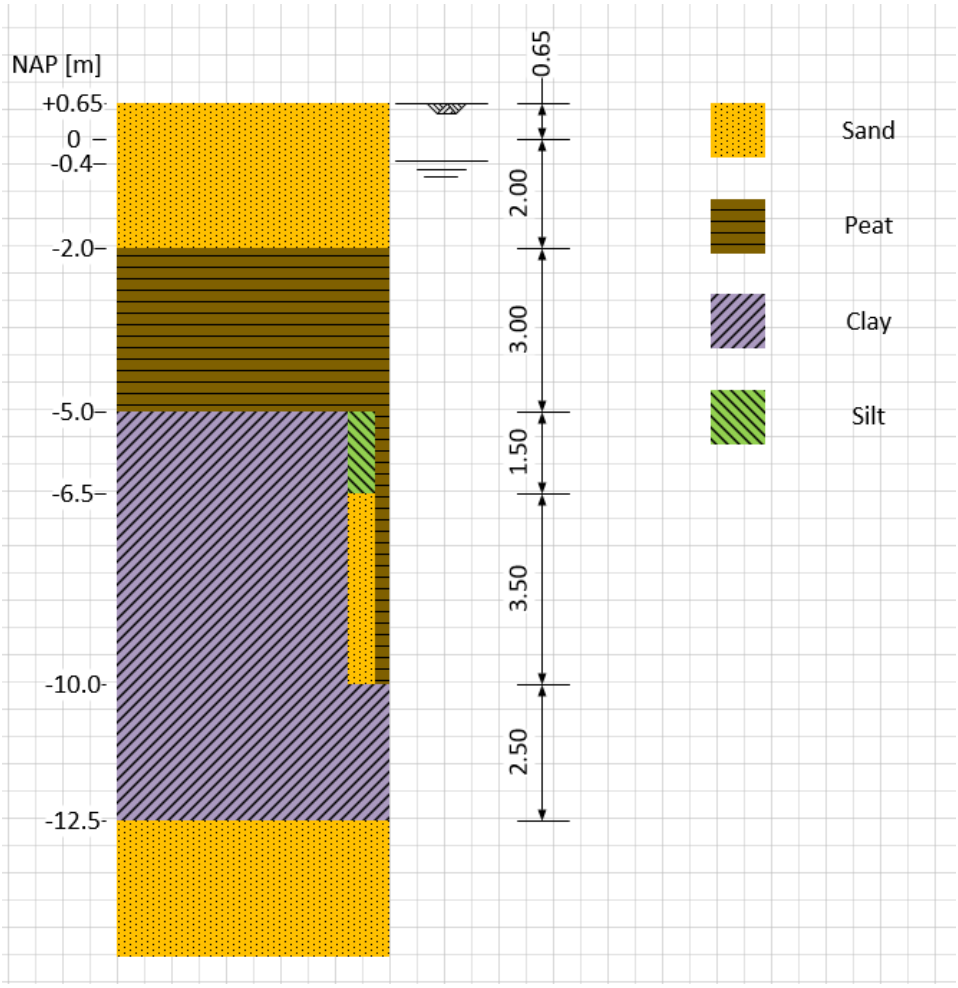

Figure C.1: Schematisation soil profile Herengracht

C.2. Unit weights and initial void ratio

For all layers, except the first sand layer, the lab classifications of the samples from the Herengracht itself were used. The samples were stored in Ackermann canisters for transport to the lab. The wet and dry unit weights, respectively γ_n and γ_{dry}, were determined in accordance with NEN-EN-ISO 17892-2. The saturated unit weight and void ratio have been determined using an estimation of the unit weight of the particles.

For the first sand layer, no data from the Herengracht was available. Instead, data was used from a drilling at the Entrepotdok. Only 1 sample had been taken from the first sand layer; the unit weights and void ratio was taken equal to this value.

A log-normal distribution was used to determine the mean value of the unit weights and void ratios. It has been decided to use a log-normal distribution instead of a Gaussian one, as the latter one would allow for negative values, which are impossible for these parameters. The distributions follow below:

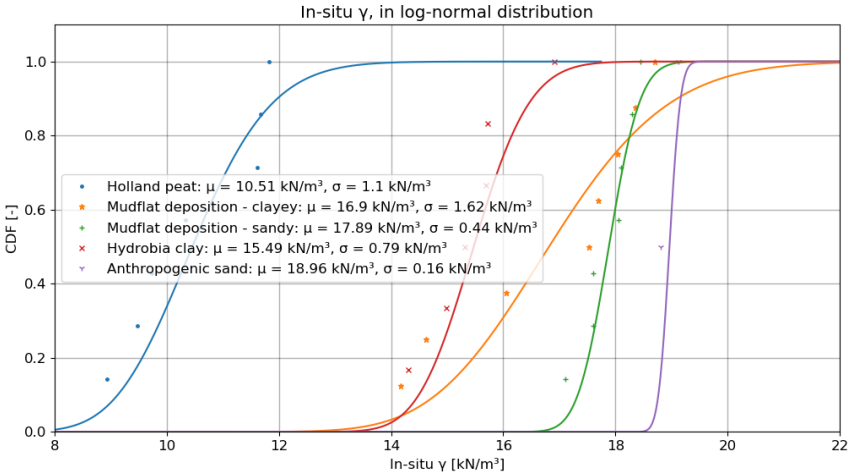

Figure C.2: Log-normal distribution natural specific weight, from Herengracht sample lab classification

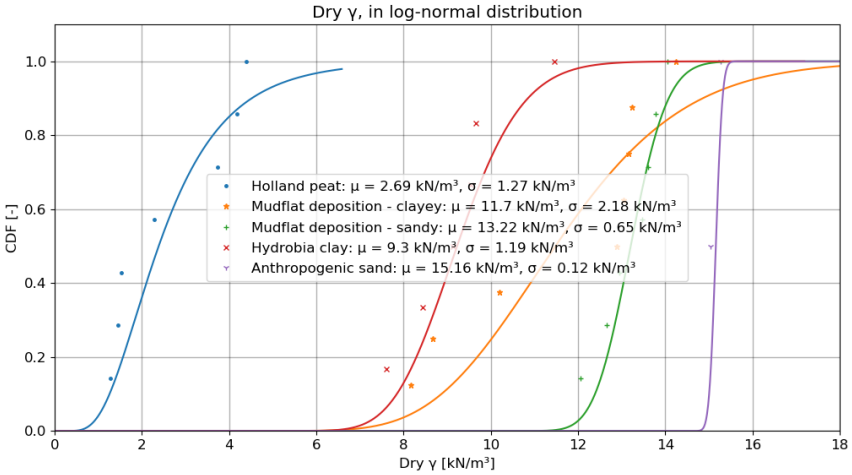

Figure C.3: Log-normal distribution dry specific weight, from Herengracht sample lab classification

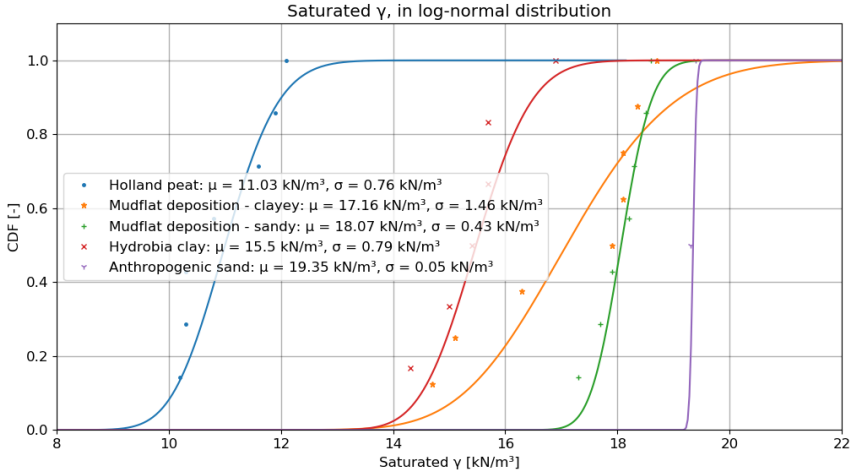

Figure C.4: Log-normal distribution saturated specific weight, from Herengracht sample lab classification

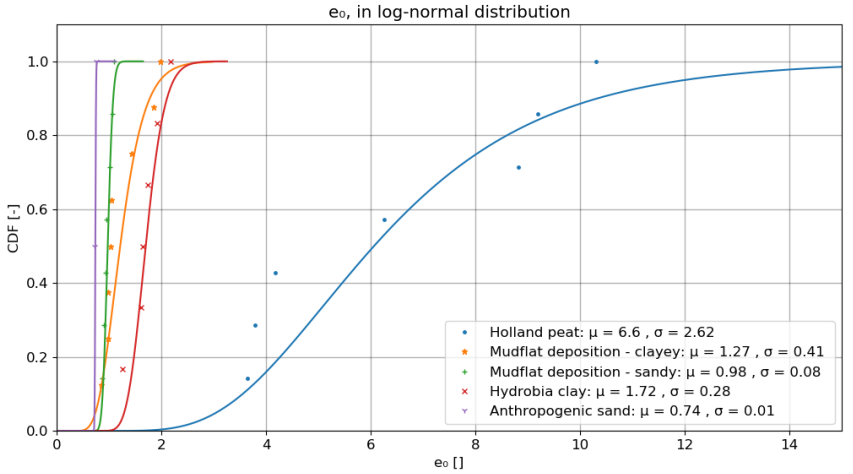

Figure C.5: log-normal distribution initial void ratio, from Herengracht sample lab classification

The obtained values have been presented in the following table:

Layer	**1**	**2**	**3**	**4**	**5**	**6**	
Parameter							**Unit**
γ_n	19.0	10.5	16.9	17.9	15.5	17.7	kN/m^3
γ_{dry}	15.2	2.69	11.7	13.2	9.30	14.7	kN/m^3
γ_{sat}	19.4	11.0	17.2	18.1	15.5	18.9	kN/m^3
e_0	0.740	6.60	1.27	0.980	1.72	0.774	–

Table C.2: Unit weights and void ratios per layer, with layers defined as:
1: Anthropogenic sand
2: Holland peat
3: Mudflat deposition - clayey
4: Mudflat deposition - sandy
5: Hydrobia clay
6: First sand layer

C.3. Shear strength and dilatency parameters

The effective strength parameters φ' and c' were obtained from different sources. Consolidated Isotropic Undrained triaxial tests had been performed on samples from the Herengracht, but only reliable data for the Holland peat and clayey mudflat deposition were obtained. For the Hydrobia clay, one triaxial test was available from the Entrepotdok drilling. The triaxial test data has been plotted in the s'-t space in order to determine the effective strength parameters.

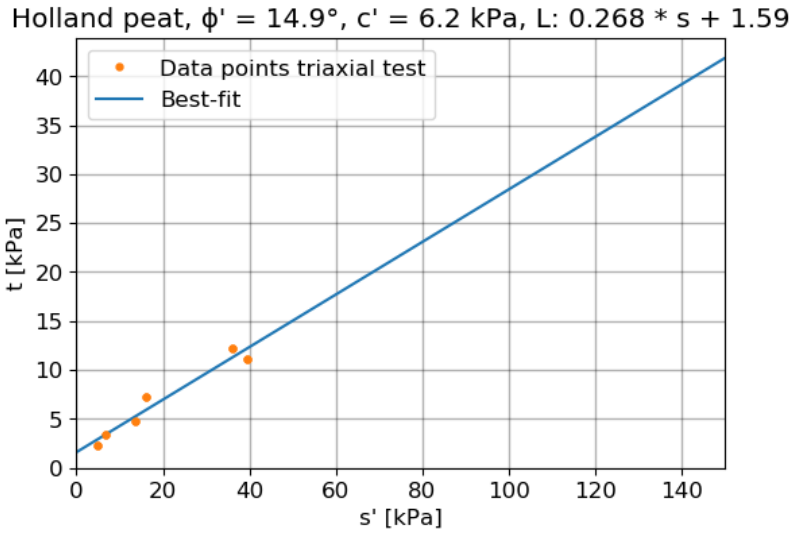

Figure C.6: Holland peat CIU triaxial tests data in s'-t space with corresponding effective strength parameters

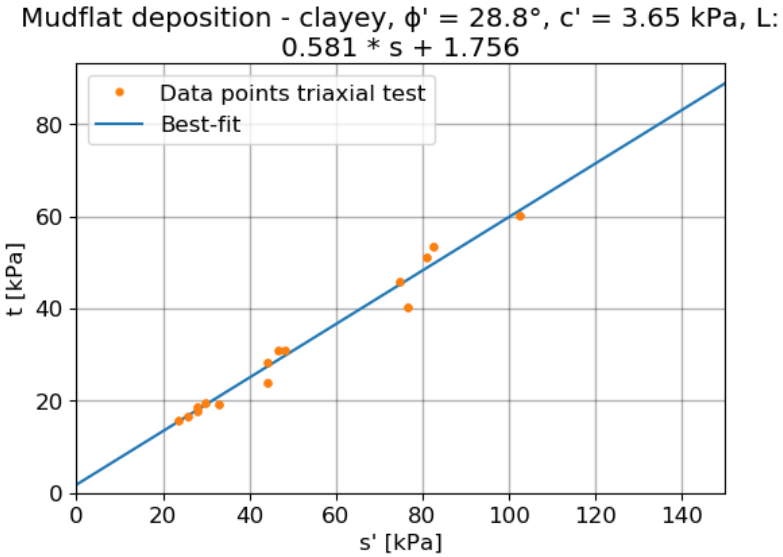

Figure C.7: Mudflat deposition - clayey CIU triaxial tests data in s'-t space with corresponding effective strength parameters

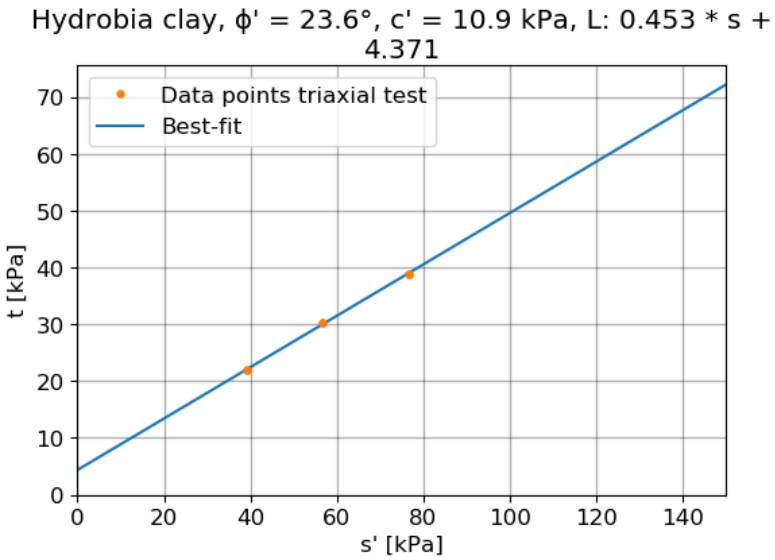

Figure C.8: Hydrobia clay CIU triaxial tests data in s'-t space with corresponding effective strength parameters

The results of the Hydrobia clay layer contain a relative high value for the cohesion. Internal documents suggest a more common value of 8 kPa, mentioning it is still on the high side. However, according to the experience numbers of the North-South metro line, a maximum of 15 kPa is possible Herbschleb (1999). Hence, the obtained value from the triaxial test will still be used.

For both sand layers and the sandy mudflat deposition, no triaxial data test that could be used was available. Instead, recommended numbers from different reports have been averaged to come to the required parameters. The following sources have been used:

- (S11) Parameters on the soil at the Jordaan (Visser, 1988)
- (S12) Soil parameter set for the design of bridge 112 at the Lauriergracht (Maagdelijn and Philippart, 1988)
- (NZ) Parameter set Holocene soil layers North-South metro line (Herbschleb, 1999)

Layer	**1**	**4**	**6**
Source		φ'[°]	
S11	30.0	20.0	N.A.
S12	35.0	28.0	35.0
NZ	N.A.	27.0	N.A.
Average	32.5	25.0	35.0
		$c'[kPa]$	
S11	0.00	4	0.00
S12	0.00	0	0.00
NZ	0.00	2.5	0.00
Average	0.00	2.17	0.00

Table C.3: Estimated effective strength parameters from sources as mentioned on Page 110, with layers defined as:
1: Anthropogenic sand
4: Mudflat deposition - sandy
6: First sand layer

No data from the Herengracht site was available to determine the dilatency angle. Hence, the following relation has been used (Plaxis, 2019b):

$$\psi \approx \varphi' - 30° <= 0 \tag{C.1}$$

A summary of the obtained strength and dilatency parameters is presented in Table C.4.

Layer	1	2	3	4	5	6	
Parameter							**Unit**
φ'	32.5	14.9	28.8	25.0	23.6	35.0	°
c'	0.00	6.20	3.65	2.17	10.9	0.00	kPa
ψ	2.50	0.00	0.00	0.00	0.00	5.00	°

Table C.4: HSsmall properties per layer, with layers defined as:
1: Anthropogenic sand
2: Holland peat
3: Mudflat deposition - clayey
4: Mudflat deposition - sandy
5: Hydrobia clay
6: First sand layer

C.4. Elasticity parameters

For the Poisson's values, the values have been taken from an internal data set for the North-South line, which have been obtained from literature and calibrated for the HSsmall model. The values can be found in Table C.6.

The results of the triaxial test data have been used to determine the E-moduli for the cohesive soils. The data provided the $E_{50,undr}$ and corresponding confining pressure σ'_3. The following equation has been used to calculate elastic modulus at the reference confining pressure p^{ref} = 100 kPa:

$$E_{50} = E_{50}^{ref} \left(\frac{c' cos(\varphi') - \sigma'_3 sin(\varphi')}{c' cos(\varphi') + p^{ref} sin(\varphi')} \right)^m \tag{C.2}$$

With:

- E_{50}: elastic modulus at 50% mobilisation for primary loading as calculated in triaxial test [kPa]
- E_{50}^{ref}: elastic modulus for primary loading at reference confining pressure [kPa]
- c': effective cohesion [kPa]
- φ': effective friction angle[°]
- σ'_3: effective confining pressure in triaxial test [kPa]
- p^{ref}: reference pressure = 100 kPa
- m: amount of stress dependency [-]

For the stress-dependency factor m, the following assumed values have been used:

Layer	1	2	3	4	5	6	
Parameter							**Unit**
m	0.5	0.9	0.8	0.7	0.8	0.5	–

Table C.5: Stress dependency stiffness, with layers defined as:
1: Anthropogenic sand
2: Holland peat
3: Mudflat deposition - clayey
4: Mudflat deposition - sandy
5: Hydrobia clay
6: First sand layer

The test data for the $E_{50,undr}$ and corresponding calculated $E^{ref}_{50,undr}$ have been plotted in the following figures:

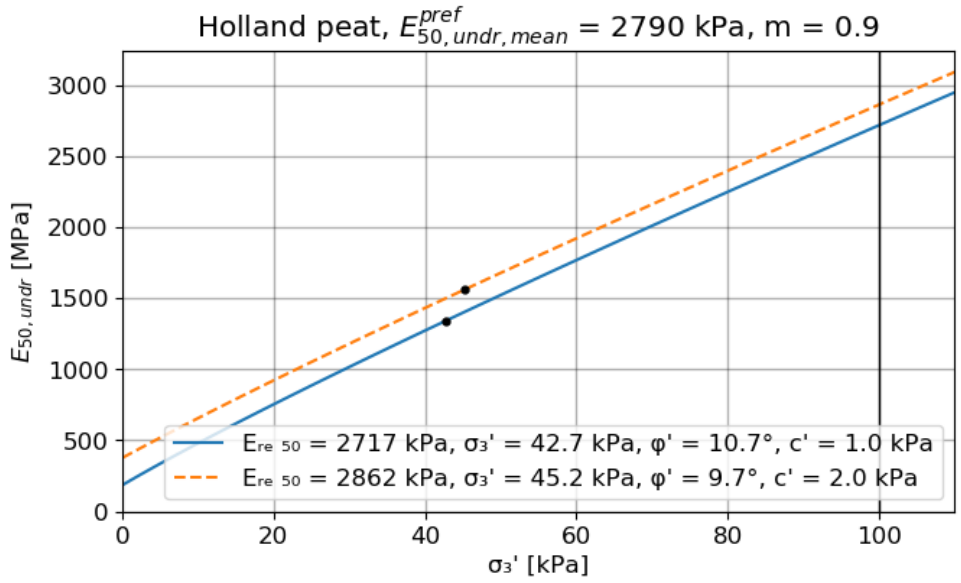

Figure C.9: Test data Holland peat for $E_{50,undr}$ and corresponding $E^{ref}_{50,undr}$

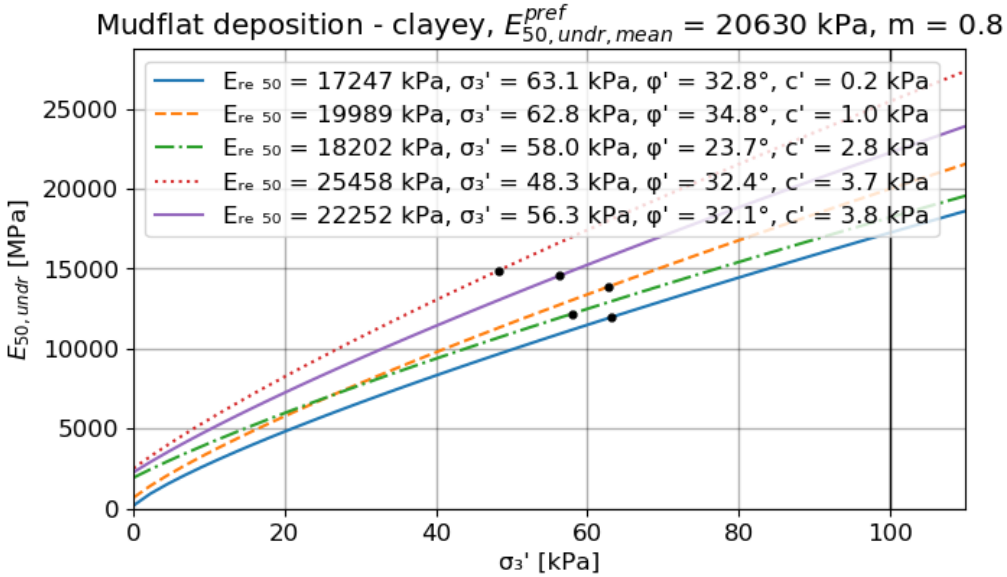

Figure C.10: Test data Mudflat deposition - clayey for $E_{50,undr}$ and corresponding $E^{ref}_{50,undr}$

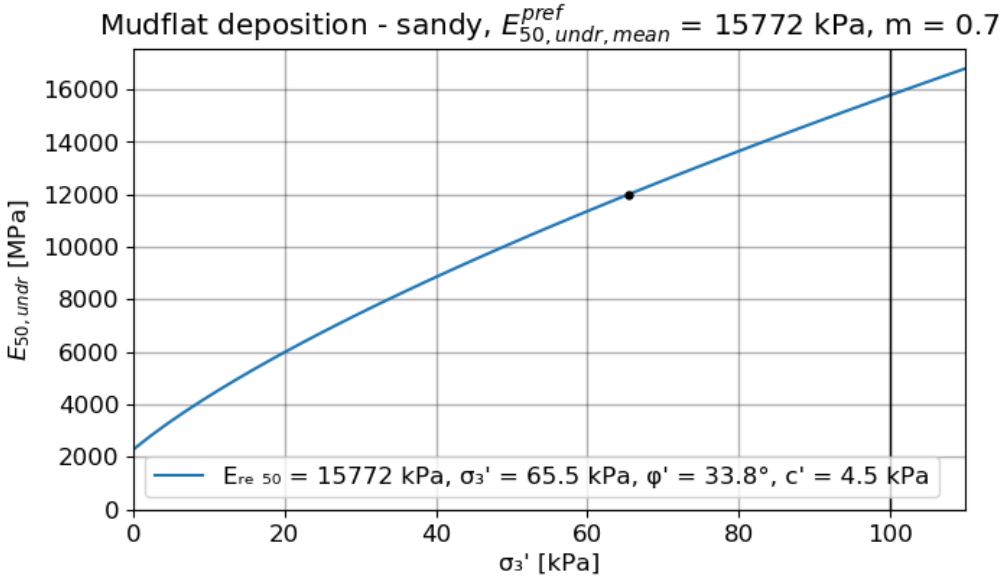

Figure C.11: Test data Mudflat deposition - sandy for $E_{50,undr}$ and corresponding $E^{ref}_{50,undr}$

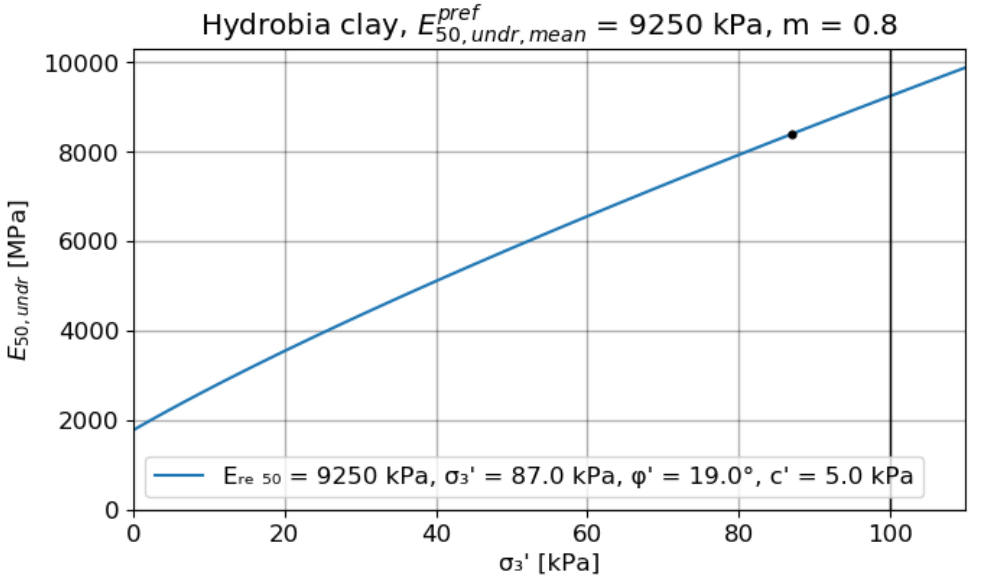

Figure C.12: Test data Hydrobia clay for $E_{50,undr}$ and corresponding $E^{ref}_{50,undr}$

This conversion was done for each test, after which the parameter value for $E^{ref}_{50,undr}$ was taken equal to the average of all tests, per layer. In order to calculate the drained moduli, the next relation was used:

$$E^{ref}_{50} \approx \frac{E^{ref}_{50,undr}}{1.25} \tag{C.3}$$

From this value, the drained oedometer and unloading-reloading moduli E_{oed}^{ref} and E_{ur}^{ref} were calculated as follows (Alpan, 1970):

$$E_{oed}^{ref} = \frac{(1-\nu)\,E_{50}^{ref}}{(1+\nu)\,(1-2\nu)} \qquad E_{ur}^{ref} \approx E_{50}^{ref} \tag{C.4}$$

For the sand layers, the values have been taken from the internal data set for the North-South line, as no other data was available. The obtained parameters have been presented in Table C.6.

Layer	**1**	**2**	**3**	**4**	**5**	**6**	
Parameter							**Unit**
ν_{ur}	0.15	0.15	0.15	0.20	0.15	0.20	–
m	0.5	0.9	0.8	0.7	0.8	0.5	–
E_{50}^{ref}	20.0	2.32	16.5	12.6	7.40	40.0	MPa
E_{oed}^{ref}	21.1	2.36	17.4	14.0	7.81	44.4	MPa
E_{ur}^{ref}	60.0	6.70	49.5	37.9	22.2	120.	MPa

Table C.6: HSsmall properties per layer, with reference pressure p_{ref} = 100 kPa, with layers defined as:
1: Anthropogenic sand
2: Holland peat
3: Mudflat deposition - clayey
4: Mudflat deposition - sandy
5: Hydrobia clay
6: First sand layer

C.5. Shear stiffness parameters

The shear parameters have been calculated using the article from M. A. op de Kelder (2015). The initial shear modulus G_0 have been calculated using elasticity theory (Wichtmann and Triantafyllidis, 2009):

$$G_0 = \frac{E_0}{2\,(1+\nu)} \tag{C.5}$$

With:

- G_0: initial shear modulus $[kPa]$
- E_0: elastic modulus at small strains, taken equal to elastic modulus for un- and reloading E_{ur} $[kPa]$
- ν: Poisson's ratio $[-]$

The threshold shear strain $\gamma_{0.7}$ has been calculated using the following estimation Hardin and Drnevich (1972):

$$\gamma_{0.7} \approx \frac{1}{9G_0}\left[2c'\left(1+cos\left(2\varphi'\right)\right)+\sigma_1'\left(1+k_0\right)sin\left(2\varphi'\right)\right] \tag{C.6}$$

The determined shear parameters can be found in Table C.7.

Layer	**1**	**2**	**3**	**4**	**5**	**6**	
Parameter							**Unit**
G_0	26.1	2.91	21.5	15.8	9.65	50.0	MPa
$\gamma_{0.7}$	5.65E-4	4.19E-3	7.20E-4	9.01E-4	1.77E-3	2.98E-4	–

Table C.7: Shear properties per layer, with layers defined as:
1: Anthropogenic sand
2: Holland peat
3: Mudflat deposition - clayey
4: Mudflat deposition - sandy
5: Hydrobia clay
6: First sand layer

D

Determination Timber Parameter Set

The main source of data used for the wood parameters consists of an inspection of a bridge at the Herengracht, including adjacent quay walls (Ruiter, 2015). In this inspection, 10 piles were investigated that were representative for the Herengracht model. This included visual inspections, taking samples and performing lab analysis. The samples have a diameter of ø = 10 mm and a minimum length of half the diameter of the construction element.

D.1. Wood species and age

From the 10 piles investigated, 6 were made from European Spruce *Picae abies*) and 4 from Scots Pine (*Pinus sylvestris*). Hence, the other piles were taken into consideration to determine the wood species. Out of the 65 samples, 45 consisted of European Spruce, 11 Scots Pine and 9 were undetermined. Therefore, it has been decided to assume the timber elements to be composed of European Spruce. Only data from European spruce samples will be used for further parameter determination.

The inspection reports the year of construction to be 1886, which gives the quay wall an age of 134 years. It is unclear how the year of construction was determined, but it is most likely this was done through archival research.

D.2. Modulus Of rupture and elastic bending modulus

No bending data was available for the timber elements. Instead, numbers for Young's modulus have been taken from Kránitz (2014). In this report, they compared test data performed on aged timber beams from residential buildings, of different wood species and age. The MOR and elastic bending modulus had been determined according to standard DIN-52-186 1978. For this report, data has been taken from tests that were performed on *Picae abies*) samples with a similar age to the Herengracht quay wall, which is 134 years. Kranitz reported the test data to be within range of what literature mentions for values. The following test data has been used:

Sample	**Age** $[yrs]$	E_B $[MPa]$
SA06	150	10 385
SA07	150	12 233
SA08	120	12 900
SA09	150	11 936
Average	142.5	11 864

Table D.1: Samples used for determining bending characteristics, obtained from Kránitz (2014)

Kránitz (2014) also reported Moduli Of Rupture. A mean average MOR of approximately 80 MPa had been found. However, it has been chosen to compare stress results to characteristic strength values as provided by the Eurocode. Given a mean elasticity modulus of 11.86 GPa, the corresponding strength class would be C27. Given this class, the following characteristic strength values apply:

Strength parameter	Strength $[MPa]$
$f_{m,k}$	27
$f_{t,0,k}$	16
$f_{c,0,k}$	22

Table D.2: Characteristic strengths C27

D.3. Density

The densities of each sample were reported per fraction. The average density per sample has been determined as follows:

$$\rho_{sample} = \sum_{i=1}^{n} \frac{\sum_{i=1}^{n} A_i \rho_i}{\sum_{i=1}^{n} A_i} \tag{D.1}$$

With:

- ρ_{sample}: average density of one sample $[kg/m^3]$
- i: fraction number within sample
- n: total number of fractions within sample
- r: size fraction, in radial direction $[m]$
- ρ_i: density of the fraction $[kg/m^3]$
- A_i: cross-sectional area of the fraction, longitudinally plane wood

The following data has been used to determine the density:

Sample		**1**	**2**	**3**	**4**	**5**	**6**	
Fraction								**Unit**
1	size	15	15	17	9	20	21	$[mm]$
	ρ	250	193	196	241	146	155	$[kg/m^3]$
2	size	36	12	21	19	29	8	$[mm]$
	ρ	324	246	289	228	188	187	$[kg/m^3]$
3	size	25	18	32	15	18	15	$[mm]$
	ρ	380	273	310	269	537	276	$[kg/m^3]$
4	size	N.A.	33	38	34	32	28	$[mm]$
	ρ	N.A.	441	369	317	330	316	$[kg/m^3]$
5	size	N.A.	32	N.A.	33	N.A.	29	$[mm]$
	ρ	N.A.	365	N.A.	341	N.A.	292	$[kg/m^3]$
ρ_{avg}		307	300	278	273	240	231	$[kg/m^3]$
Total ρ_{avg}		271						$[kg/m^3]$

Table D.3: Wood density per sample per fraction, fraction 1 represents the outside fraction, the highest fraction the inside Ruiter (2015)

As can be seen in Table D.3, an average density of 271 kg/m^3 has been calculated. However, Blaßand Sandhaas (2017) mentions the densities of spruce to be in the range of 400-700 kg/m^3. Furthermore, the samples from Kránitz (2014) measured densities of around 435 kg/m^3. It is likely the reported density is lower than normal due to deterioration. It is unclear how the densities have been determined.

E

Pile Resistance Parameters

The lateral, axial and toe resistance of the pile are part of the user input for the Embedded Beam Row in Plaxis. This chapter elaborates on the determination of these resistances.

E.1. Lateral resistance

For the ultimate lateral resistance of the pile, the relations developed by Brinch-Hansen (1961) has been used:

$$
\begin{aligned}
\sigma_p &= K_q \sigma'_v + K_c c \\
K_q &= \frac{K_q^0 + K_q^\infty \alpha_q \frac{D}{B}}{1 + \alpha_q \frac{D}{B}} \\
K_c &= \frac{K_c^0 + K_c^\infty \alpha_c \frac{D}{B}}{1 + \alpha_c \frac{D}{B}} \\
K_q^0 &= e^{\left(\frac{\pi}{2}+\varphi\right) tan(\varphi)}\ cos(\varphi)\ tan\left(\frac{\pi}{4}+\frac{\varphi}{2}\right) - e^{\left(-\frac{\pi}{2}+\varphi\right) tan(\varphi)}\ cos(\varphi)\ tan\left(\frac{\pi}{4}-\frac{\varphi}{2}\right) \\
K_c^0 &= \left(e^{\left(\frac{\pi}{2}+\varphi\right) tan(\varphi)}\ cos(\varphi)\ tan\left(\frac{\pi}{4}+\frac{\varphi}{2}\right) - 1\right) cot(\varphi) \\
K_q^\infty &= K_c^\infty\ K_0\ tan(\varphi) \\
K_c^\infty &= N_c\ d_c^\infty \\
d_c^\infty &= 1.58 + 4.09\ tan^4(\varphi) \\
N_c &= \left(e^{\pi tan(\varphi)}\ tan^2\left(\frac{\pi}{2}+\varphi\right) - 1\right) cot(\varphi) \\
K_0 &= OCR^{sin(\varphi)}\left(1 - sin(\varphi)\right) \\
\alpha_q &= \frac{K_q^0}{K_q^\infty - K_q^0} * \frac{K_0 sin(\varphi)}{sin\left(\frac{\pi}{4}+\frac{\varphi}{2}\right)} \\
\alpha_c &= \frac{K_c^0}{K_c^\infty - K_c^0} * 2sin\left(\frac{\pi}{4}+\frac{\varphi}{2}\right)
\end{aligned}
\tag{E.1}
$$

With:

- σ_p: ultimate passive earth pressure $[kPa]$
- σ'_v: vertical effective soil pressure $[kPa]$
- c: cohesion $[kPa]$
- D: depth $[m]$
- B: pile width $[m]$
- φ: friction angle $[°]$
- OCR: Over-Consolidation Ratio $[-]$

The vertical effective soil pressure has been calculated using self-weight of the soil and hydrostatic water pressure. The parameters used are as described as in Appendices B and C. Plaxis requires the lateral resistance as force per unit pile length. Hence, the ultimate passive earth pressure is to be multiplied width the width, from which the result is the input for the Embedded Beam Row.

E.2. Axial resistance

The axial resistance has been determined using method Koppejan:

$$p_{r;max;shaft;z} = \alpha_s q_{c;z;a} \tag{E.2}$$

With:

- $p_{r;shaft;max;z}$: maximum pile shaft friction at depth z $[kPa]$
- α_s: pile installation factor. For the cohesive layers, it is unclear whether these would provide positive or negative shaft friction on the piles. Hence, the friction contribution of the cohesive layers has been neglected. For wooden tapered piles in sand, $\alpha_s = 0.0012$ $[-]$
- $q_{c;z;a}$: cone resistance. Sounding peaks are limited to 15 MPa if occurring over more than 1 m, else to 12 MPa $[kPa]$

The sounding used has been presented in Figure E.1.

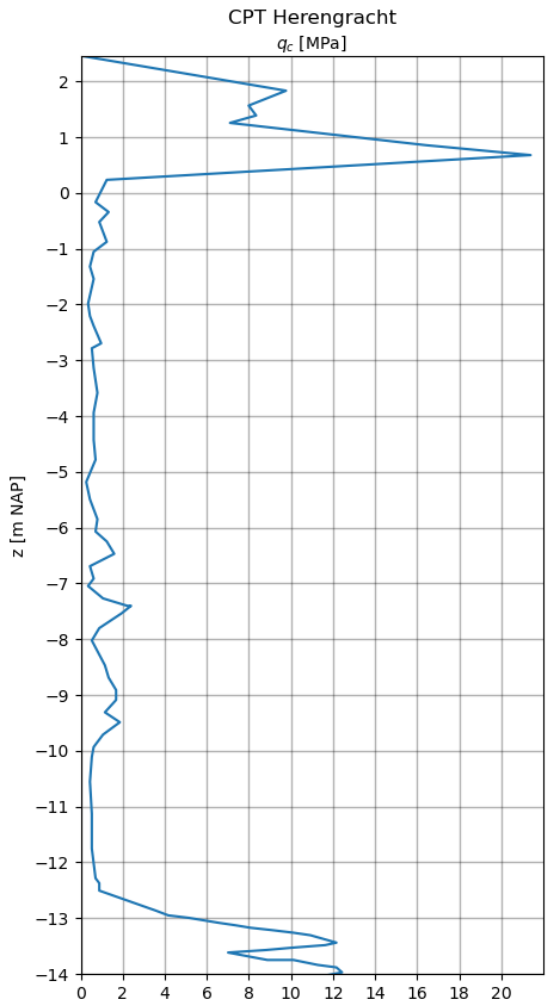

Figure E.1: Cone Penetration Test Herengracht

E.3. Tip resistance

The tip resistance has been determined using method Koppejan:

$$p_{r;max;tip} = \frac{1}{2}\alpha_p \beta s \left(\frac{q_{c;I;avg} + q_{c;II;avg}}{2} + q_{c;III;avg} \right) \tag{E.3}$$

With:

- $q_{c;I;avg}$, $q_{c;II;avg}$, $q_{c;III;avg}$: average cone resistance as described by NEN 9997-1 [kPa]
- α_p: pile class factor = 1 for driven piles [-]
- β: foot shape factor = 1 for this case [-]
- s: foot cross-section factor = 1 for this case [-]

Based on the CPT in Figure E.1, the following tip resistance has been determined:

$$\begin{aligned} p_{r;max;tip} &= \frac{1}{2}\alpha_p \beta s \left(\frac{q_{c;I;avg} + q_{c;II;avg}}{2} + q_{c;III;avg} \right) \\ &= \frac{1}{2} * 1 * 1 * 1 \left(\frac{7000 + 7000}{2} + 2000 \right) \\ &= 4500\ kPa \\ F_{tip} &= \frac{\pi}{4} D^2 p_{r;max;tip} \\ &= \frac{\pi}{4} (0.2)^2 * 4500 \\ &= 141.4\ kN \end{aligned} \tag{E.4}$$

F Input Plaxis 2D Herengracht Model

F.1. Geometry

The quay wall has been modelled as depicted in Figures F.1 and F.2. For the mesh settings, the pre-defined "Medium" mesh setting has been used.

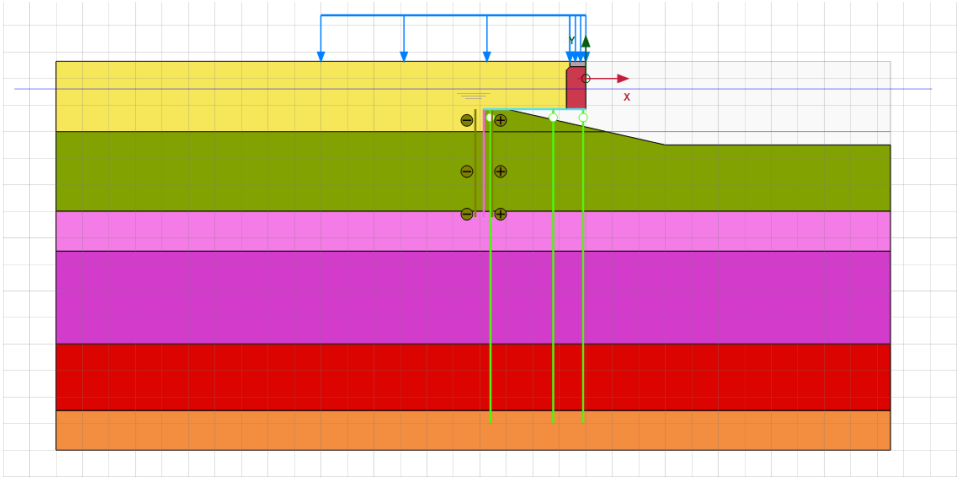

Figure F.1: Geometry Plaxis model Herengracht case

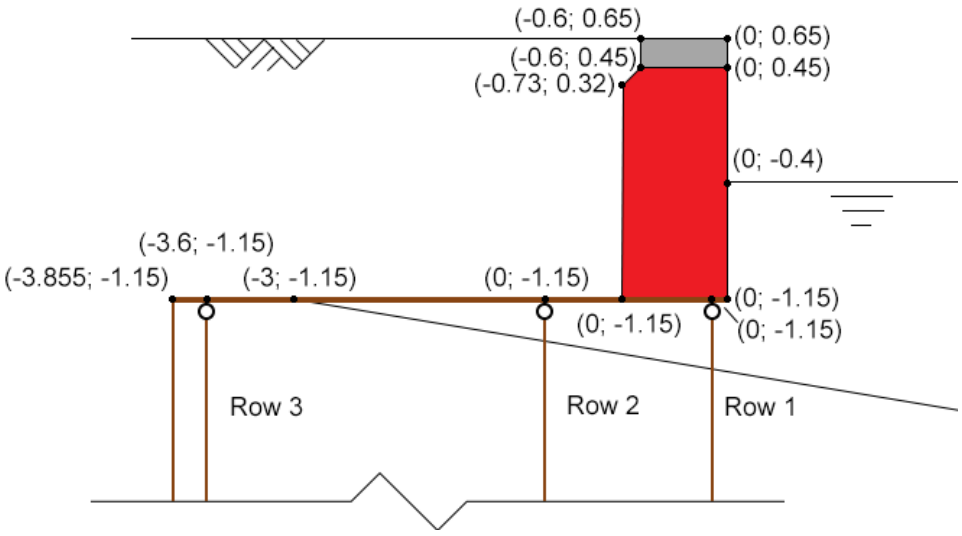

Figure F.2: Geometry Plaxis model Herengracht case, schematised

It has been decided to model both the floor as a plate element, with properties averaged per meter. For the Embedded Beam Rows, it has been decided to use use Interface Stiffness Factors equal to 10 times the Default value. Section 4.3, Page 33 shows that a better fit can be found with the D-Sheet calculations, even when it was a slight improvement. Furthermore, the results from Chapter 3 have shown that the default ISF values are too low.

F.2. Phases

Table F.1 shows the phases used, their order and a description per phase. Figures F.3 to F.5 show the model for different phases. There was insufficient information to model the construction of the quay wall. Hence, the construction has been modelled using only one phase.

Phase number	Start from phase	Description
0	N.A.	Initial phase, soil profile homogeneous in horizontal plane, stress generation via K0 procedure
1	0	Moment just after finishing construction quay wall, t=0
2	1	Applying load on the quay wall directly after finishing construction, using parameters from t=0
3	1	Applying load on the quay wall directly after finishing construction, using parameters from t=∞
4+	2	Calculating deformation at different points in time, using parameters 0<t=∞

Table F.1: Plaxis 2D phases Herengracht model

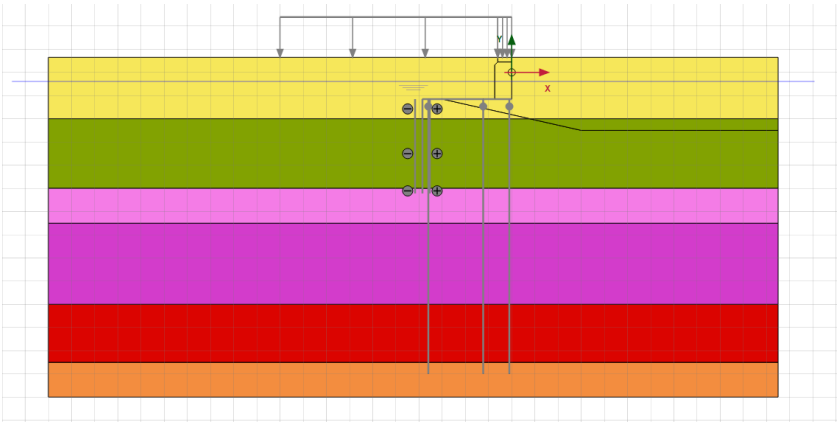

Figure F.3: Plaxis model Herengracht case, initial phase

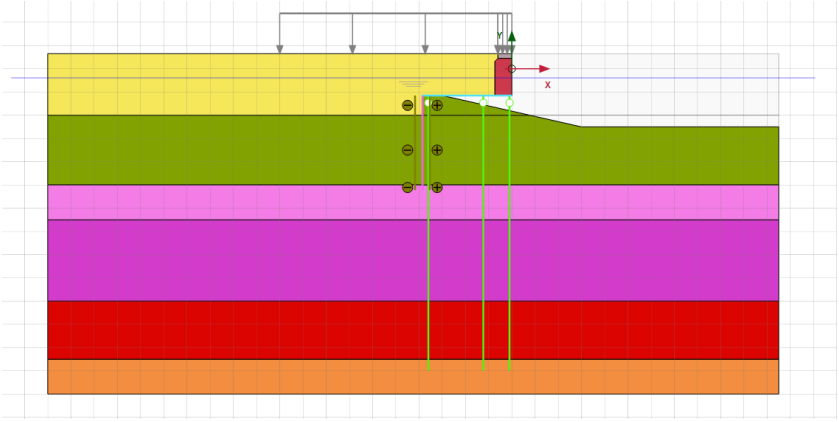

Figure F.4: Plaxis model Herengracht case, phase 1

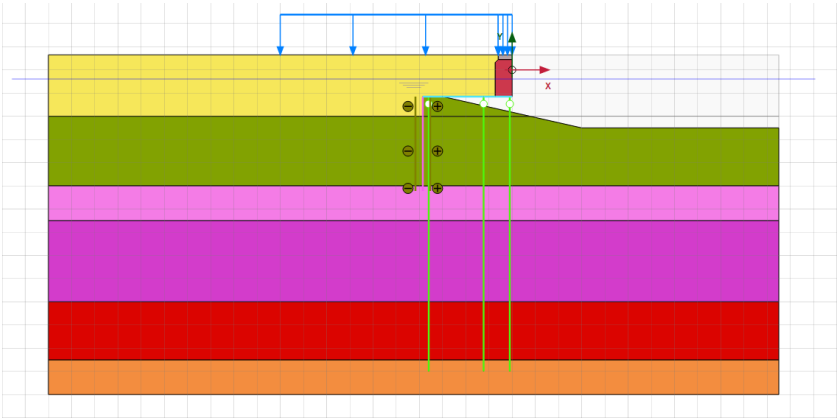

Figure F.5: Plaxis model Herengracht case, phases 2+

F.3. Deformation and numerical control parameters

General	
Calculation type	K0 procedure
Loading type	Staged construction
$\sum M_{weight}$	1.00
Pore pressure calculation type	Phreatic
Thermal calculation type	Ignore temperature
Deformation control parameters	
Updated water pressure	False
Ignore suction	True

Table F.2: Deformation and numerical control parameters Plaxis 2D model Herengracht case, initial phase

Parameter	**Phase 1**	**Phase 2**	**Phase 3**	**Phase 4+**
General				
Calculation type	Plastic			
Loading type	Staged construction			
$\sum M_{stage}$	1.00	1.00	1.00	1.00
$\sum M_{weight}$	1.00	1.00	1.00	1.00
Pore pressure calculation type	Use pressures from previous phase	" "	" "	" "
Thermal calculation type	Ignore temperature	" "	" "	" "
Time interval	0.00 day	" "	" "	" "
Deformation control parameters				
Ignore undr. behaviour	False	" "	" "	" "
Reset displacements to zero	True	False	True	False
Reset small strains	True	False	True	False
Reset state variables	False	" "	" "	" "
Reset time	False	" "	" "	" "
Updated mesh	True	" "	" "	" "
Updated water pressure	False	" "	" "	" "
Ignore suction	True	" "	" "	" "
Cavitation cut-off	False	" "	" "	" "
Numerical control parameters				
Max cores to use	256	" "	" "	" "
Max numbers of steps stored	1	" "	" "	" "
Use default iter parameters	False	" "	" "	" "
Max steps	1000	1000	1000	1000
Tolerated error	0.0100	0.0100	0.0100	0.0100
Max unloading steps	5	100	5	100
Max load fraction per step	0.500	0.100	0.100	0.500
Over-relaxation factor	1.20	1.20	1.20	1.20
Max number of iterations	60	60	60	60
Desired min number of iterations	6	6	6	6
Desired max number of iterations	15	15	15	15
Arc-length control type	On	" "	" "	" "
Use line search	False	" "	" "	" "
Use gradual error reduction	False	" "	" "	" "

Table F.3: Deformation and numerical control parameters Plaxis 2D model Herengracht case, phases 1 and up

G

Results Sensitivity Analysis Creep Influence Herengracht Case

This appendix presents an overview of the numerical results of the sensitivity analysis. For the sensitivity analysis, two quantities have been compared; the relative change in horizontal displacement as well as in maximum compressive stress in pile row 1, the front row, due to the creep. This has been compared to the relative change in the reference case. This can be written in formula form as follows:

$$
\begin{aligned}
Relative\ Influence\ Displacement &= \frac{\left(\frac{u_x(\varphi=1.6)-u_x(\varphi=0.0)}{u_x(\varphi=0.0)}\right)}{\left(\frac{u_{x,ref}(\varphi=1.6)-u_{x,ref}(\varphi=0.0)}{u_{x,ref}(\varphi=0.0)}\right)} \\
Relative\ Influence\ Stress &= \frac{\left(\frac{\sigma_{c,max,row1}(\varphi=1.6)-\sigma_{c,max,row1}(\varphi=0.0)}{\sigma_{c,max,row1}(\varphi=0.0)}\right)}{\left(\frac{\sigma_{c,max,row1,ref}(\varphi=1.6)-\sigma_{c,max,row1,ref}(\varphi=0.0)}{\sigma_{c,max,row1,ref}(\varphi=0.0)}\right)}
\end{aligned}
\tag{G.1}
$$

For the discussion of the results, see Chapter 6, Page 51.

G.1. Results sensitivity analysis - displacement

Variation	u_0 [mm]	$u_{\varphi=1.6}$ [mm]	Creep displacement as factor of u_0 [-]	Relative to reference [-]
Add Pile	120.8	351.1	+1.908	-14.2%
E_B +20%	128.2	347.6	+1.711	-23.0%
E_B -20%	136.5	566.0	+3.145	+41.5%
Fixed pile-floor connection	74.85	254.8	+2.405	+8.19%
ISF +20%	132.9	422.2	+2.177	-2.04%
ISF -20%	132.5	419.5	+2.165	-2.57%
ISF x0.2	134.0	451.4	+2.368	+6.53%
ISF x5	131.4	426.7	+2.248	+1.13%
Layer 2 c' +20%	95.62	176.2	+0.843	-62.1%
Layer 2 c' -20%	N.A. †	N.A.	N.A.	N.A.
Layer 2 G_0 +20%*	118.2	353.3	+1.990	+10.5%
Layer 2 G_0 -20%*	149.6	499.3	+2.338	+5.19%
Layer 2 $\gamma_{0.7}$ +20%	131.3	413.5	+2.148	-3.34%
Layer 2 $\gamma_{0.7}$ -20%	131.6	426.5	+2.241	+0.82%
Layer 2 tan(φ') +20%*	128.3	325.6	+1.537	+30.8%
Layer 2 tan(φ') -20%	N.A. †	N.A.	N.A.	N.A.
Layer 3 c' +20%	129.7	407.1	+2.140	-3.73%
Layer 3 c' -20%	135.8	422.4	+2.111	-5.03%
Layer 3 G_0 +20%	130.3	414.7	+2.183	-1.79%
Layer 3 G_0 -20%	134.1	409.6	+2.055	-7.53%
Layer 3 $\gamma_{0.7}$ +20%	131.8	423.8	+2.216	-0.27%
Layer 3 $\gamma_{0.7}$ -20%	131.7	424.6	+2.223	+0.03%
Layer 3 tan(φ') +20%	126.7	413.1	+2.260	+1.68%
Layer 3 tan(φ') -20%	138.5	405.7	+1.930	-13.1%
Layer 4 c' +20%	130.8	430.5	+2.292	+3.14%
Layer 4 c' -20%	132.6	411.7	+2.106	-5.26%
Layer 4 G_0 +20%	131.0	415.0	+2.168	-2.45%
Layer 4 G_0 -20%*	131.5	402.6	+2.061	-7.26%
Layer 4 $\gamma_{0.7}$ +20%	131.9	416.0	+2.154	-3.08%
Layer 4 $\gamma_{0.7}$ -20%	132.0	439.4	+2.329	+4.80%
Layer 4 tan(φ') +20%*	131.3	417.6	+2.181	-1.87%
Layer 4 tan(φ') -20%	131.5	397.2	+2.020	-9.12%
Layer 5 c' +20%	132.7	409.5	+2.086	-6.13%
Layer 5 c' -20%	131.1	401.8	+2.064	-7.13%
Layer 5 G_0 +20%	131.4	415.6	+2.162	-2.72%
Layer 5 G_0 -20%	131.6	421.3	+2.202	-0.92%
Layer 5 $\gamma_{0.7}$ +20%	132.1	406.1	+2.074	-6.69%
Layer 5 $\gamma_{0.7}$ -20%	131.6	410.6	+2.121	-4.57%
Layer 5 tan(φ') +20%*	131.7	405.5	+2.080	-6.44%
Layer 5 tan(φ') -20%*	130.8	414.7	+2.170	-2.35%
Layer 6 G_0 +20%	132.0	414.8	+2.142	-3.63%
Layer 6 G_0 -20%	132.6	411.9	+2.106	-5.23%
Layer 6 $\gamma_{0.7}$ +20%	133.2	392.0	+1.942	-12.6%
Layer 6 $\gamma_{0.7}$ -20%	131.8	425.1	+2.225	+0.10%
Layer 6 tan(φ') +20%	132.3	408.9	+2.090	-5.94%
Layer 6 tan(φ') -20%*	132.8	404.4	+2.046	-7.95%
Load +20%*	154.2	816.7	+4.295	+93.3%
Load -20%*	111.0	279.9	+1.523	-31.5%
Load behind	115.5	227.4	+0.969	-56.4%
Load on top	75.78	134.7	+0.778	-65.0%
$\Delta\varphi = 0.2$	131.2	371.5	+1.831	-17.6%
$\Delta\varphi = 0.05$*	131.2	414.8	+2.161	-2.77%
Retaining screen +20%	130.7	336.9	+1.578	-29.0%
Retaining screen -20%	131.4	461.7	+2.514	+13.1%
Unloading Reloading	131.2	437.2	+2.333	+4.99%

Table G.1: Results sensitivity analysis creep influence - displacement
*: different numerical parameters have been used in one or more phases to reach final creep factor
†: the quay wall had collapsed before reaching the final creep factor

G.2. Results sensitivity analysis - maximum compressive stress pile row 1

Variation	σ_0 [MPa]	$\sigma_{\varphi=1.6}$ [MPa]	Stress decrease as factor of σ_0 [-]	Relative to reference [-]
Add Pile	-12.60	-4.502	-0.643	+8.95%
E_B +20%	-13.67	-4.335	-0.683	+15.7%
E_B -20%	-14.69	-11.93	-0.188	-68.2%
Fixed pile-floor connection	-11.49	-3.397	-0.704	+19.4%
ISF +20%	-14.23	-6.224	-0.562	-4.66%
ISF -20%	-14.14	-5.527	-0.609	+3.23%
ISF x0.2	-13.93	-7.061	-0.493	-16.4%
ISF x5	-14.18	-6.110	-0.569	-3.51%
Layer2 c' +20%	-10.34	-2.912	-0.718	+21.8%
Layer2 c' -20%	N.A. †	N.A.	N.A.	N.A.
Layer2 G_0 +20%*	-13.06	-4.938	-0.622	+5.40%
Layer2 G_0 -20%*	-15.49	-6.456	-0.583	-1.12%
Layer2 $\gamma_{0.7}$ +20%	-14.04	-5.949	-0.576	-2.33%
Layer2 $\gamma_{0.7}$ -20%	-14.05	-6.151	-0.562	-4.70%
Layer2 $\tan(\varphi')$ +20%*	-14.39	-3.309	-0.770	+30.5%
Layer2 $\tan(\varphi')$ -20%	N.A. †	N.A.	N.A.	N.A.
Layer3 c' +20%*	-14.19	-5.667	-0.601	+1.82%
Layer3 c' -20%	-14.09	-6.039	-0.572	-3.12%
Layer3 G_0 +20%	-14.15	-5.599	-0.604	+2.43%
Layer3 G_0 -20%	-14.05	-5.608	-0.601	+1.85%
Layer3 $\gamma_{0.7}$ +20%	-14.09	-5.883	-0.582	-1.26%
Layer3 $\gamma_{0.7}$ -20%	-14.08	-5.825	-0.586	-0.60%
Layer3 $\tan(\varphi')$ +20%	-14.06	-5.928	-0.578	+1.98%
Layer3 $\tan(\varphi')$ -20%	-14.02	-5.583	-0.602	+2.01%
Layer4 c' +20%	-14.00	-6.435	-0.540	-8.40%
Layer4 c' -20%	-14.16	-5.647	-0.601	+1.90%
Layer4 G_0 +20%	-14.06	-6.144	-0.563	-4.56%
Layer4 G_0 -20%*	-13.96	-5.367	-0.616	+4.34%
Layer4 $\gamma_{0.7}$ +20%	-14.10	-5.778	-0.590	+0.05%
Layer4 $\gamma_{0.7}$ -20%	-14.11	-6.372	-0.548	-7.04%
Layer4 $\tan(\varphi')$ +20%*	-14.11	-5.904	-0.582	-1.40%
Layer4 $\tan(\varphi')$ -20%	-13.93	-5.348	-0.616	+4.45%
Layer5 c' +20%*	-14.20	-5.549	-0.609	+3.27%
Layer5 c' -20%*	-14.02	-5.529	-0.606	+2.68%
Layer5 G_0 +20%	-13.99	-5.842	-0.583	-1.26%
Layer5 G_0 -20%	-14.08	-5.929	-0.579	-1.85%
Layer5 $\gamma_{0.7}$ +20%	-14.13	-5.741	-0.594	+0.64%
Layer5 $\gamma_{0.7}$ -20%	-14.06	-5.964	-0.576	-2.37%
Layer5 $\tan(\varphi')$ +20%	-14.11	-5.378	-0.619	+4.92%
Layer5 $\tan(\varphi')$ -20%	-14.00	-5.548	-0.604	+2.37%
Layer6 G_0 +20%	-14.09	-5.704	-0.595	+0.90%
Layer6 G_0 -20%	-14.24	-5.625	-0.605	+2.54%
Layer6 $\gamma_{0.7}$ +20%	-14.22	-5.238	-0.632	+7.09%
Layer6 $\gamma_{0.7}$ -20%	-14.06	-6.094	-0.567	-3.96%
Layer6 $\tan(\varphi')$ +20%	-14.13	-5.358	-0.621	+5.24%
Layer6 $\tan(\varphi')$ -20%*	-14.20	-5.365	-0.622	+5.46%
Load +20%*	-16.34	-15.44	-0.055	-90.7%
Load -20%*	-11.91	-3.652	-0.693	+17.6%
Load Behind	-11.51	-2.505	-0.782	+32.6%
Load on Top	-8.699	-2.849	-0.672	+14.0%
$\Delta\varphi = 0.2$	-14.02	-5.837	-0.584	-1.07%
$\Delta\varphi = 0.05$*	-14.03	-5.612	-0.600	+1.70%
Retaining Screen +20%	-13.90	-4.902	-0.647	+9.74%
Retaining Screen -20%	-14.03	-6.983	-0.502	-14.9%
Unloading Reloading	-14.04	-5.946	-0.577	-2.27%

Table G.2: Results sensitivity analysis creep influence - maximum compressive stress pile row 1
*: different numerical parameters have been used in one or more phases to reach final creep factor
†: the quay wall had collapsed before reaching the final creep factor